Available online at www.sciencedirect.com
ScienceDirect
Surface Science Reports 62 (2007) 219–270
surface science reports
www.elsevier.com/locate/surfrep

Oxygen vacancies in transition metal and rare earth oxides: Current state of understanding and remaining challenges

M. Verónica Ganduglia-Pirovano*, Alexander Hofmann, Joachim Sauer

Humboldt-Universität zu Berlin, Institut für Chemie, Unter den Linden 6, D-10099 Berlin, Germany

Accepted 26 March 2007

Abstract

Defects at transition metal (TM) and rare earth (RE) oxide surfaces, neutral oxygen vacancies in particular, play a major role in a variety of technological applications. This is the motivation of numerous studies of partially reduced oxide surfaces. We review, discuss, and compare theoretical data for structural and electronic properties and energetic quantities related to the formation of oxygen defects at TM and RE oxide surfaces using TiO_2, ZrO_2, V_2O_5, and CeO_2 as examples. Bulk defects, as far as relevant for comparison with the properties of reduced surfaces, are briefly reviewed. Special attention is given to the fate of the electrons left in the system upon vacancy formation and the ability of state-of-the-art quantum-mechanical methods to provide reliable energies and an accurate description of the electronic structure of the partially reduced oxide systems.

Contents

* Corresponding author.
E-mail address: vgp@chemie.hu-berlin.de (M.V. Ganduglia-Pirovano).

0167-5729/$ - see front matter © 2007 Elsevier B.V. All rights reserved.
doi:10.1016/j.surfrep.2007.03.002

1. Introduction

Transition metal (TM) oxides constitute an important class of inorganic solids exhibiting a very wide variety of structures and electronic and magnetic properties that are due to the nature of the outer d states [1,2]. They are of great importance for a number of a technological applications such as heterogeneous catalysis, corrosion-protective coating of metals and microelectronic devices. Point defects in TM oxides such as vacancies and interstitials account for the transport properties of ionic solids. Furthermore, bulk defects play a significant role in determining surface properties where, for example, annealing to high temperatures is necessary. In addition, an important issue in TM oxide-based heterogeneous catalysis is the role of surface defects in determining the activity and selectivity of the catalyst. The existence of reduced surface centers — and hence the presence of neutral oxygen vacancies — is sometimes necessary for any activity. Ultimately, the potential of TM oxides in applications is related to the ability of the metal atoms to assume multiple oxidation states — for instance, vanadium can have the oxidation states II, III, IV, and V. This characteristic is not exclusive to transition (d) metal oxides and a representative example is given by ceria-based materials [3]. Many of the key properties of ceria, a rare earth (RE) oxide, arise from the fact that cerium has two stable oxidation states, namely, III and IV, in which f electron states are partially occupied or empty, respectively.

Oxygen vacancies at (TM and RE) oxide surfaces (or in the bulk) alter the geometric and electronic structure as well as chemical properties of the host system. In turn, the host system will largely determine the properties of the vacancies. The expectation that a fundamental understanding (i.e., microscopic) of these defects will help to elucidate the effect that they have on the system's functionality has been the driving force for pursuing experimental and theoretical research on reduced materials. For years oxygen vacancies have been detected and investigated using a variety of spectroscopic techniques, however, much has been learned recently about the structure of defective surfaces using scanning probe techniques. In spite of that, there are still difficulties in the experimental determination of the vacancy-induced lattice relaxations, and information about the vacancy formation energy (hence defect stability) is not always experimentally obtainable. Therefore, a great number of theoretical studies on oxygen removal from TM and RE oxides have appeared in the literature. In particular, *isolated* oxygen vacancies at differently oriented surfaces and in the bulk have received much attention. Strong interactions can occur between defects, causing them to cluster or order. Yet, isolated defects (or a low concentration of them) have been the natural starting point for the theoretical studies.

In this article, we consider the formation of oxygen vacancies at TM and RE oxide surfaces using TiO_2, ZrO_2, V_2O_5, and CeO_2 as examples. The partially reduced bulk oxides are also considered. The interest on these particular oxide surfaces is their importance for heterogeneous catalysis and other industrial applications. Their specific applications that are the deeper motivation for most of the performed work will be briefly mentioned in each of the sections that cover basic properties of the oxides. The focus is on theoretical studies and the more recent literature (after 1990). Inclusion of experimental studies would render a review unmanageably large given the vast number of experimental studies published since 1990 on oxygen defects for the systems considered. Nevertheless, the key experimental findings on the properties of the reduced systems are mentioned. One question of fundamental interest is: What is the electronic structure of the reduced oxides systems? In other words, when neutral oxygen atoms are removed, which states do the electrons left in the system populate? Another question, which is perhaps more practical, is: What is the energy required to form the oxygen defects? Answering these questions has provided a very strong motive to investigate the nature of neutral oxygen defects in the specific chosen systems at the atomistic level using density functional theory (DFT); see, e.g., Refs. [4–29] (TiO_2), Refs. [29–35] (ZrO_2), Refs. [36–42] (V_2O_5), and Refs. [43–

54] (CeO_2). Different exchange–correlation functionals have been applied, including the local density approximation (LDA) and generalized gradient approximation (GGA) for exchange and correlation [55–57], as well as hybrid functionals such as Becke–Lee–Yang–Parr (B3LYP), which contain a portion of exact exchange (20%) [58,59]. The Hartree–Fock (HF) and DFT+U approaches [60–63] have also been used. Defects have been modelled using either (embedded) cluster or the supercell approach, i.e., applying periodic boundary conditions.

While several theoretical articles and reviews that compare defective wide-gap oxides such as SiO_2, MgO, SnO_2, α-Al_2O_3, and HfO_2 (i.e., *non*-TM oxides in particular) were written in recent years [64–71], a comprehensive review of theoretical insights into oxygen vacancy properties in TM and RE oxides in general and in those considered in this report in particular, is lacking. In this report, an attempt is made to critically review the ability of different computational methods to provide reliable (geometrical and electronic) structures and energies for oxygen defects for selected examples of TM and RE oxides.

The four oxides, TiO_2, ZrO_2, V_2O_5, and CeO_2 are discussed in Sections 3, 4, 5 and 6, respectively. Each section starts with the basic structural and electronic properties of the bulk and selected low-index surfaces. Then the important experimental findings on the reduced systems are summarized. In the following subsections the theoretical insights into the structural and electronic properties and energetic quantities related to the formation of surface oxygen defects and in the bulk are reviewed and discussed. The article ends with a comparison of the systems considered and an outlook of the remaining challenges for first-principles studies in the field of oxygen defects in oxide materials.

2. Models and methods

In the so-called periodic approach to study solids, bulk and surfaces, the Schrödinger equation is (approximately) solved for the atoms of a unit cell containing a given number of atoms, subject to periodic boundary conditions in three dimensions. Surfaces are modelled in a supercell approach. Here one considers the periodic repetition of a two-dimensional periodic *slab* of the crystal together with a sufficiently thick vacuum layer, in the direction parallel to the surface normal. Hence, in the periodic approach one models two surfaces, one at each side of the slab. The thickness of the slab and vacuum layer are chosen so that the mutual interaction between the two surfaces of a slab and between those of periodic images, respectively, vanish. The presence of a point defect in the surface unit cell (typically on one side of the slab) results in its periodic repetition and a high concentration of surface defects. Increasing the size of the unit cell in the surface plane reduces the defect concentration, but increases the computational cost. Similar considerations apply to defects in the bulk unit cell, repeating in three directions. We recognize that the defect concentrations accessible to computer simulations are typically much higher than those encountered in experiments.

An alternative approach is the use of cluster models. Here only a finite number of atoms are explicitly considered to describe a part of a solid system whereas the rest of the crystal is treated by embedding techniques. There is an important advantage in the use of clusters in describing point defects — an infinite dilution is considered. Ideally there should be no dependence of the calculated properties on the embedding, size, and shape of the cluster used, thus careful checks have to be performed.

Density functional theory has become a widely used tool for calculations of the properties of solids and molecules, employing both periodic and cluster approaches. Standard implementations of DFT are based on the Kohn–Sham equations and use LDA or GGA for the exchange–correlation functional. Three GGA functionals, namely PW91 [55], PBE [56], and RPBE [57], have been used in studies of oxygen defects in the TM and RE oxide systems considered in this review. A number of failures are known to exist in LDA and *all* currently used GGA functionals, for example the underestimation of band gaps, the gross overestimation of electron delocalization and metallic character, the overestimation of atomization energies of molecules and solids, and the underestimation of energy barriers for molecular reactions. These problems are a consequence of employing approximations to the *unknown* exchange–correlation functional. Another source of error is the lack of exact cancellation of the Coulombic self-interaction, which stabilizes solutions with delocalization of spin density and, as a result, the electronic structure of highly localized magnetic systems is not correctly reproduced. For these reasons, the description of oxygen defects on TM and RE oxide surfaces and in the bulk employing standard DFT is expected to show deficiencies. These will particularly relate to the electronic properties of the reduced systems, specifically, the location of the electrons left in the system upon reduction, the population of specific electronic states by these electrons, resulting in occupied states *in* the band gap, and the actual position of these (defect) states within the gap. Shortcomings are also anticipated in the defect formation energy. In this report we illustrate the merits and limits of local and gradient-corrected functionals as applied to reduced TiO_2, ZrO_2, V_2O_5, and CeO_2 bulk and surfaces.

The above-mentioned inadequacies of GGA functionals can be partly removed by admixture of a fixed amount of Fock exchange to the exchange–correlation functional. These hybrid functionals give significant improvement over GGA for many molecular properties and are very popular in molecular quantum chemistry. Possibly the most widely used hybrid functional is B3LYP [58,59]. Despite the important impact of hybrid functionals on molecular quantum chemistry, their applications to periodic solids used to be linked to Gaussian basis sets (see, e.g., Refs. [23,25,72–77]). Due to progress in plane-wave based algorithms [78,79] and computer speed, hybrid functionals such as HSE03 [80–82] and PBE0 [83–85] have been implemented recently in widely used plane-wave basis set codes [86–89]. The hybrid (periodic and cluster) approach has been successfully applied to selected defective TM oxide surfaces [12,23,25,40]. Compared to GGA functionals, an *improved* description of the electronic

structure and *more accurate* energies have been obtained. The use of cluster models, in particular, allows for the explicit inclusion of correlation effects employing approaches such the Møller–Plesset perturbation theory. The application of such approaches to the electronic structure of point defects at TM or RE oxide surfaces is, however, still rare [90].

A number of more pragmatic approaches have been developed to address the deep seated problems of local and gradient-corrected functionals such as the self-interaction correction (SIC) [91] and the DFT + U approach. This latter method was originally proposed by Anisimov and co-workers [60–63] to account for correlations resulting from strong on-site Coulomb and exchange interactions, as an extension of the LDA approach based on the lessons learned from Hubbard model studies [92–94]. In practice, in these DFT(LDA/GGA)+U approaches one identifies a set of atomic-like orbitals that are treated with an orbital-dependent potential and an associated screened on-site Coulomb and exchange interaction parameter, U and J, respectively [95]. The method, although initially tied to the linear muffin-tin orbital (LMTO) approach, has been reformulated for different basis sets [96–99]. The DFT + U approach has been applied recently to partially reduced RE systems [48–54]. Yet, questions regarding the proper way of specifying the atomic-like orbitals, and of deriving the best value for the so-called effective Hubbard-U parameter ($U' = U - J$) are still under debate.

Last, but not least, generation of the (norm-conserving or ultra-soft) pseudopotentials used in periodic plane-wave calculations (see Refs. [100,101] and references therein) still is a tricky, cumbersome, and error-prone task. Ill-behaved pseudopotentials may affect the description of defective systems, the electronic structure in particular. Yet, deficient pseudopotentials are easily spotted if results are compared to those obtained using all-electron methods. Examples of this and the above-mentioned aspects of calculations on reduced TM and RE oxides systems using different models and methods will be discussed in more detail in following sections.

The average oxygen defect formation energy E_f^{O} is defined as

$$E_f^{\mathrm{O}} = 1/N_{\mathrm{def}}[E_{\mathrm{def}} - E_{\mathrm{free}} + E_{\mathrm{O}}], \quad (1)$$

where E_{def}, E_{free}, and E_{O} represent the total energies of the reduced and defect-free system, and the free oxygen atom, respectively. N_{def} is the number of oxygen defects in the model.

In the following, $E_f^{\frac{1}{2}\mathrm{O}_2}$ indicates the use of the molecular reference energy in Eq. (1), i.e.,

$$E_f^{\frac{1}{2}\mathrm{O}_2} = 1/N_{\mathrm{def}}\left[E_{\mathrm{def}} - E_{\mathrm{free}} + \frac{1}{2}E_{\mathrm{O}_2}\right]. \quad (2)$$

A positive value for $E_f^{\frac{1}{2}\mathrm{O}_2}$ indicates that the vacancy formation is endoenergetic and the difference between E_f^{O} and $E_f^{\frac{1}{2}\mathrm{O}_2}$ is just half the dissociation energy of the O_2 molecule ($E_d^{\frac{1}{2}\mathrm{O}_2}$).

3. Titanium oxide

3.1. TiO_2 applications and basic information

Titanium dioxide is *the* model system in the surface science of TM oxides [2]. It is by far the most extensively studied TM oxide system (see Ref. [102] and references therein). Well ordered, nearly perfect surfaces can be produced relatively easily; it is used as a support of both metal and oxide catalysts, as a photocatalyst, as a gas sensor, as a corrosion-protective coating, and in electric devices such as varistors.

Titanium dioxide crystallizes into three main phases, rutile, anatase, and brookite. However, only rutile and anatase play any role in the applications of TiO_2. In both structures, the basic building block consists of Ti atoms surrounded by six oxygen atoms in a more or less distorted octahedral configuration (see Fig. 1). The bulk unit cell compositions are Ti_2O_4 and Ti_4O_8, respectively. In all three structures, the stacking of the octahedra results in threefold coordinated oxygen atoms. Rutile is the most abundant polymorph in nature. Most crystal growth techniques yield TiO_2 in the rutile phase, thus this phase has been studied extensively. Relative to rutile there are fewer investigations of the anatase phase, although it constitutes most of the commercially produced material. In the following, if the phase is *not* explicitly mentioned, rutile is meant. Both rutile and anatase are insulators with band gaps of 3.0 and 3.2 eV, respectively [103]. Anatase is less dense and less stable than rutile at ambient pressures and temperatures (see Ref. [104] and references therein). The transition temperature depends on a variety of factors including impurities, sample history and crystal size. Indeed, nanocrystalline TiO_2 may be phase selected by controlling the particle size, as well as other experimental conditions such as temperature [105].

The oxygen terminated (110) and (101) oriented (1 × 1) surfaces are the most stable rutile and anatase surfaces, respectively [102,106–108]. Both surfaces have sixfold and fivefold coordinated Ti atoms ($Ti^{(6)}$ and $Ti^{(5)}$), as well as threefold and twofold coordinated O atoms ($O^{(3)}$, $O^{(2)}$, respectively, see Fig. 2). The removal of the latter, so-called bridging oxygen atoms is a subject of much interest and debate.

3.2. Experimental findings on oxygen vacancies

The titanium–oxygen phase diagram is very rich with a variety of crystal structures [109]. When point defects (predominantly oxygen vacancies) are created in the bulk or at surfaces, they cause important changes in the electronic structure that affect the performance of the material in various applications. Consequently, the properties of reduced TiO_2 have been the subject of considerable experimental and theoretical interests [7–19,22,23,25–29]. The sheer number of experimental investigations, in particular, excludes a comprehensive listing, and we refer the reader to the recent review by Diebold [102].

The defect structure of TiO_{2-x} is a complex issue because a family of stable Magnéli phases [110,111] is found to occur between Ti_2O_3 and TiO_2. At low concentrations ($x < 10^{-4}$) the

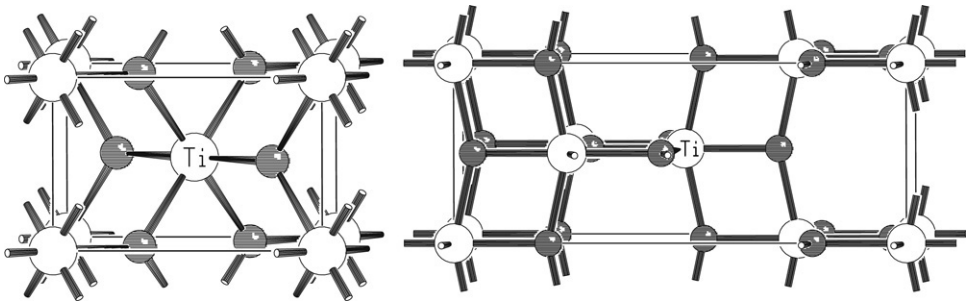

Fig. 1. Bulk structures of rutile (left) and anatase (right) TiO_2 phases.

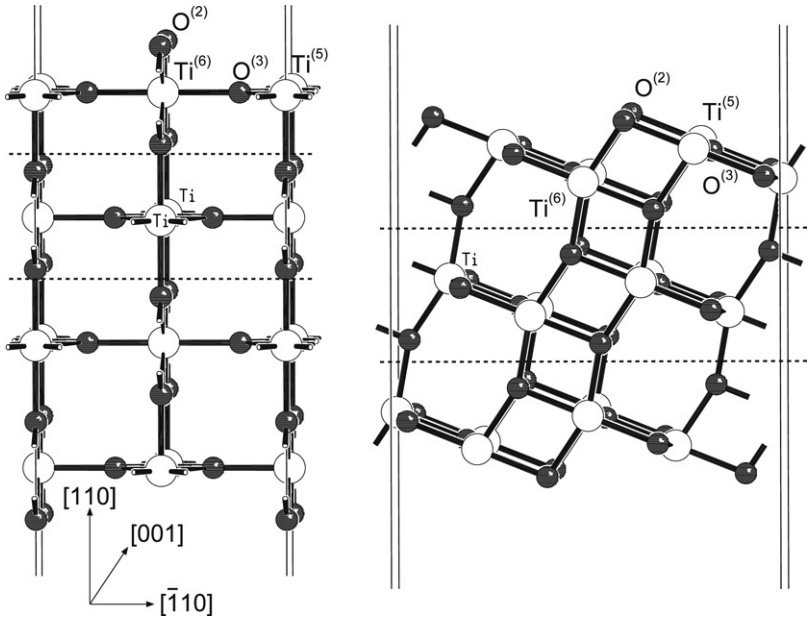

Fig. 2. The bulk truncated (110) and (101) surfaces of rutile (left) and anatase (right), respectively. Shown are four- and three-layer (1 × 1) slabs, respectively. The dotted lines indicate the repeating unit (one-layer) in the direction perpendicular to the surface.

oxygen vacancies are accommodated as point defects while for higher degrees of reduction crystallographic shear (CS) planes are formed, and the point defects eliminated. It is beyond the scope of this work to discuss the formation of CS planes and the most stable structure for a given stoichiometry.

Heating TiO_2 bulk single crystals in vacuum leads to deviations from the 1:2 stoichiometry as firstly reported by Gray et al. [112], and is accompanied by visible color changes from transparent to light and, in turn, dark blue [113]. These deviations were later attributed to conduction electrons trapped at Ti sites forming (electron paramagnetic resonance) EPR-active Ti^{III} species [114]. The EPR studies revealed that darker rutile crystals exhibit higher concentrations of Ti^{III} centers associated to bulk defects such as crystallographic shear planes [113], that may extend all the way to the surface [115]. The characteristic EPR signals attributed to Ti^{III} ions were also observed after excitation of anatase TiO_2 samples with UV light [116], but the signal may disappear at increasing temperature if the particles are small [117]. Reduced TiO_2 crystals exhibit n-type doping, and are widely used in photocatalysis (see Ref. [118] and references therein).

There is overwhelming spectroscopic and chemical evidence for the presence of oxygen defects on (rutile and anatase) samples sputtered and annealed in UHV. These are attributed to bridging oxygen vacancies. Their concentration is reported as several per cent [119,120]. Anatase surfaces show, however, less tendency to release lattice oxygen atoms. For the (110) rutile surface, in particular, scanning tunneling microscopy (STM) has uncovered a large amount of information about oxygen defects in the bridging oxygen [001] oriented rows that includes their diffusion and adsorption on the defective surface [102,121–125]. The latter topic has blossomed after Haruta's discovery [126] that nanosized TiO_2 supported gold clusters exhibit unique catalytic properties [127–129]. It is assumed that the presence of defects on the substrate plays an important role in the catalytic activity (see additional references in the recent survey by Diebold [130]), but experimental evidence has not yet been provided.

Regardless of the location of the oxygen vacancy (i.e., in the bulk or at a surface) the presence of Ti^{III} ions in the reduced systems has been reported. In the following, we summarize the key features of the experimental evidence for their existence

on reduced TiO_2 surfaces. The ultraviolet photoemission spectroscopy (UPS) spectra of single-crystal surfaces contain a band gap feature at ~1 eV below the conduction band edge, which has been interpreted in terms of occupied Ti 3d states [131,132], a view supported by the resonant behavior of UPS across the range of photon energies corresponding to the Ti 3p–3d excitation threshold [133–136]. Moreover, UPS measurements on preparation induced reduced rutile (110) surface (e.g., annealing or Ar bombardment) showed a band gap state at 0.7–0.9 eV below the conduction band [137,138] for low defect concentration that moves towards the bottom of the conduction band as the defect concentration increases [139, 140]. This is consistent with EELS studies [141]; the signature of surface oxygen vacancies is a loss feature at about 0.9 eV. Furthermore, a shoulder in the Ti 2p spectra seen in X-ray photoelectron spectroscopy (XPS) was attributed to Ti^{III} ions, and the lack of surface conductivity also evidence the localized nature of the additional electrons [102].

3.3. Reduced TiO_2 rutile (110) surface

There are two possible types of states that the electrons left in TiO_2 systems (bulk and surface) upon reduction can occupy: delocalized conduction band states (its bottom formed by Ti 3d states) which leads to a metallic ground state, or localized Ti 3d states in the band gap connected with an insulating ground state. The latter type corresponds to the experimental observations. Ti^{IV} ions in titania are in the d^0 state, Ti^{III} ions formed upon oxygen removal are in the d^1 state. The excess charge localization seriously challenges DFT calculations as anticipated in Section 2, and shown next and in Section 3.5.

3.3.1. Structure relaxation and electronic structure

Studies of reduced TiO_2 surfaces using Hartree–Fock or hybrid DFT methods, where the Fock exchange is partially mixed with the DFT exchange, are relatively scarce [8, 12,23,25]. Mackrodt et al. [8] performed spin-unrestricted Hartree–Fock (UHF) calculations [142] of the fully reduced $(1 \times 1)TiO_2(110)$ surface ($\Theta_{def} = 1$) that included relaxation of the surface structure upon reduction. The surface model contained three layers (all were allowed to relax). The term *layer* is used for the repeating O–Ti_2O_2–O unit (see Fig. 2). For other computational details see Table 1. The largest displacements were those of the oxygen atoms in the outermost Ti–O plane, which moved outwards by up to ~0.3 Å.

The UHF calculations led to an antiferromagnetic *insulating*, ground state, i.e., an open-shell singlet. The excess-electron density was located solely at the surface and evenly distributed between the nearest and next-nearest neighbors to the defect. The occupied states associated with the $Ti^{(4)}$ ($Ti^{(6)}$ before defect formation, cf. Fig. 1) and $Ti^{(5)}$ atoms were entirely separated from each other. (Note that the fourfold coordination results of the fact that $\Theta_{def} = 1$). They were located *in* the band gap within ~1–2 eV of the top of the valence band.

Bredow and Pacchioni [12] modelled the isolated defect limit for the $TiO_2(110)$ surface using cluster models, and discussed the defect formation energy (see Section 3.3.2). Clusters of different size were either embedded in point charges (Ti_4O_8 and $Ti_{10}O_{20}$) or terminated by hydrogen atoms [$Ti_4O_8(H_2O)_8$, $Ti_{10}O_{20}(H_2O)_{12}$, $Ti_{17}O_{34}(H_2O)_{19}$]. The oxygen defect was created by removing the central bridging oxygen atom from the surface. The spin-polarized unrestricted (UKS) calculations were performed using two hybrid functionals with 20% and 100% Fock exchange, B3LYP and HFLYP, respectively (Table 1). The structures of the reduced clusters were only partially reoptimized.

Removal of one oxygen atom did *not* result in an open-shell singlet ground state, but in a triplet state (Table 1). For the largest (unrelaxed) system the energy difference between the triplet and closed-shell singlet state was 0.39 eV. The two unpaired electrons were almost equally distributed over the two fivefold ($Ti^{(6)}$ in the defect free surface) nearest neighbors to the defect, and the two next-nearest neighbors ($Ti^{(5)}$), before structure relaxation was considered. However, after relaxation the excess electrons localized almost entirely on the two $Ti^{(5)}$ next-nearest neighbors, probably to reduce electron repulsion. With the HFLYP functional this localization was present even in the unrelaxed structures. Thus, localization is in part connected with the defect-induced structural relaxations. Beyond that, the difference between the B3LYP and HFLYP results confirms the awaited "sensitivity" of the results to the main approximations made.

Zhang et al. [23] considered a fully reduced 5L slab ($\Theta_{def} = 1.0$) and applied the hybrid density functional proposed by Moreira et al. [76] with an admixture of 13% of Fock exchange into spin-polarized LDA. The (empirical) value of 13% was determined by fitting the calculated value of the bulk band gap as a function of the percentage contribution of Fock exchange to the experimental value (3.0 eV). The B3LYP functional (20% exchange) overestimated the band gap by ~0.5 eV. The ground state was a triplet, but the antiferromagnetic solution (open-shell singlet) was only 13 meV less stable. For 13% Fock exchange within LDA, two defect states ~2.4 eV above the top of the valence band were predicted, i.e., approximately 0.6 eV below the conduction band edge (cf. Table 1). The resulting spin density is mainly localized on the $Ti^{(4)}$ ($Ti^{(6)}$ before reduction) and $Ti^{(5)}$ surface atoms, with major $d_{x^2-y^2}$ ($Ti^{(4)}$) and d_{xz} ($Ti^{(5)}$) contributions, however small density contributions are still seen on cations belonging to the layers beneath (see Fig. 3).

Recently, Di Valentin et al. [25] performed spin-polarized calculations using the B3LYP functional for a 4L $c(2 \times 4)$ reduced slab ($\Theta_{def} = 1/4$). The structure was fully relaxed, except for the atoms in the bottom layer which were fixed at their bulk positions. We note that in the $(a' \times b')$ nomenclature of the (reduced) surface unit cells two choices are possible, namely the a'- and b'-axis parallel to the bulk $[\bar{1}10]$ and [001] directions, respectively, or viceversa. Within the former choice the (1×1) surface unit cell has dimensions of $\sqrt{2}a \times c$ with a and c the bulk lattice parameters ($a_{exp} = 4.59$ Å and $c_{exp} = 2.95$ Å) [143]. In the following, we will use this choice as the standard nomenclature and indicate differences (if any) with the original literature.

The $c(2 \times 4)$ structure allows for the possibility of having inequivalent nearest and next-nearest neighbors to the defect.

Table 1
Bridging oxygen defect on TiO_2(110) as obtained by different methods (see Section 3.3.1)

Method[a]	Core-electrons	Basis set	Model[b]	Θ_{def}	Spin state	Electronic structure[c]	References
HF	All-electron	Ti:86-411(d3)G; O:8-411G	3L slab	1	Open-shell singlet	Two occupied defect states ∼1–2 eV above O 2p band *in* the gap; excess electrons localization on all surface Ti atoms	Mackrodt et al. [8]
B3LYP	Ti: ECP[d]	Ti: [8s5p5d/3s3p(2d)]; O: 6-31G	Cluster	Isolated	Triplet	Excess electrons localization on two Ti next-nearest neighbors	Bredow and Pacchioni [12]
Hybrid 13% Fock[e]	All-electron	Ti:86-411(d3)G; O:8-411G	5L	1	Triplet	Two occupied defect states at ∼2.4 eV above O 2p band *in* the gap; excess electrons localization mainly on all surface Ti atoms	Zhang et al. [23]
B3LYP	All-electron	Ti:86-411(d41)G; O:8-411(d1)G	4L	1/4	Triplet	Two occupied defect states at 1.1 and 0.9 eV below the conduction band *in* the gap; the excess electrons remain on one nearest and one next-neareast Ti neighbor	Di Valentin et al. [25]
Non-spin LDA	US PP	340 eV	3L	1/2, 1	Non-spin	Metallic ground state; excess electrons localization mainly at Ti surface atoms	Ramamoorthy et al. [7]
PW91	Kleinman–Bylander	750 eV	3L	1/2, 1	Triplet	Insulating ground states; occupied defect states above O 2p band *in* the gap (e.g., ∼0.7–1.8 eV, $\Theta_{def} = 1$); localization solely at Ti surface atoms ($\Theta_{def} = 1$) and at Ti surface and subsurface atoms ($\Theta_{def} = 1/2$)	Lindan et al. [9]
LDA/PW91	All-electron	LMTO	3L	1	Triplet	Metallic ground state; local magnetic moments 1.2 (Ti under bridging O), 0.6 (fivefold), and $0.2\mu_B$ (subsurface)	Paxton and Thiên-Nga [11]
PW91	US-PP	396 eV	3L	1/3, 1/2	Triplet	Not discussed	Menetrey et al. [13]
PW91	US-PP	396 eV	3L–5L	1/2, 1	Triplet	Electron density gain upon reduction fairly delocalized over the slab	Vijay et al. [15]
PW91	US-PP	396 eV	3L–7L	1/2, 1/4	Triplet	Not discussed	Oviedo et al. [16]
PBE	US-PP	340 eV	4L	1/6, 1/4, 1/2	Triplet	Excess electrons localization primarily at Ti atoms near to the defect	Wu et al. [17]
PW91	US-PP	340 eV	3L–6L	1/6, 1/4, 1/3, 1/2	Triplet	Defect states right below conduction band edge; spread of the excess electrons (after relaxation) with a sizable amount accumulating at the near Ti atoms	Rasmussen et al. [18]

[a] Spin-polarized (unrestricted Kohn–Sham) calculations except otherwise noted; the low spin solution was assumed closed-shell if not mentioned otherwise in the original work.
[b] L (layer) is used for the repeating O–Ti_2O_2–O unit.
[c] In *all* studies electrons left in the system occupied Ti 3d states.
[d] Ti core: $1s^2$ to $2p^6$; O: all-electron.
[e] Hybrid functional [76], 13% Fock-exchange, 87% LDA.

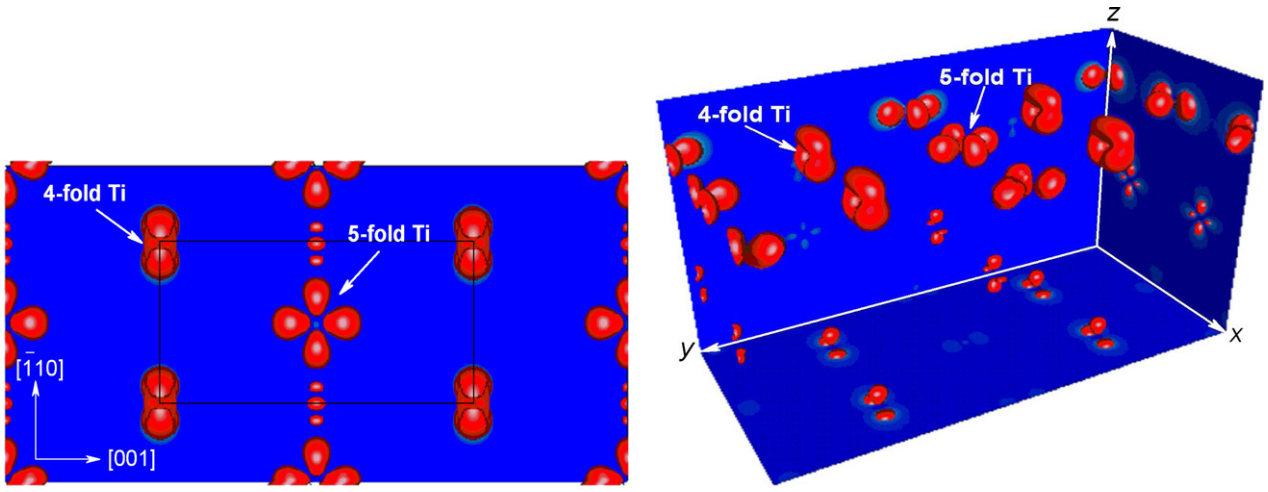

(a) Top view. (b) Side view.

Fig. 3. Distribution of the spin density calculated by hybrid LDA + 13% Fock for the reduced $TiO_2(110)$ (1×1) surfaces. The dashed lines in (a) indicate the surface unit cell, and the distribution on the outermost three layers. Note that the unit cell axis differ from the standard nomenclature. Figure reproduced with permission from Zhang et al. [23].

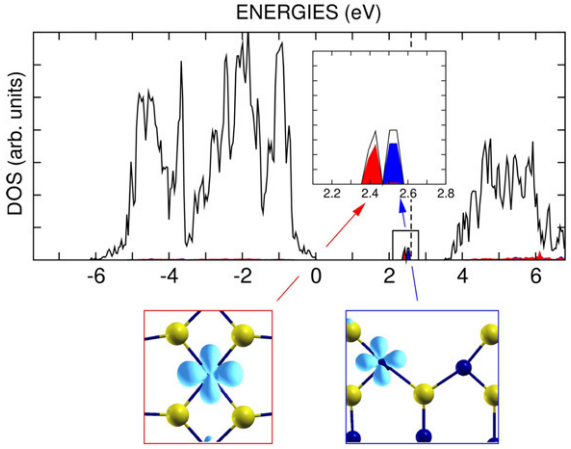

Fig. 4. Spin up-projected density of states of the $c(2 \times 4)$ reduced $TiO_2(110)$ surface, calculated using the B3LYP functional. Blue and yellow spheres indicate titanium and oxygen ions, respectively. The vertical dotted line in the plot denotes the position of the Fermi energy. Figure reproduced with permission from Di Valentin et al. [25].

The results show that rather than localizing on the two next-nearest neighbors ($Ti^{(5)}$) as predicted by Bredow and Pacchioni [12], one electron localizes on a nearest neighbor and the other on a next-nearest neighbor. The reason why the B3LYP cluster and periodic calculations differ may be the limited relaxation considered in the cluster, which signalizes the importance of accounting for full geometry optimization. Fig. 4 shows the spin up-projected total density of states. The states at 1.1 and 0.9 eV below the bottom of the conduction band correspond to the occupied Ti 3d states localized on one $Ti^{(5)}$ and one of the the former $Ti^{(6)}$ atoms, respectively.

The studies reported so far employed cluster or supercell approaches and used exact exchange or a portion of it (cf. Table 1). The same physical picture emerges from all of them: The excess electrons occupy (strictly) *localized* Ti 3d states. The hybrid methods predicted location of these states below the conduction band edge (0.6–1.1 eV) is in fairly good agreement with experimental results (0.7–0.9 eV, cf. Section 3.2). What remains experimentally unresolved is the existence of *two* distinct states.

The LDA and gradient-corrected approximation have been widely and frequently used [7,9–11,13–18,22,28]. The first (non-spin-polarized) self-consistent LDA calculation [144] of reduced $TiO_2(110)$ surfaces was performed by Ramamoorthy et al. [7] They used supercells containing three (3L) and five layer (5L) slabs (for other computational details see Table 1). The attention was focused on the 3L (1×2) and (2×1) supercells, for which only one half of the bridging oxygen atoms were absent ($\Theta_{def} = 1/2$), as well as on the fully reduced (1×1) structure ($\Theta_{def} = 1$). The (2×1) configuration has alternate [001] oriented rows of bridging oxygen defects, whereas the (1×2) has alternate oxygen defects along each such row. The two unit cells differ with respect to the closest distance between defects. For the (1×2) cell this equals $2 \cdot c$ and is twice as large as for the (2×1) cell. Ramamoorthy et al. [7] found the (1×2) structure to be lower in energy by 0.13 eV (3L slab).

Geometry relaxation upon reduction was considered, however, it is likely that only the atoms in the outermost (slab) layer were allowed to move. The resulting (1×1) geometry was very close to that found in Ref. [8], despite those calculations were performed using the UHF approach. In the relaxed (1×2) structure, both surface Ti atoms that were bonded to the removed bridging oxygen were displaced by 0.1 Å *away* from the defect along the [001] direction. Note that for lower defect concentrations than $\Theta_{def} = 1$, the structure relaxations obtained with the LDA or GGA functionals may vary from those obtained with approaches that use exact exchange, in cases in

which the localization of the excess electrons as described by the different functionals differ [25].

The electrons left at the (110) reduced surfaces ($\Theta_{def} = 1/2$, 1) occupy Ti 3d states localized primarily on *all* surface Ti atoms. These states were found *not* to be separated by a gap from the bottom of the conduction band in gross disagreement with experiment.

Lindan et al. [9,10] considered the same systems as Ramamoorthy et al. [7], but performed spin-polarized PW91 calculations. The defect induced surface relaxations were in broad agreement with those of Ref. [7] (largest displacement of ∼0.4 Å for the oxygen atoms in the outermost Ti–O plane), but the (2 × 1) structure was found to be more stable than the (1 × 2) structure by ∼0.2 eV. This corresponds to a difference in surface energy of 0.04 J/m^2, which the authors indicated to be at the limit of accuracy of their calculations.

Lindan et al. [9] found a triplet ground state for all structures investigated (cf. Table 1). Large energy differences between the (closed-shell) singlet and triplet solutions were reported (e.g., ∼3 eV for the (2 × 1) cell). In the following, we assume that the authors did not search for an open-shell singlet solution if they did not mention this explicitly. For the (1 × 1) structure, each surface Ti atom received one electron upon reduction. Fig. 5 shows the corresponding spin-projected total density of states. A band at 0.7–1.8 eV above the top of valence band corresponds to the Ti 3d occupied states. The lowest unoccupied states (not shown) are about 1.9 eV above the valence band edge of the defect free system. Thus, the occupied states are *in* the gap. Although optical properties and band gaps are not ground-state properties, it has become a common practice to compare DFT one electron energies with experimentally measured quasi-particle spectra. It is well-known that the LDA usually underestimates band gaps for semiconductors and insulators [145,146]. For TiO_2 (rutile) the predicted LDA band gap is around 2.0 eV [147–149], (exp.: 3.0 eV). Using gradient-corrected functionals such as PW91 does not necessarily improve the results [150], and the HF approximation yields a band gap that is three times larger than the experimental one [151]. Therefore, we expect that the actual position of defect states within the gap may not be accurately predicted using any of these methods. The deviation between the B3LYP and the experimental band gaps is less severe, as previously mentioned.

For the (2 × 1) configuration the associated occupied Ti 3d states lay 0.2–0.8 eV above the top of valence band *in* the gap, whereas for the (1 × 2) configuration they were higher in energy (0.8–1.5 eV). The spin density distributions showed that no electron localizes on surface Ti atoms that would be fivefold coordinated at the defect-free surface but on one nearest Ti neighbor to the defect ($Ti^{(6)}$ before reduction), and one Ti atom in the middle layer. We note that Lindan et al. [9] indicated the possibility that these reduced systems have multiple minima on the potential energy surface determined by the starting geometry. Namely, once one electron is localized on a Ti ion in the course of structure optimization, subsequent structural relaxation may not be enough to allow the electron to move to another site.

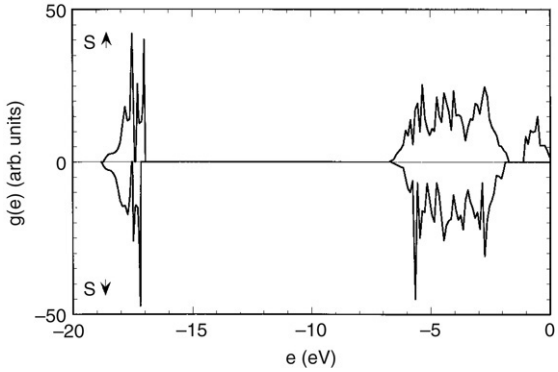

Fig. 5. Spin-projected density of states of the (1×1) reduced TiO_2(110) surface within the PW91 approximation. The zero of the energy scale has been set at the highest occupied energy state. The lowest unoccupied states (not shown) are located at about +0.1 eV. Figure reproduced with permission from Lindan et al. [9].

The existence of gap states is in agreement with the findings using hybrid DFT methods and spin-polarized Hartree–Fock [8,12,23,25], and in *contrast* to those (spin-paired) of Ramamoorthy et al. [7] obtained with *plain* DFT (cf. Table 1). This comparison may suggest that including spin-polarization is necessary *and* sufficient to reproduce the observed n-type semiconducting character of the ground state of reduced TiO_2 systems (cf. Section 3.2). This qualitative agreement between the hybrid and GGA approaches should *not* be assumed to exist always. Nevertheless, it is surprising that non-spin-polarized calculations of oxygen defects at the TiO_2(110) surface are still being published [28].

Paxton and Thiên-Nga [11] applied the spin-polarized *all-electron* full-potential linear muffin-tin orbital (FP-LMTO) [152,153] method to a 3L slab model of the fully reduced (1×1) TiO_2(110) surface. Exchange and correlation was treated within both the LDA [154,155] and PW91 approximations. Both bulk truncated and relaxed atom positions (those reported in Ref. [9]) were considered. In *no* case an occupied state in the band gap was found (cf. Table 1). The Ti local magnetic moments were $1.2\mu_B$ and $0.6\mu_B$ (LDA) for the Ti surface atoms that were sixfold and fivefold coordinated, respectively, at the defect free surface and $0.2\mu_B$ on Ti atoms of the central layer. Thus, the excess electrons were, as a result, to some extent delocalized. The all-electron spin-polarized calculation by Paxton and Thiên-Nga [11] is at odds with that by Lindan et al. [10], however, results obtained using all-electron and pseudopotentials methods (and the same functional) are expected to be (at least) qualitative similar. If not, one should worry about the quality of the pseudopotential used (see later discussion in this section).

A great amount of work [13–19] on reduced TiO_2(110) over recent years, using periodic boundary conditions and ultra-soft pseudopotentials, has led to an understanding of the above-stated disagreements and to an answer to the question: What is the electronic structure of reduced TiO_2 in the context of DFT-GGA methods?

With the recent increase in computational resources, thicker (up to 7L) slabs and lower defect concentrations (up to

Table 2
Selected atomic displacements (in Å) (relative to the positions of the relaxed defect-free surface) upon formation of an oxygen defect in (1 × 4) cell [18]

Atom[a]	Δ_y	Δ_z
O(1)	−0.027	0.007
O(2)	0.043	0.006
O(3)	−0.008	0.122
Ti(4)	−0.225	−0.296
Ti(5)	0.209	−0.298
O(6)	−0.006	0.274
Ti(7)	−0.023	−0.186
Ti(8)	0.020	0.187

$\Delta_x = 0$ for all atoms.
[a] The labels in parenthesis correspond to those in Fig. 6.

$\Theta = 1/6$) have been investigated. The importance of considering thicker systems will become apparent later. Among all periodic studies on reduced TiO_2(110) using gradient-corrected functionals and (ultra-soft) pseudopotentials, the one by Rasmussen et al. [18] is probably the most systematic (and most accurate). They performed spin-polarized PW91 calculations and investigated defect concentrations in the range $1/6 < \Theta_{def} < 1/2$ using slabs of varying thickness (3L–6L) and (1 × 6), (1 × 4), (1 × 3), and (1 × 2), and $c(2 \times 6)$, $c(2 \times 4)$, and $c(2 \times 2)$ unit cells. The centered cells correspond to $\Theta_{def} = 1/6$, 1/4 and 1/2, respectively. At a given concentration, with respect to the distance between defects along the [001] direction (i.e., in the rows) both the primitive and centered cells are identical. However, in the centered cells the periodicity is doubled in the $[\bar{1}10]$ direction (i.e., a') and the two oxygen rows are displaced by b' with respect to each other. (In the original work the orientation of the a' and b' lattice vectors is interchanged.) The use of both primitive and centered cells of increasing size allowed for an estimation of defect interactions along and across the bridging rows (see Section 3.3.2). Geometry relaxations (beyond the first layer) were considered in detail.

Table 2 reproduces the main atomic displacements for the example of the (1 × 4) structure calculated with a four layer slab of which two were relaxed (cf. Fig. 6). The Ti atoms just below the missing O are strongly pushed sideways and down, whereas the O atom below these two Ti atoms are lifted upwards considerably, and relaxations in the second layer are *non*-negligible. The amplitude of the displacement of the oxygen atoms in the outermost Ti–O plane is not as large as previously reported for 3L deficient slabs at $\Theta_{def} = 1/2$ and 1 [7,10]. The importance of atomic relaxations for reduced rutile TiO_2(110) is also apparent in the electronic structure as already mentioned in connection with the results of Bredow and Pacchioni [12] and further discussed next in this section. Nevertheless, information of the atomic structure was not in general provided or was considered in restrictive ways.

Menetrey et al. [13], Vijay et al. [15], and Oviedo et al. [16] performed spin-polarized PW91 calculations [156,157], as Rasmussen et al. [18] (cf. Table 1). The former employed (1 × 3) and (1 × 2) unit cells and a 3L slab for which motions were restricted to the outermost layer. They also reported that removal of bridging oxygen atoms causes substantial changes

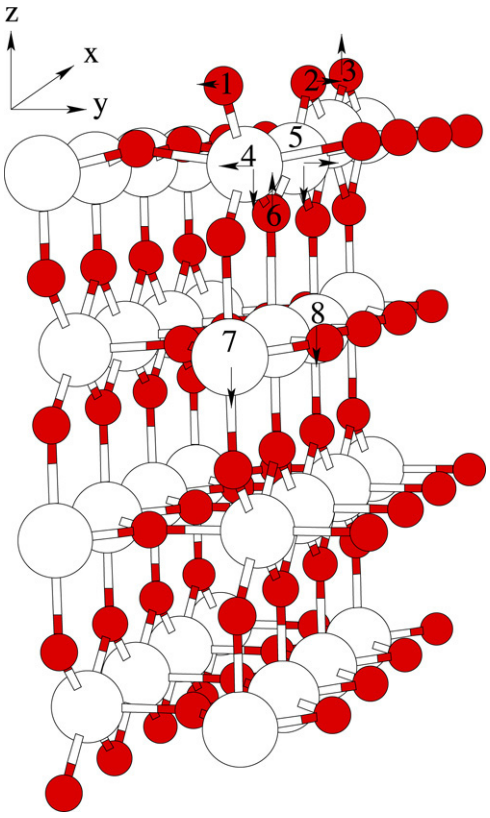

Fig. 6. Illustration of the structural rearrangements upon single defect formation in a (1 × 4) cell ($\Theta_{def} = 1/4$) obtained with PW91. Figure reproduced with permission from Rasmussen et al. [18].

in the positions of the remaining atoms, leading to an increase of the Ti–Ti distance between nearest Ti neighbors to the defect by 0.41 and 0.28 Å for $\Theta_{def} = 1/3$ and 1/2, respectively, in particular. Vijay et al. [15] used a (1 × 2) unit cell and considered both $\Theta_{def} = 1/2$ and 1 with 3–5 layer slabs, whereas Oviedo et al. [16] employed up to 7L slabs and (1 × 2), (2 × 1), and (1 × 4) cells ($\Theta_{def} = 1/2$ and 1/4, respectively). Vijay et al. [15] fixed only the atoms in the bottom layer in their bulk positions, i.e., the number of layers allowed to relax varied with slab thickness. Nevertheless, they only described the movements of the atoms in the outermost layer, which agree with those discussed previously [7,10,13]. Oviedo et al. [16] did not fix any atom in the slabs, but did not report the resulting geometries. Similarly, Wu et al. [17], who performed spin-polarized calculations [158,159] with the PBE functional using (2 × 3), (1 × 4) and (2 × 2), and (1 × 2) unit cells, where all atoms (except those in the bottom slab layer) were allowed to relax, did not describe the atomic displacements.

In these four most recent GGA studies [15–18] the ground states of all oxygen deficient structures considered were triplet (cf. Table 1), in agreement with most of the earlier investigations [9,11–13]. The (spin-paired) singlet state was found to be less favored by a few tenths of an eV (or less) [16,17]. Such difference qualitatively agrees with that obtained in hybrid periodic [23] (∼0.01 eV with respect to the open-shell singlet) and cluster [12] studies (∼0.4 eV), but it is in disagreement with that reported by Lindan et al. [9] (about 3

eV). Moreover, the late GGA calculations that employed (ultrasoft) pseudopotentials, showed a *metallic* ground state [15,17,18] (cf. Table 1). The absence of Ti 3d occupied states *in* the gap is in agreement with the earlier all-electron calculation of Paxton and Thiên-Nga [11], but in contrast to the results of Lindan et al. [9], who used norm-conserving pseudopotentials. It is comforting to see that all-electron and pseudopotential GGA studies do give the same answer. Ref. [18] includes a hint that there may be some problem with the pseudopotential used by Lindan et al. [9]. Nevertheless, while the agreement between recent GGA studies is satisfying, they do *not* reproduce the experimentally observed state in the band gap. Such a state is consistent with the occupation of *localized* Ti 3d states, whereas in the metallic state electrons are obviously delocalized. The extent to which the excess electrons were found to spread over the system differed considerably [15,17,18].

For example, Vijay et al. [15] evaluated the electron density *loss* upon binding of one O atom to reduced (unrelaxed) structures as a qualitative measure of the (de)localization of the excess electrons upon reduction. Thereby assuming that the electron density loss (when the defect is "healed") and gain (when the defect is created) are likely to be similar. They calculated the electron density difference $\Delta_\rho = \rho_{\text{free}} - \rho_{\text{def}} - \rho_{\text{O}}$; ρ_{free} and ρ_{def} are the electron densities of the clean and (unrelaxed) reduced surfaces, respectively, and ρ_{O} that of a free O atom at the defect's position. Δ_ρ is negative in those regions where oxygen bonding induces a depletion of electron density. Fig. 7 shows the result for the example of $\Theta_{\text{def}} = 1/2$ with (1×2) periodicity. The region that is depleted is fairly delocalized over the slab. Therefore, the delocalization of the excess electrons over *many* Ti atoms (i.e., not just those connected to the bridging oxygen) was pointed out.

Rasmussen et al. [18] evaluated the actual changes in charge density upon defect creation and found that structural rearrangements are strongly coupled with important changes in the electronic structure as illustrated next for the example of the defect structure at $\Theta_{\text{def}} = 1/4$. Fig. 8(a) shows the induced charge density changes upon reduction for the (1×4) structure with unrelaxed atoms positions (i.e., equal to those in the relaxed clean TiO_2(110) surface). The excess electrons remained relatively near the defect site mostly at the two closest surface Ti atoms. However, when atoms were allowed to relax (cf. Fig. 8(b)), the excess electrons spread out. The delocalization of the excess electrons increased upon relaxation, however, a sizable amount remained at the nearby Ti atoms. Note the different scales in Fig. 8(a) and (b). Wu et al. [17] also found the two electrons primarily on those Ti atoms. Consistently with these findings, the calculated density of states of the reduced systems shows a defect related occupied state right below the Fermi level, however, *not* separated by a gap from the conduction band as already mentioned.

From the above survey we conclude that the answer to the question on the existence of occupied Ti 3d states in the band gap and the corresponding localization of the excess electrons, depends *strongly* on the exchange–correlation functional used (cf. Table 1). Periodic spin-polarized GGA approaches *failed* to reproduce the splitting of the occupied Ti 3d states from

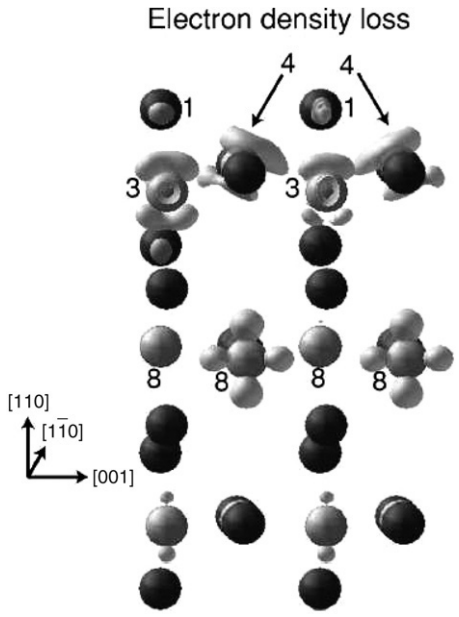

Fig. 7. Electron density loss when defects at the (1×2) reduced TiO_2(110) surface (3L slab) are healed as obtained with PW91. The contour corresponds to $\Delta\rho = -0.040$ electrons/Å^3. Arrows indicate the positions of the former defect Ti nearest neighbors. Note that the unit cell nomenclature is different from that used in Ref. [15]. Figure reproduced with permission from Vijay et al. [15].

the bottom of the conduction band. In contrast, HF, B3LYP, HFLYP, and LDA (13% Fock admixture) calculations, which make use of exact exchange, provided the expected localization independent of the model (cluster or periodic) employed.

The use of different approximations to exchange and correlation lead not only to considerable disagreements in the calculated electronic structure but also to important quantitative differences in the energy for the removal of lattice oxygen as discussed next.

3.3.2. *The rutile TiO_2(110) surface defect formation energy*

Among the hybrid DFT studies on the reduced TiO_2(110) surface, only in that by Bredow and Pacchioni [12] was the energy to form an isolated oxygen defect discussed. They used the oxygen atom as reference (i.e., E_f^{O} in Eq. (1)). The defect formation energy depends strongly on the cluster model used. It was lower when the clusters were embedded in point charges (4.79–4.90 eV, unrelaxed geometries) than for the case of H-termination (from 6.75 to 7.27 eV, also unrelaxed). For the larger $Ti_{17}O_{34}(H_2O)_{19}$ cluster used E_f^{O} is 7.27 eV. If referred to $\frac{1}{2}O_2$ (Eq. (2), with $E_d^{\frac{1}{2}O_2} = 5.20$ eV in B3LYP [12]), the defect formation energy becomes $E_f^{\frac{1}{2}O_2} = 4.67$ eV. Lattice relaxations will lower these values (cf. Table 3). A decrease of 1.95 eV as calculated for the smaller $Ti_{10}O_{20}(H_2O)_{12}$ cluster (obtained in a restricted open-shell calculation), leads to an estimate of $E_f^{\frac{1}{2}O_2} \approx 2.7$ eV for the isolated defect with the B3LYP functional (cf. Table 3).

Menetrey et al. [13], who considered a (thin) 3L slab (allowing only the outermost layer to relax), obtained $E_f^{\text{O}} =$

Table 3

Bridging oxygen defect formation energies at the rutile $TiO_2(110)$ surface, $E_f^{\frac{1}{2}O_2}$ (in eV/atom), as obtained using different methods (see Section 3.3.2)

Method[a]	Core-electrons	Basis set	Model	Cell, Θ_{def}	$E_d^{\frac{1}{2}O_2}$[b]	$E_f^{\frac{1}{2}O_2}$	References
B3LYP	Ti: ECP; O: all-electron	Ti: [8s5p5d/3s3p(2d)]; O: 6-31G	Cluster $Ti_{17}O_{34}$ $(H_2O)_{19}$	Isolated	2.60	∼2.7[c]	Bredow and Pacchioni [12]
PW91	US-PP	396 eV	3L slab	$p(1\times3)1/3$	2.94[d]	2.97[e]	Menetrey et al. [13]
				$p(1\times2)1/2$		4.02[f]	
PW91	US-PP	396 eV	3L 4L 5L	$p(1\times2)1/2$	2.94	3.54 4.53 4.13	Vijay et al. [15]
			3L 4L 5L	$p(1\times2)$ 1		4.10 4.62 4.52	
PBE	US-PP	340 eV	4L	$p(2\times3)1/6$	3.32	3.52	Wu et al. [17]
				$p(1\times4)1/4$		3.55	
				$p(2\times2)1/4$		3.72	
				$p(1\times2)1/2$		4.31	
PW91	US-PP	340 eV	4L	$p(1\times6)1/6$	3.03[g]	3.16	Rasmussen et al. [18]
			4L	$c(2\times6)1/6$		3.03	
			3L 4L 5L 6L	$p(1\times4)1/4$		2.36 3.28 3.16 3.20[h]/(3.12)[i]	
			4L	$c(2\times4)1/4$		3.19	
			3L 4L 5L 6L	$p(1\times3)1/3$		2.59 3.49 3.37 3.43[h]/(3.43)[i]	
			3L 4L 5L 6L	$p(1\times2)1/2$		3.73 4.27 4.26 4.31[h]/(4.25)[i]	
			4L	$c(2\times2)1/2$		4.17	

The effect of lattice relaxations is included.

[a] Spin-polarized (unrestricted Kohn–Sham) calculations.

[b] O_2 molecule dissociation energy (in eV/atom).

[c] $E_f^O = 7.27$ eV for the unrelaxed cluster was reported (cf. Eq. (1)), the relaxation effect (∼2 eV) has been added, and the $E_d^{\frac{1}{2}O_2}$ used to convert E_f^O into $E_f^{\frac{1}{2}O_2}$ (see text).

[d] Ref. [14].

[e] $E_f^O = 8.93$ eV for the unrelaxed structure and a relaxation contribution of 3.03 eV were reported.

[f] $E_f^O = 8.56$ eV for the unrelaxed structure and a relaxation contribution of 1.61 eV were reported.

[g] Ref. [57].

[h] 3L, 4L, 5L, 6L of which 2L were relaxed, respectively.

[i] 6L of which 4L were relaxed.

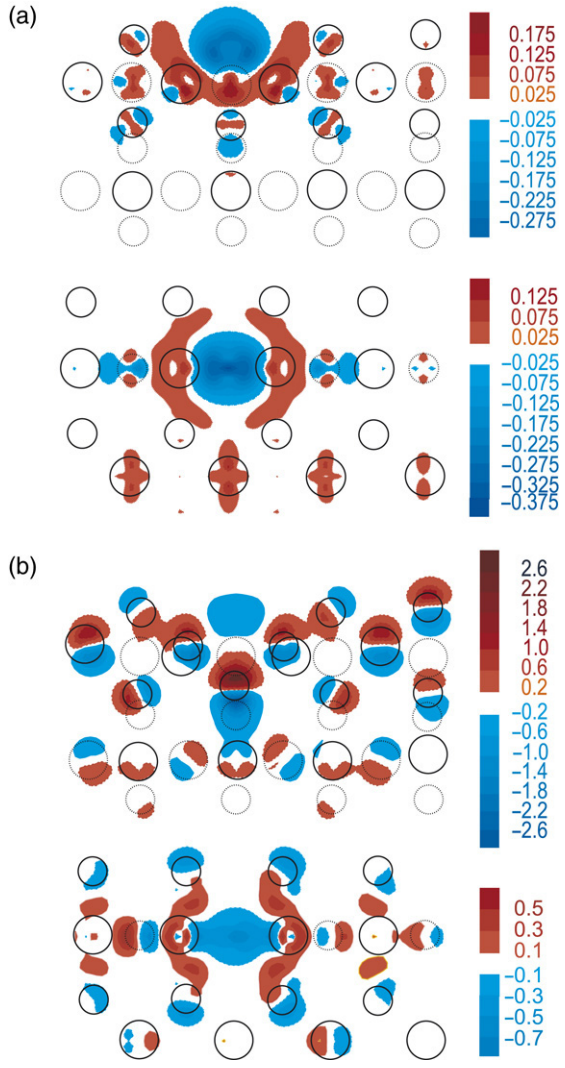

Fig. 8. Change in the charge density upon creation of a single defect in a $p(1 \times 4)$ cell with (a) unrelaxed and (b) relaxed geometries as calculated using PW91. Top, a cut through the slab along the bridging oxygen rows. Bottom, a top view. The induced charge densities were integrated over the perpendicular direction to the plane shown, units are electrons/Å^2. Figure reproduced with permission from Rasmussen et al. [18].

8.93 and 8.56 eV for the (1×3) and (1×2) unrelaxed structures, respectively, using the PW91 functional. Lattice relaxations reduce the defect formation energy (E_f^{O}) to 5.90 and 6.95 eV for $\Theta_{\mathrm{def}} = 1/3$ and $1/2$, respectively. Naturally, including the already described non-negligible relaxations in inner layers, will further reduce the cost to create a defect as discussed later in this section.

Using the value of 5.87 eV for the O_2 dissociation energy [14], calculated within the same computational setup as used in Ref. [13], we obtain (cf. Eq. (2)) $E_f^{\frac{1}{2}\mathrm{O}_2} = 2.97$ eV ($\Theta_{\mathrm{def}} = 1/3$) and 4.02 eV ($\Theta_{\mathrm{def}} = 1/2$, Table 3). These numbers indicate that the interaction between oxygen defects along the [001] rows is markedly repulsive.

Vijay et al. [15] and Oviedo et al. [16] considered the dependence of the defect formation energy on the slab thickness (up to 7L) and defect concentration (as low as $\Theta_{\mathrm{def}} = 1/4$).

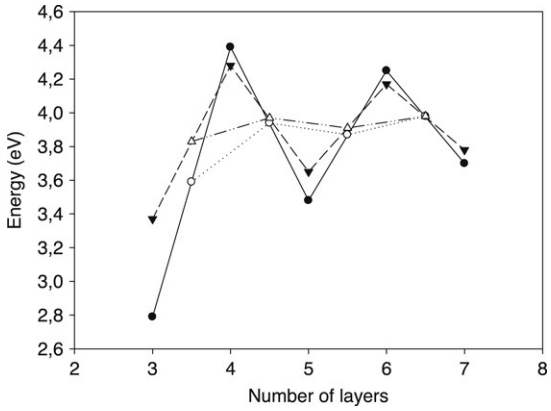

Fig. 9. Defect formation energy $E_f^{\frac{1}{2}\mathrm{O}_2}$ as a function of the layers in the slab for reduced $TiO_2(110)$ surfaces at $\Theta_{\mathrm{def}} = 1/2$ obtained from PW91 calculations. Filled circles and triangles show the calculated values for the (1×2) and (2×1) configurations, respectively. Open symbols correspond to average values between those for odd-layer and even-layer slabs. (Note that the unit cell nomenclature is different from that used in Ref. [16].) Figure reproduced with permission from Oviedo et al. [16].

Before discussing their results, we note here that Ramamoorthy et al. [106] indicated in their earlier studies that when all the atoms in the non-defective slab are allowed to relax, the $TiO_2(110)$ surface energy converged slowly with slab thickness (from three to six), and an oscillatory behavior was reported for the first time. Since then, a number of theoretical works have dealt with this issue [10,15–18,150,160,161]. In the odd-layer slabs there is an extra symmetry of reflection about the plane of the central layer that constrains the relaxation of these slabs in comparison with that of the even-layer slabs. Moreover, in the latter, a bilayer substructuring occurs [150]. As a consequence of these differences, the surface energy oscillates. However, average values between nL and $(n + 1)$L slabs converge much faster. The reason for mentioning this is that such oscillations reappear in the defect formation energies obtained using periodic approaches.

Fig. 9 shows the results of Oviedo et al. [16] for the defect formation energies of $\Theta_{\mathrm{def}} = 1/2$ and two different configurations (all atoms relaxed), and Table 3 summarizes those of Vijay et al. [15] (bottom layer fixed). Both groups found that $E_f^{\frac{1}{2}\mathrm{O}_2}$ oscillates with the number of layers in the slab. This behavior has also been asserted by the PW91 calculations of Rasmussen et al. [18] for $\Theta_{\mathrm{def}} = 1/4$, $1/3$, and $1/2$, and 3L–6L slabs, of which 2L were allowed to relax (Table 3). The amplitude of the oscillations, however, is seen to decrease more rapidly than previously reported (cf. Fig. 9). Indeed, it has been recently shown [161] that fixing some layers at the bottom of the slab reduces the amplitude of the large oscillations in the defect formation energy present in fully relaxed slabs.

These oscillations can cause a significant discrepancy between defect formation energies obtained for thin (e.g., three layers as in Ref. [13]) or thick slabs. Similar to the surface energy, average values converge much faster with the number of slab layers. The results in Fig. 9 suggest that the average value for 4L and 5L slabs (4.5L) yields the converged (average)

value within ∼0.1 eV. Note that the (1 × 2) arrangement was found to be slightly preferred over the (2 × 1) (by about 0.1 eV) in agreement with previous work [7] (cf. Section 3.3.1).

The detailed comparison between calculated defect formation energies by different authors (e.g., Refs. [13,15,16]), even if obtained with the same computational technique (i.e., working with the same code, number of slab layers, and energy cutoff), is not as straightforward as one may expect (cf. Table 3). May be this explains why authors [15,16] do not always compare their results with previously published work. For example, using a 3L slab and a (1 × 2) cell, values of 4.02 eV [13], 3.54 eV [15], and ∼2.8 eV [16] were obtained, a difference within 1.2 eV. The origin of this discrepancy is probably in the subtle computational details such as the vacuum thickness (approximately 6, 15, and 5 Å in Refs. [13] [15], and [16], respectively) and the number of layers in the slab allowed to relax, one (Ref. [13]), two (Ref. [15]) or all (Ref. [16]). Additionally, the *k*-point sampling was not exactly the same, but of similar quality. To fully understand the fairly large discrepancies would require a very laborious testing of the separate effects of a considerable number of technical parameters on the calculated energies. Nevertheless, the differences between average values is expectedly less severe. For 3.5L (average of 3L and 4L) is about 0.4 eV (cf. ∼4.0 and ∼3.6 eV Ref. [15], and Fig. 9, respectively).

Oviedo et al. [16] estimated a value of ∼3 eV for the isolated defect limit for the TiO_2(110) surface with the PW91 functional using the 4.5L value of 3.07 eV from spin-paired calculations employing a (1 × 4) structure ($\Theta_{def} = 1/4$). As previously mentioned, the actual 4L and 5L triplet states are expected to be favored by only a few tenths of an electronvolt (or less) compared to the corresponding closed-shell states.

Wu et al. [17] used 4L thick slabs representing defect concentrations of 1/6, 1/4, and 1/2 with the PBE functional. Thus, the computational method somewhat differs from that of Refs. [13,15,16] (see additional details in Table 3). Two different configurations at $\Theta_{def} = 1/4$ were considered using (1 × 4) and (2 × 2) cells. The defect separation along the (shorter) [001] direction is twice as large ($4 \cdot c$) in the (1 × 4) structure. The defect formation energy of 3.55 eV for the (1 × 4) cell (Table 3) was only by 0.03 eV larger than that for a (2 × 3) cell at $\Theta_{def} = 1/6$. Thus, the (1 × 4) structure appears to be representative of an isolated defect. The value of ∼3.5 eV is, however, by ∼0.5 eV larger than the estimated [16] ∼3 eV using the PW91 functional (and the energies of 4L and 5L calculations at $\Theta_{def} = 1/4$). The use of the different PW91 and PBE functionals does not explain such a significant difference since they are constructed so as to yield essentially the same results for structure, bond dissociation, and adsorption energies [40,56,57].

We recall that the use of a small and even number of layers such as 4L yields overestimated defect formation energies [15,16,18]. For the example of $\Theta_{def} = 1/2$ (see Fig. 9), the values calculated using a fully relaxed 4L slab are ∼0.4 eV larger than the converged (average) values. As already mentioned, the amplitude of the oscillations decreases more rapidly for non-fully relaxed slabs. Hence, the overestimation using 4L of which the bottom layer was held fixed as in Ref. [17], is expected not to exceed a few tenths of an electronvolt. Such correction applied to the value of ∼3.5 eV (4L) for the estimated isolated defect limit in Ref. [17], would bring it closer to the corresponding value of ∼3 eV (4.5L) in Ref. [16].

There are other possible reasons for this dissimilarity that relate to the computational methods. Calculated defect formation energies strongly depend on the ability of the methods to describe the O_2 molecule (cf. Eq. (2)). Hence, at this point, comparing the calculated O_2 dissociation energy ($E_d^{\frac{1}{2}O_2}$) by different implementations of periodic calculations using gradient-corrected functionals (PW91 and PBE) [13,15–18] may be clarifying and instructive. The results in the sixth column of Table 3 show differences up to 0.4 eV/atom. (Differences due to the use of hybrid functionals are discussed later in this section.) We attribute the discrepancy in the dissociation energy (in part) to differences in the pseudopotentials and the cutoff. The O_2 interatomic distance was in all calculations quite well described. For instance, it was 1.24 Å (PBE: Ref. [17] and PW91: Ref. [15]) compared to the experimental value of 1.21 Å (Ref. [162]). The GGA O_2 dissociation energy is overestimated [40,55,56]. The converged PBE and PW91 values (3.12 and 3.10 eV/atom, respectively, Ref. [56]) are very similar and about 0.5 eV larger than the experimental value of 2.59 eV/atom (obtained after adding the contributions due to zero point vibrations to the $T = 0$ K value) [162]. However, the calculated values (Table 3) of 3.32 (PBE: Ref. [17]), 2.94 (PW91: Refs. [13,15,16]), and 3.03 eV/atom (PW91: Ref. [18]) are by ∼0.2 larger and ∼0.2–0.1 eV smaller, respectively, than the corresponding converged (GGA) values. These (fairly large) deviations are likely to "reappear" in the calculated defect formation energies. They are of course independent of those caused by approximations such as different *k*-meshes, slab and vacuum thicknesses, extent of lattice relaxations, etc., but indicative of differences in the pseudopotentials and the cutoff. Hammer et al. [57] have shown that molecular bond energies are particularly sensitive to the details of the pseudopotential. In particular, the choice of the oxygen core radii led to deviations of about 0.2 eV in $E_d^{\frac{1}{2}O_2}$. Hence, variations (by up to a few tenths of an electronvolt) in the oxygen defect formation energies, as calculated using supercells, pseudopotentials, and GGA functionals, resulting (among other reasons) from the arbitrariness in the choice of the pseudopotential, can be expected. This has to be kept in mind when comparing the results in Refs. [13,15–18].

Rasmussen et al. [18] analyzed the dependence of the defect formation energy on the number of layers in the slab (3L–6L), and the number of them that are allowed to relax (1L–4L) in great detail (Table 3). The relaxation of more than 2L led to small differences in vacancy formation energies, e.g., at $\Theta_{def} = 1/2$ for a 6L slab, values of 4.31, 4.29, and 4.25 eV with 2L, 3L, and 4L relaxed, respectively. (The value for a 3L relaxation is not listed in Table 3.) However, for all thicknesses, deviations were larger (up to ∼0.3 eV) if only one layer was allowed to relax [18]. At $\Theta_{def} = 1/2$ and for a 3L slab, values of 4.02 and 3.73 eV were obtained with 1L and 2L relaxed, respectively (not listed in Table 3). The former

agrees well with the corresponding value of Menetrey et al. [13] (cf. Table 3). From the energy dependence on slab thickness and extent of lattice relaxations, we gather that the PW91 results of Rasmussen et al. [18], obtained using 4L slabs (of which two are relaxed), are converged within 0.1–0.2 eV.

As already mentioned, the defect formation energy depends significantly on the defect separation along the [001] rows. The 4L values by Rasmussen et al. [18] for the primitive cells of increasing size are in broad agreement with previously reported trends [16,17]; the defect formation energy decreases by approximately 1.0 eV when Θ_{def} decreases from 1/2 to 1/4 (the distance between defects increases from $2 \cdot c$ to $4 \cdot c$). An additional 0.2–0.1 eV decrease in energy is obtained if the distance between defects increases from $4 \cdot c$ to $6 \cdot c$ (i.e., $\Theta_{\text{def}} = 1/4, 1/6$ in the primitive cells). The use of centered cells at the same defect concentration (cf. $p(1 \times 6)$ and $c(2 \times 6)$) results in an additional decrease of 0.1 eV attributable to defect–defect interactions along the $[\bar{1}10]$ direction (i.e., across the rows). The value of 3.03 eV for the $c(2 \times 6)$ structure at $\Theta_{\text{def}} = 1/6$ represents the isolated defect limit. It is consistent with the previous PW91 estimate of ≈3 eV [16].

Regardless of the discussed variations in the defect formation energies, the recent investigations [13,15–18] using periodic approaches and gradient-corrected functionals (i.e., the *same* computational level), can be considered of comparable quality. We conclude that approximately 3 eV is needed to create a single defect at the (rutile) TiO_2(110) surface, when using gradient-corrected functionals. As already mentioned, the GGA (PW91 or PBE) functionals are known to systematically overestimate bond energies of molecules, cohesive energy of solids, and atomic and molecular bonding to surfaces [40,55–57] and the estimated $E_f^{\frac{1}{2}O_2} \approx 3$ eV is no exception.

The use of hybrid functionals such as B3LYP, which appears to be essential for the proper description of the localization of the excess electrons (Section 3.3.1), reduces the O_2 GGA overbinding by ∼0.5 eV/atom, from 3.12/3.10 eV/atom (PBE/PW91) to 2.60 eV/atom (B3LYP). The deviation of the calculated B3LYP O_2 dissociation energy from experiment [162] (2.59 eV/atom) is one order of magnitude smaller than those of the GGA values. This indicates that *accurate* oxygen defect formation energies can only be expected when hybrid functionals such as B3LYP are used. However, they cannot as yet be efficiently used with fairly large supercells. Therefore, it is still very meaningful to perform hybrid calculations on cluster models of TiO_2 surfaces such as those employed in Ref. [12]. Yet, the quality of the model should be checked using either larger cluster sizes or supercell approaches, but the same functional. This was *not* done in Ref. [12], but would be desirable. Nevertheless, as discussed at the beginning of this section, we estimated (by adding relaxation effects of small clusters to values for unrelaxed larger clusters, Table 3) a value of ∼2.7 eV for the isolated defect formation energy at the B3LYP level, i.e., about 10% less than the (estimated) converged PW91/PBE value. Properly including relaxation effects in the cluster model (and increasing its size) may lead to additional differences.

3.4. Reduced TiO_2 anatase surfaces

As mentioned in Section 3.1, relative to rutile much less is known about anatase surfaces than about rutile surfaces. In correspondence to the rutile (110) surface, the reduced anatase (101) surface obtained by removal of twofold coordinated oxygen atoms ($O^{(2)}$ in Fig. 2) was theoretically investigated [22], however, hybrid studies have not yet been reported.

Vittadini and Selloni [22] simulated a partially reduced (101) surface using a 2L slab and a (1×3) unit cell with the (spin-polarized) PW91 functional. One of the surface bridging oxygen atoms was removed, i.e., $\Theta_{\text{def}} = 1/6$. The term *layer* is used for the repeating O_2–Ti_4O_4–O_2 unit (Fig. 2). Atomic relaxations were allowed with the six outermost TiO_2 units fixed at their bulk positions. The calculated defect formation energy was $E_f^{\frac{1}{2}O_2} = 4.7$ eV.

Recently, Bouzoubaa et al. [14] also carried out spin-polarized PW91 calculations but on the less stable [107] (001) and (100) anatase surfaces that also possess twofold coordinate oxygen atoms. Reduced surfaces were modelled using (2×2) cells and 3L slabs of which 1L and 2L were allowed to relax for the (001) and (100) slab, respectively. The energies of formation of bridging oxygen defects at $\Theta_{\text{def}} = 1/4$ were 4.38 and 4.40 eV for the (001) and (100) surfaces, respectively. As stressed in the previous section, defect formation energies are sensitive to the details of the computational approach. Thus, a direct comparison of these two numbers with that for the (101) surface in Ref. [22] is not very meaningful. Nevertheless, the difference between the energies in Table 4 (anatase surfaces) and Table 3 (rutile surface) is sufficiently large to conclude that oxygen removal from anatase surfaces is more difficult than from the (110) rutile one. This is in agreement with the aforementioned experimentally observed little propensity of anatase surfaces to form oxygen defects under reducing conditions (see Section 3.2). Moreover, it also consistent with an earlier theoretical prediction on the facile reduction of rutile surfaces based on simple electrostatic arguments [163]. We will comment further on this difference in Section 7.

The ground state of the reduced anatase surfaces was a singlet (as before, we assume that authors did not search for an open-shell singlet solution if they did not mention this explicitly). Yet, the triplet is only slightly unfavored (less than 0.01 eV); for the (100) surface it was in fact the triplet favored by that amount (see Table 4). Given these tiny energy differences the spin state of the ground state remains uncertain. In addition, Vittadini and Selloni [22] found that for the unrelaxed (101) reduced surface, the excess electrons were mostly localized on the Ti atoms originally bonded to the removed oxygen atom (cf. Fig. 10) and that actually the triplet was slightly favored. When the structure was relaxed, the singlet became the ground state with the excess electrons spreading over *all* surface cations. This relaxation induced distribution of the excess electrons is largely similar to the results in Fig. 8 for the rutile TiO_2(110) surface. We observe that relaxations lead to additional delocalization of the excess electrons when gradient-corrected functionals, whereas the use

Table 4

Bridging oxygen defect formation energies, $E_f^{\frac{1}{2}O_2}$ (in eV/atom), at anatase TiO_2 surfaces and associated changes in the electronic structure (see Section 3.4)

Surfaces	Method[a]	Core-electrons	Basis set (eV)	Model	Cell, Θ_{def}	Spin state	Electronic structure	$E_f^{\frac{1}{2}O_2}$	References
(101)	PW91	US-PP	340	2L	$p(1 \times 3)1/6$	Singlet	Spread of the excess electrons (after relaxation) over all surface Ti atoms	4.70	Vittadini and Selloni [22]
(001)	PW91	US-PP	396	3L	$p(2 \times 2)1/4$	Singlet	Not discussed	4.38	Bouzoubaa et al. [14]
(100)	PW91	US-PP	396	3L	$p(2 \times 2)1/4$	Triplet[b]	Not discussed	4.40	Bouzoubaa et al. [14]

The effect of lattice relaxations is included.

[a] Spin-polarized (unrestricted Kohn–Sham) calculations except otherwise noted; the low spin solution was assumed closed-shell if not mentioned otherwise in the original work.

[b] The closed-shell singlet state is less favored by ~0.01 eV.

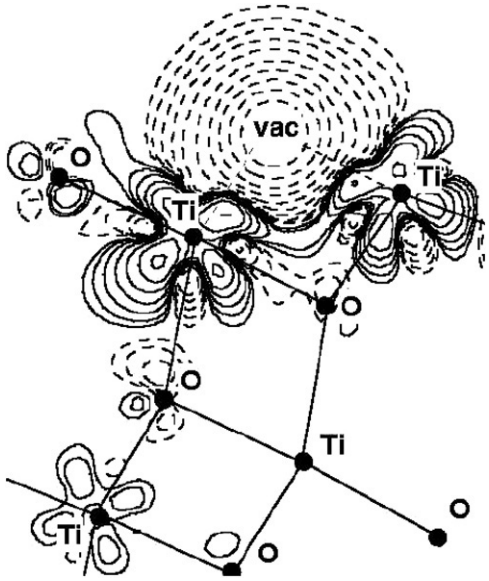

Fig. 10. Change in the charge density upon creation of a single defect at the (1×3) anatase $TiO_2(101)$ surface with unrelaxed geometry as calculated using PW91. Contour levels of charge depletion are dashed. The singlet state is shown. Figures reproduced with permission from Vittadini et al. [22].

of hybrid functionals (B3LYP, Refs. [12] and [25]) to additional localization (see Section 3.3.1).

3.5. Reduced rutile and anatase TiO_2 bulk

While there have been many theoretical investigations of oxygen defects at TiO_2 surfaces, relatively few studies have dealt with such defects in the bulk phases [7–9,14,26,27,29], of which *none* employed hybrid approaches; Mackrodt et al. [8] used spin-unrestricted Hartree–Fock, and the others used the LDA or gradient-corrected functionals [7,9,14,26,27,29].

Consistently with the findings for the surface oxygen defects, only the UHF calculated electronic structure of the reduced TiO_2 bulk shows defect related occupied states *in* the gap (Table 5). The results of the periodic spin-polarized PW91 calculations of Lindan et al. [9] do not agree with those of recent GGA studies [26,29], as they employed norm conserving pseudopotentials [164] that may have had problems [18].

Mackrodt et al. [8] modelled an oxygen deficient rutile TiO_2 bulk using a supercell of composition Ti_8O_{16}. In this configuration defects are surrounded by a single unit cell of non-defective crystal only in two directions, whereas lines of defects are formed in the *c*-direction. It is likely that atomic relaxations upon defect formation were considered, however, were not discussed.

Unlike in their surface studies (cf. Section 3.3.1), they used Gaussian basis sets with and without oxygen functions at the vacant site. Both sets led to an *insulating*, triplet spin-polarized ground-state and the appearance of states *in* the band gap located ∼1–2 eV above the top of the valence band. This is similar to their surface result as obtained without functions at the vacant site. The most significant difference is, however, that for the surface the UHF calculations predicted an antiferromagnetic spin arrangement, i.e., an open-shell singlet. The ground state of the reduced bulk as derived from the calculation with basis functions at the vacancy was lower in energy by 1.4 eV. In the latter, most of the excess-electron density was localized at the vacancy site with the rest asymmetrically distributed between the nearest and next-nearest Ti atoms. The net spin-population was 0.8 (vacant site), 1.0, and 0.2, respectively. The occupied states formed two well separated features in the gap. In the absence of vacancy functions, the excess electrons were mostly localized at the cation sites, whereas the rest was distributed among three O atoms. The spin-populations at both Ti (nearest and next-nearest) sites were ∼1.0.

Whereas in the earlier LDA investigation of Ramamoorthy et al. [7] spin polarization was not considered, in the recent LDA and GGA studies the ground state was triplet for the $(2 \times 2 \times 2)$ and singlet for the bigger $(2 \times 2 \times 3)$ and $(3 \times 3 \times 5)$ cells (Table 5) [14,26,29]. As before, we assume that the authors did not search for an open-shell singlet solution unless it is explicitly stated otherwise. In all cases, the energy difference between the ground state (closed-shell singlet or triplet) and the less favored magnetic state was found not to exceed 0.05 eV. Such small energy difference does not allow for a definite statement on the magnetic ground state of the reduced rutile phase at low defect concentrations. These four investigations considered geometry relaxation upon reduction. However, in Ref. [14] only the positions of the three metal atoms close to the oxygen defect were allowed to relax. The outward displacement of the neighboring Ti atoms to the defect was reported, namely, by ∼0.1 (Ref. [7]) and ∼0.3 Å (Ref. [26]). Furthermore, a *metallic* ground state was found with local and gradient-corrected functionals [7,26,29]. In reality, when atoms of the $(3 \times 3 \times 5)$ cell were fixed at their bulk position, a defect state *in* the gap was obtained with LDA [26]. This relaxation induced delocalization of the excess electrons in reduced TiO_2 systems had been previously observed in GGA studies of reduced TiO_2 surfaces [18,22] (Sections 3.4 and 3.3.1).

Bouzoubaa et al. [14] reported a PW91 defect formation energy of 4.52 eV using a $(2 \times 2 \times 2)$ cell, whereas we obtained 4.43 eV using a $(2 \times 2 \times 3)$ cell (Table 5) [29]. The latter agrees well with the previously reported PBE value (4.40 eV) at the same defect concentration [27]. As already mentioned, to quantitatively discuss the dependence of $E_f^{\frac{1}{2}O_2}$ on the defect concentration, besides the varying cell sizes, the used methodology has to be identical (i.e., same pseudopotentials and cutoff, equivalent *k*-point meshes, etc.). The comparison between our calculated $E_f^{\frac{1}{2}O_2}$ values for the $(2 \times 2 \times 3)$ and $(3 \times 3 \times 5)$ cells indicates that the interaction between oxygen defects is repulsive. However, bigger supercells have to considered to get the value for the isolated defect limit. The values of 4.1–4.4 eV/atom for rutile lies in the range of 3.9–5.7 eV/atom, obtained in thermogravimetric studies of defective rutile TiO_x with $x = 0.0015$–0.024 [165]. The use of GGA functionals such as PW91 can explain an *over*estimation of up to ∼1 eV of bond energies of 3d TM compounds [166].

Table 5

Oxygen defect formation energies, $E_f^{\frac{1}{2}O_2}$ (in eV/atom), in bulk TiO_2 phases and associated changes in the electronic structure

Method[b]	Core-electrons	Basis set	Unit cell	Spin state	Electronic structure	$E_f^{\frac{1}{2}O_2}$	References
Rutile							
HF	All-electron	Ti:86-411(d3)G; O:8-411G	Ti_8O_{16}, $(2 \times 2 \times 1)$	Triplet	Insulating ground state; excess electrons localization mostly at the vacancy site. Occupation of states ∼1–2 eV above O 2p band *in* the gap	–	Mackrodt et al. [8]
PW91	Kleinman–Bylander	750 eV	$Ti_{16}O_{32}$, $(2 \times 2 \times 2)$	Triplet	Insulating ground state. Population of states ∼1.3–1.9 eV above O 2p band *in* the gap; electron localization at the three closest Ti atoms	–	Lindan et al. [9]
Non-spin LDA	US-PP	340 eV	Ti_4O_8, $(1 \times 1 \times 2)$	non-spin	No gap between occupied Ti 3d levels and conduction band	–	Ramamoorthy et al. [7]
LDA	PAW[c]	400 eV	$Ti_{90}O_{180}$, $(3 \times 3 \times 5)$	Singlet	Metallic ground state; defect state in the gap before relaxation	4.44	Cho et al. [26]
PW91	US-PP	396 eV	$Ti_{16}O_{32}$, $(2 \times 2 \times 2)$	Triplet[d]	Not discussed	4.52	Bouzoubaa et al. [14]
PBE	US-PP	340 eV	$Ti_{24}O_{48}$, $(2 \times 2 \times 3)$	Not discussed	Not discussed	4.40	Di Valentin et al. [27]
PW91	PAW	400 eV	$Ti_{24}O_{48}$, $(2 \times 2 \times 3)$	Singlet[e]	Metallic ground state	4.43	Hofmann et al. [29]
			$Ti_{90}O_{180}$, $(3 \times 3 \times 5)$	Singlet[e]		4.05	
Anatase							
PW91	US-PP	396 eV	$Ti_{32}O_{64}$, $(2 \times 2 \times 2)$	Singlet[e]	Not discussed	5.29	Bouzoubaa et al. [14]
PBE	US-PP	340 eV	$Ti_{32}O_{64}$, $(2\sqrt{2} \times 2\sqrt{2} \times 1)$	Not discussed	Not discussed	4.20	Di Valentin et al. [27]
PW91	PAW	400 eV	$Ti_{16}O_{32}$, $(2 \times 2 \times 1)$	Singlet	Metallic ground state	4.89	Hofmann et al. [29]
			$Ti_{32}O_{64}$, $(2\sqrt{2} \times 2\sqrt{2} \times 1)$	Singlet		4.27	

The effect of lattice relaxations is included[a].

[a] In some studies the inclusion of geometry relaxations upon reduction was neither explicitly mentioned nor denied (see Section 3.5).

[b] Spin-polarized (unrestricted Kohn–Sham) calculations except otherwise noted; the low spin solution was assumed closed-shell if not mentioned otherwise in the original work.

[c] Projector augmented wave method [302,303].

[d] The singlet state is less favored by less than ∼0.05 eV.

[e] The triplet state is less favored by less than ∼0.05 eV.

Bouzoubaa et al. [14], Di Valentin et al. [27], and Hofmann et al. [29] also performed calculations to investigate oxygen defects in anatase with supercells of composition $Ti_{32}O_{64}$. The latter considered a smaller cell ($Ti_{16}O_{32}$) as well. Similar to the rutile phase, the interaction between defects is repulsive (Table 5). The ground state is a (spin-paired) singlet; the energy difference between the singlet and triplet states is small (∼0.1 eV). As already mentioned, the more facile formation of defects at rutile than at anatase surfaces has been observed. The comparison of the $E_f^{\frac{1}{2}O_2}$ values obtained for the rutile and anatase bulk phases using the $(3 \times 3 \times 5)$ and $(2\sqrt{2} \times 2\sqrt{2} \times 1)$ cells, respectively, indicates that a similar behavior for defects in the bulk may be expected (cf. 4.05 (rutile) with 4.27 eV (anatase) in Table 5).

3.6. Summary TiO_2

Much has been learned about the changes in the geometry and electronic structure upon defect formation in the rutile TiO_2 crystal and at its (110) oriented surface in recent years. The knowledge about anatase systems is less deep.

The relaxation patterns are complex, for the rutile TiO_2(110) surface in particular, with atomic displacements of up to ∼0.3 Å perpendicular to the surface as found with gradient-corrected functionals. Sizeable relaxations extend up to the two outermost slab layers. They lead to a considerable surface buckling and a "wider" defect site. The optimal geometry with hybrid approaches has not been discussed in detail yet, but it is likely to somewhat differ from the GGA one.

Spin-polarized DFT (periodic) within the LDA or GGA approximations *fails* to correctly describe the experimentally observed localized nature of the excess electrons in reduced TiO_2 systems, resulting in metallic ground states. This is valid for both, all-electron and (ultra-soft) pseudopotentials approaches. For the rutile TiO_2(110) surface in particular, the localization of the excess electrons have been corroborated by theoretical studies at the HF level (periodic) and employing (periodic and clusters) hybrid approaches, namely, HFLYP, B3LYP, and one that combines an empirically fitted percentage of exact exchange with LDA (13% Fock). Both B3LYP and the hybrid LDA + 13% Fock give the position of the occupied Ti 3d states upon reduction below the bottom of the conduction band (0.6–1.1 eV) close to experiment. The answer onto which Ti ions the two excess electrons localize for a single defect (surrounded by at least a neighboring shell of non-defective material), depends on the model with B3LYP. Either on the two next-nearest neighbors ($Ti^{(5)}$) to the defect (partially reoptimized cluster) or one electron localizes on a nearest ($Ti^{(6)}$ in the clean surface) and the other on a next-nearest neighbor (fully optimized $c(2 \times 4)$ slab). In addition, when considering clusters and the B3LYP functional the excess electrons localized *only* if atomic displacements were considered, whereas relaxation in defective supercells (bulk and surfaces) with GGA functionals led to an increase in the extent of the delocalization of the excess electrons. These results show the importance of both exact exchange and lattice relaxations for the proper description of the electronic structure. It would be desirable to perform a GGA calculation using the optimized B3LYP geometry and viceversa as recently done for the hydroxylated TiO_2(110) surface [27].

For the reduced bulk phases, the energy difference between the triplet and closed-shell singlet is less than 0.05 eV (PW91), i.e., the two spin states have virtually the same energy. The defective anatase surfaces show a similar behavior, with singlet [(001), (101)] and triplet [(100)] ground states. For the (relaxed) defective rutile TiO_2(110) supercells, the closed-shell singlet is 0.05–0.1 eV above the triplet (PW91/PBE), whereas it is 0.4 eV in the absence of relaxation of a cluster model with B3LYP. Hybrid LDA+13% Fock predicts an energy difference between the triplet and open-shell singlet states which is no more than a few millielectronvolts for a (relaxed) defective slab ($\Theta_{def} = 1$).

The cost to create a defect depends on the model and on the approximations to exchange and correlation. Using slabs and gradient-corrected functionals, independently of the defect concentration, the average defect formation energy oscillates on the rutile TiO_2(110) surface with the number of slab layers. A minimum of 4L of which (not less than) 2L are relaxed appears to give results converged within ∼0.1–0.2 eV.

The TiO_2(110) surface defect interactions are repulsive and fairly strong along the [001] direction. A centered (2×6) cell is representative of the isolated defect limit. Its formation energy is estimated to be ≈3.0 eV (PW91 functional). Using cluster models (that included relaxations in a limited way) and the B3LYP functional, a value of ≈2.7 eV has been estimated. This number may decrease when larger and relaxed clusters are considered. The database of the energies for creating defects at the rutile TiO_2(110) surface is very large. However, *no* study of the defect formation energy, aiming beyond gradient-corrected functionals with proper account for geometry relaxation, have been carried out for reduced TiO_2 yet.

The few defect formation energy values available for anatase systems are larger than those for rutile and are consistent with the experimentally observed lower tendency of anatase to release atomic oxygen under reducing conditions.

4. Zirconium oxide

4.1. ZrO_2 applications and basic information

Zirconia-based ceramics are used in a variety of technological and commercial applications, ranging from thermal barrier coatings on aircraft turbines to affordable diamond substitutes [167,168]. Recently, zirconia has received attention as an alternative dielectrics to silicon dioxide for memory and logic devices [169]. The versatility of zirconia originates entirely from atomic or point defects in the crystal created by adding aliovalent oxides, e.g., MgO, La_2O_3, and Y_2O_3. The substitutional cations or dopants that are charge balanced by the formation of oxygen vacancies, and their mutual interactions, dramatically affect the structural, thermal, mechanical, and electrical properties of modified or stabilized zirconia (SZ). These defects are solely responsible for the high ionic conductivity of doped zirconia that underlies its use in oxygen sensors [170], and high-temperature fuel cells [171]. Zirconia is also used as a support material in heterogeneous catalysis [172].

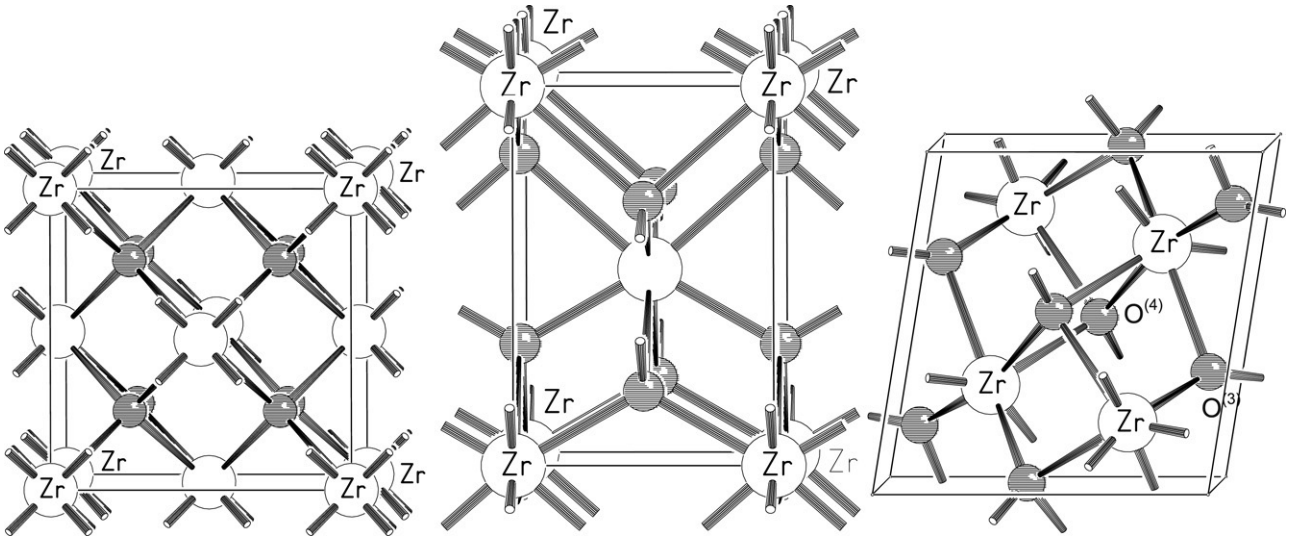

Fig. 11. Bulk structure of the three cubic, tetragonal, and monoclinic ZrO_2 polymorphs. Small and large circles represent the oxygen and zirconium atoms, respectively. (a) c-ZrO_2, (b) t-ZrO_2, and (c) m-ZrO_2.

Pure ZrO_2 adopts the monoclinic baddelyte structure (m-ZrO_2) under ambient conditions [173,174], with Zr in a distorted sevenfold coordination and O atoms are either fourfold or threefold coordinated (see Fig. 11). Above ∼1400 K, it transforms to a tetragonally distorted fluorite structure (t-ZrO_2) [175], with Zr surrounded by eight anions, but with two slightly different Zr–O distances. Perfect eightfold coordination is achieved at ∼2600 K with a transformation to the cubic fluorite structured phase (c-ZrO_2) [176]. However, the presence of dopants stabilizes the tetragonal and cubic modifications, even at room temperature. Oxygen atoms in the tetragonal and cubic phases are fourfold coordinated.

The three phases are insulators. The reported experimental band gap values for the monoclinic phase are 4.2 eV (Ref. [177] obtained by EELS), and 5.8–7.1 eV (Ref. [178] obtained by vacuum–ultraviolet spectroscopy). The VUV reflectance method tends to overestimate the value of band gaps. The amount by which the band gap of the c-ZrO_2 and t-ZrO_2 phases differs from that of the m-ZrO_2 phase is not resolved experimentally. Values (VUV) of 6.1–7.1 (c-ZrO_2) and 5.8–6.6 eV (t-ZrO_2) were reported [178].

From experimental studies on polycrystalline samples of t-ZrO_2 it is known that only a few low-index crystal planes are preferentially exposed, with the (101) face being the most favored [179]. Theoretical investigations on the stability of different surface orientations support this observation. The (101) oxygen terminated surface is by far the most stable (see Fig. 12) followed by the (001) face, also oxygen terminated [35,180–182]. (Note that the orientation of the surfaces is named differently in Ref. [180].) The oxygen atoms at these surfaces are threefold coordinated (cf. fourfold in bulk). The t-ZrO_2(101) surface exhibits two different types of oxygen atoms.

4.2. Experimental findings on oxygen vacancies

As titania, stabilized zirconia becomes colored when exposed at high temperature to a reducing atmosphere, and a pronounced room-temperature electron spin or paramagnetic resonance (ESR/EPR) signal appears [183], suggesting the existence of *trapped* electrons. A great deal of experimental work has been dedicated to the study and characterization of defects in SZ using electron paramagnetic resonance, optical absorption, and photoemission techniques [184–188]. Although in ZrO_2 oxygen vacancies are commonly introduced deliberately by adding stabilizing low-valence metal ions, undoped ZrO_2 may contain a significant concentration of oxygen vacancies [189,190]. Experimental investigations of the electronic structure of polycrystalline *pure* ZrO_2 and its changes upon reduction by Ar bombardment using photoemission spectroscopy have identified significant changes in the O 2p band and the appearance of occupied electronic states *in* the band gap at 2.3 eV above the top of the valence band [191,192]. These states have been assigned to electrons populating Zr 4d orbitals of adjacent cations to the oxygen defects.

4.3. Reduced ZrO_2 bulk phases

Point defects in modified or stabilized zirconia systems have been extremely topical in theoretical studies (see e.g., Refs. [30, 182,193–202]), which focus on ion mobility [30,199–201], thermal properties [197,198], and the interactions between the dopant cations and oxygen vacancies [194–196].

State-of-the-art computational methods have been also used to model reduced undoped zirconia systems [29–35], bulk phases in particular. Relative to the bulk, there are fewer investigations of reduced zirconia surfaces [29,33–35]. Oxygen induced lattice relaxation, the question whether the electrons left in the system occupy the vacant site or localize at neighboring cations, and the energy of oxygen removal have been addressed. Different exchange–correlation functionals have been applied, including the LDA and PW91, as well as B3LYP. The use of the hybrid approach was limited to just the defect formation energy of t-ZrO_2 systems.

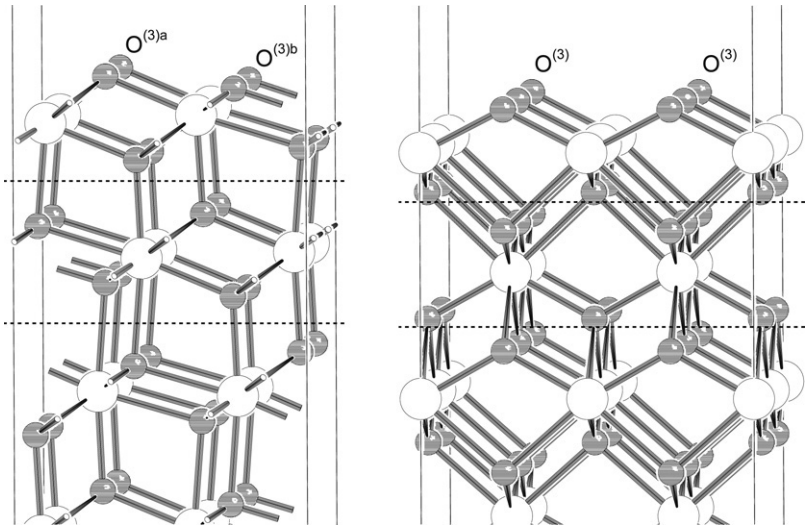

Fig. 12. The bulk truncated (left) t-ZrO_2(101) (1 × 2) and (right) t-ZrO_2(001) (2 × 2) surface slab. Small and large circles represent the oxygen and zirconium atoms, respectively. Only the three outermost slab layers are completely shown. The dotted lines indicate the repeating unit (one-layer) in the direction perpendicular to the surface.

4.3.1. Structure relaxation and electronic structure

Foster et al. [31,32] considered the *monoclinic* zirconia phase. They performed spin-polarized PW91 calculations and investigated an (isolated) oxygen defect in a (2 × 2 × 2) cell ($Zr_{32}O_{64}$, 96 atoms) allowing for ∼10 Å separation between the periodic images of the defect. The cell parameters were taken from calculations for the defect free material that deviated by less than 1% from the experimental values (a_{exp} = 5.15 Å, b_{exp}/a_{exp} = 1.01, c_{exp}/a_{exp} = 1.03, β = 99.23°) [203]. The positions of all atoms in the unit cell were allowed to relax. Removal of both fourfold and threefold coordinated oxygen atoms, denoted as $O^{(4)}$ and $O^{(3)}$, respectively, was considered. In both cases, formation of a neutral oxygen defect led to *small* relaxations of the neighboring Zr atoms with displacements of about 0.01–0.02 Å from the perfect crystal positions. The corresponding relaxation energy was 0.11 eV.

The neutral $O^{(3)}$ and $O^{(4)}$ vacancies have a doubly occupied one-electron level *in* the gap. In the following, as before, we understand that authors did not look for an open-shell singlet solution unless they clearly stated it. The main properties of both types of defects are very similar and the details below are given in terms of the $O^{(4)}$ defect. The defect charge density is strongly localized with a maximum at the center of the vacancy and can be described as a bonding combination of atomic orbitals of all four Zr atoms neighboring the vacant site. The defect state is ∼2.2 eV above the top of the valence band *in* the gap. The difference in total energy of the defective supercell (for the fixed geometry of the relaxed singlet) and the triplet state is ∼1.2 eV above the (closed-shell) singlet. We recall that for the reduced TiO_2 bulk phases, energy differences between these two spin states are by about two orders of magnitude smaller (few tenths of a millielectronvolt, see Section 3.5).

Foster et al. [31] also considered a singly and doubly positively charged vacancy. Lattice relaxation effects were larger than for the neutral defect. For instance, for the singly charged defect, the four Zr neighbors moved away from the vacancy by about 0.1 Å and the relaxation energy was 0.47 eV. The spin density map of the positively charged $O^{(4)}$ oxygen defect, $O^{(4)+}$, is displayed in Fig. 13. It clearly shows that the remaining electron is (also) strongly localized at the defect site and demonstrates contributions of Zr d-orbitals.

The strong localization of the electron density at the defect site and the behavior of the lattice relaxation are qualitatively similar to those for neutral and charged oxygen vacancies in MgO [65,67,69]. This type of defects in MgO are known as F, F^+, and F^{2+} *color centers*, depending on their charge [204]. Therefore, differently charged oxygen defects in zirconia are loosely attributed in the literature to the class of F centers.

As anticipated, the band gap of monoclinic ZrO_2 was significantly underestimated in agreement with previous GGA studies [205] (cf. 3.4 eV with the experimental values in the 4.2–7.1 eV range, Section 4.1). The same obviously applies to the cubic and tetragonal phases with GGA calculated band gaps of 3.1 (c-ZrO_2, Ref. [205]) and 3.9 and 4.2 eV (t-ZrO_2, Refs. [30,205]). (The corresponding experimental values are 6.1–7.1 (c-ZrO_2) and 5.8–6.6 eV (t-ZrO_2), Section 4.1.) We note in passing that the use of the LDA together with the so-called GW approximation for the electron self-energy [206,207], improves the agreement between theory and experiment considerably. In this approximation, the self-energy is the product of the single-particle Green function G and the screened Coulomb interaction W. The GW values are 5.42 (m-ZrO_2), 5.55 c-ZrO_2, and 6.40 eV (t-ZrO_2) [33]. The position of the defect state ∼2.2 eV above the top of the valence band in m-ZrO_2 [31], is likely to move if methods which do give more accurate band gaps are used [208].

Králik et al. [33] considered *cubic* zirconia using the LDA together with the GW approximation. The calculated LDA structural parameters compared well (within ∼1%) to the experimental value (a_{exp} = 5.09 Å) [203]. The study of oxygen defects in cubic zirconia employed a (2 × 2 × 1) supercell consisting of four formula units. The internal coordinates of all atoms were allowed to relax with LDA. As for the monoclinic phase, the defect induced displacements of the neighboring

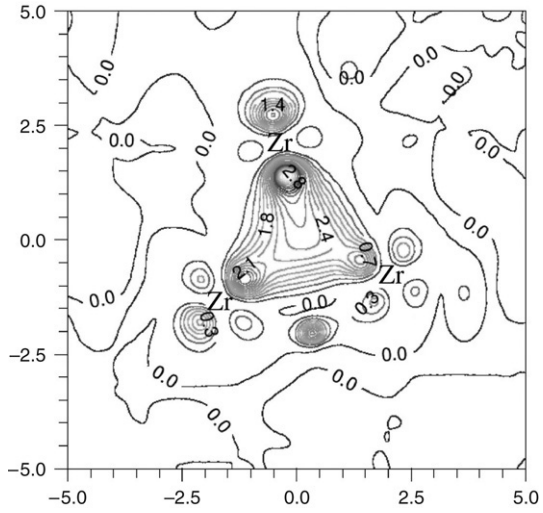

Fig. 13. Spin density map in the plane through three Zr ions neighboring the positively charged oxygen defect $O^{(4)+}$ in m-ZrO_2 obtained with PW91. The defect is at the center. The density is in 0.1 e/Å and the distances in Å. Figure reproduced with permission from Foster et al. [31].

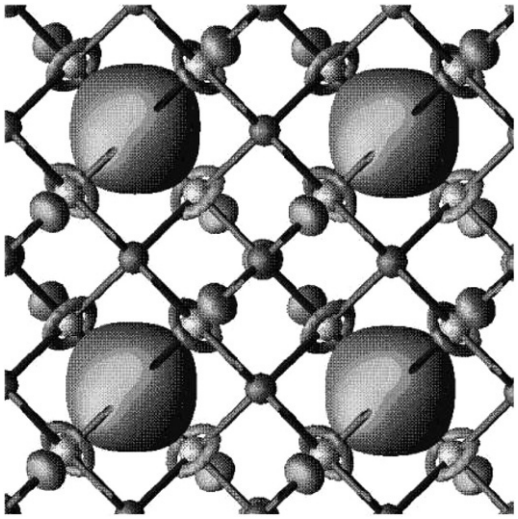

Fig. 14. Isosurface of the square of the vacancy wave function of cubic ZrO_2 obtained with LDA, superimposed on a ball and stick model of the supercell used. The large balloon-shaped structures are localized at the O vacancy sites. Figure reproduced with permission from Králik et al. [33].

Zr atoms were small (∼0.02 Å). A fully occupied state, well separated from both the valence and conduction bands, was found *in* the band gap 2.1 eV below the conduction band edge with the GW approximation. The defect state is formed by a linear combination of Zr d-orbitals. Fig. 14 shows the square of the wave function associated to the defect state. This plot reveals that indeed Zr d_{z^2} orbitals give the dominant contribution to the state and that it is mostly localized at the vacant site.

Oxygen vacancies in *tetragonal* ZrO_2 were considered by several authors [29,30,34]. Eichler [30] and Hofmann et al. [29] performed spin-polarized PW91 calculations on periodic models [156,157]. Calculated structural parameters agreed within 1% with experiment (a_{exp} = 3.64 Å, c_{exp}/a_{exp} = 1.45) [175].

For the investigation of O defects in t-ZrO_2, Eichler [30] used a (3 × 3 × 2) supercell ($Zr_{36}O_{72}$), whereas Hofmann et al. [29] used (2 × 2 × 2) and (3 × 3 × 3) cells with composition $Zr_{16}O_{32}$ and $Zr_{54}O_{108}$, respectively. As for the monoclinic and cubic phases, (neutral) defect induced lattice relaxations are small (up to 0.08 and 0.13 Å for Zr and O ions, respectively) with an energy gain of 0.22 eV, as reported by Eichler [30]. Hofmann's calculations yielded very similar atomic displacements from the ideal bulk positions and a relaxation energy of 0.17 and 0.51 eV for the (2 × 2 × 2) and (3 × 3 × 3) supercell, respectively [29].

According to both calculations, the ground state of the reduced systems is a singlet and a doubly occupied state shows up *in* the band gap (see e.g., Fig. 15). The energy difference between the closed-shell singlet and the triplet states (for relaxed geometries) are 0.94 and 0.85 eV for the defective $Zr_{16}O_{32}$ and $Zr_{54}O_{108}$ cell, respectively. This is similar to the aforementioned result for monoclinic phase (1.2 eV).

The spin projected total density of states (DOS) of Hofmann et al. [29] for the pure and reduced t-ZrO_2 in both spin states are compared in Fig. 15. In the singlet state, the peak at 2.8 eV (∼2.5 eV in Ref. [30]) above the valence band results from the partial occupation of Zr 4d orbitals (see Fig. 15(b)). Its position relative to the valence band edge is in fairly good agreement with that observed in reduced polycrystalline surfaces (2.3 eV) [192]. The charge density isosurface associated to the vacancy state is visualized in real space in Fig. 16. The two electrons are trapped in the vacancy. In contrast, in the triplet state, the excess electrons delocalize by partially "leaving" the vacant site to occupy conduction band states, which are primarily localized on the neighboring Zr atoms to the defect (cf. Fig. 15).

Safonov et al. [34] performed embedded cluster calculations of an oxygen defect in t-ZrO_2 using Hartree–Fock and the B3LYP exchange–correlation functional. The Zr_4O_{23} cluster involved one central atom (that was removed to form the bulk defect) and its first and second coordination spheres. The cluster was embedded in a field of point charges located at the zirconia lattice positions. The coordinates of all cluster atoms were allowed to relax (at the Hartree–Fock level). The oxygen basis set was retained at the defect site (see Table 6). The Zr–O distances in the optimized cluster were 2.09 and 2.44 Å, in agreement with the experimental values of 2.09 and 2.42 Å, respectively. The vacancy induced lattice relaxations were below 0.03 and up to 0.22 Å for Zr and O ions, respectively, values similar to those obtained in the periodic PW91 calculations [29,30]. Safonov et al. [34] did not explicitly state whether the ground state of the defective bulk is a singlet or a triplet and whether the two electrons remained at the defect site.

From the periodic calculations on reduced bulk ZrO_2 discussed so far, we gather that gradient-corrected functionals are indeed able to describe the localization of the excess electrons and the appearance of a doubly occupied state *in* the gap qualitatively (see Table 6). This is in contrast to reduced TiO_2 systems for which the use of exact exchange happened

Table 6

Oxygen defect formation energies, $E_f^{\frac{1}{2}O_2}$ (in eV/atom), in zirconia systems and associated changes in the electronic structure (see Sections 4.3 and 4.4)

Bulk	Method[a]	Core-electrons	Basis set	Unit cell	Defect	Spin state	Electronic structure[b]	$E_d^{\frac{1}{2}O_2}$[c]	$E_f^{\frac{1}{2}O_2}$	References
m-ZrO_2	PW91	US-PP	396 eV	$Zr_{32}O_{64}$, $(2\times2\times2)$	$O^{(4)}$	Singlet	State at 2.2 eV above O 2p band	2.94	5.94	Foster et al. [31,32]
					$O^{(3)}$	Singlet			5.96	
c-ZrO_2	LDA/GW	PP[d]	1360 eV	Zr_4O_8, $(1\times1\times1)$	$O^{(4)}$	Singlet	State at 2.1 eV below the conduction band	–	–	Králik et al. [33]
t-ZrO_2	PW91	PAW[e]	250 eV	$Zr_{36}O_{72}$, $(3\times3\times2)$	$O^{(4)}$	Singlet	State at ∼2.5 eV above O 2p band		5.73	Eichler [30]
	PW91	PAW	400 eV	$Zr_{16}O_{32}$, $(2\times2\times2)$	$O^{(4)}$	Singlet		3.13	5.92	Hofmann et al. [29]
				$Zr_{54}O_{108}$, $(3\times3\times3)$	$O^{(4)}$	Singlet	State at ∼2.8 eV above O 2p band		5.41	
	HF/B3LYP	Zr: ECP[f]	Zr: LANL2DZ; O: 6-31G/6-311G*[g]	Zr_4O_{23}, Cluster	$O^{(4)}$	–	Not discussed	2.7	6.1	Safonov et al. [34]
Surfaces	Method	Core-electrons	Basis set	Model	Cell, Θ_{def}	Spin state		$E_d^{\frac{1}{2}O_2}$	$E_f^{\frac{1}{2}O_2}$	References
t-ZrO_2(101)	PW91	USPP	380 eV	5L	$p(1\times1)$ 1/2	–	State at ∼2.7 eV above O 2p band	–	–	Hofmann et al. [35]
t-ZrO_2(101)	PW91	PAW	400 eV	5L	$p(2\times4)$ 1/16	Singlet	State at ∼2.9 eV above O 2p band	3.13	5.48	Hofmann et al. [29]
t-ZrO_2(101)	HF/B3LYP	Zr: ECP[f]; O: all-electron	Zr: LANL2DZ; O: 6-31G/6-31G*[g]	Cluster	$Zr_{35}O_{61}$	Singlet	Not discussed	2.7	5.7	Safonov et al. [34]
t-ZrO_2(001)	HF/B3LYP	Zr: ECP[f]; O: all-electron	Zr: LANL2DZ; O: 6-31G/6-31G*[g]	Cluster	$Zr_{25}O_{50}$	Triplet[h]	Not discussed		6.4	Safonov et al. [34]

The effect of lattice relaxations is included.

[a] Spin-polarized (unrestricted Kohn–Sham) calculations except otherwise noted; the low spin solution was assumed closed-shell if not mentioned otherwise in the original work.

[b] In *all* studies the ground state is insulating, the electrons left in the system occupy a linear combination of Zr 4d states *in* the band gap, and the excess charge is localized at the defect site.

[c] O_2 molecule dissociation energy (in eV/atom).

[d] Troullier–Martins and Hamman–Schluter–Chiang for O and Zr atoms, respectively.

[e] Projector augmented wave method [302,303].

[f] Zr core: $1s^2$ to $3d^{10}$; O: all-electron.

[g] In single-point B3LYP calculations the more flexible 6-311G* basis was used for the central O atom.

[h] The singlet state is less favored by about ∼0.01 eV.

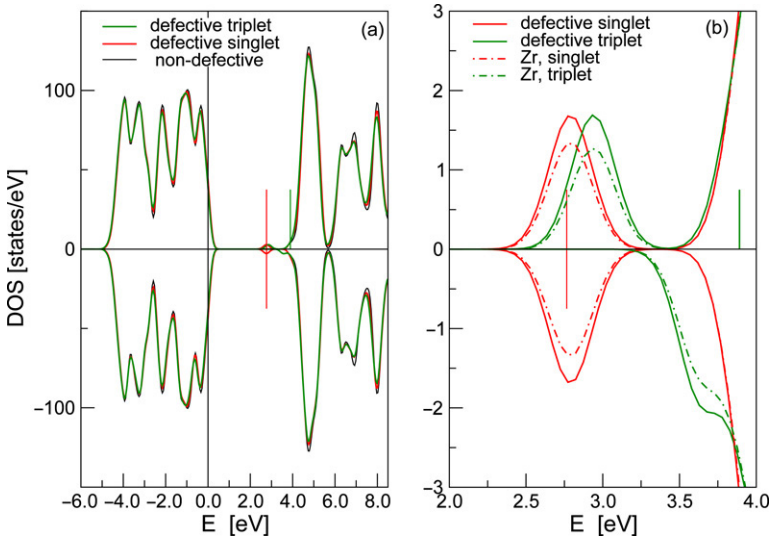

Fig. 15. Total (PW91) spin-projected density of states (DOS) (α-spin > 0, β-spin < 0) of (a) a t-$ZrO_2(3 \times 3 \times 3)$ bulk cell ($Zr_{54}O_{108}$) with a single oxygen defect in the singlet (red) and triplet state (green). The DOS of the defect free cell is shown as a reference (black). The energy zero is set to the top of the O 2p band, and the vertical lines indicate the highest occupied state. (b) Zoom into the region near the conduction band edge. The Zr contributions are plotted separately (dashed-dotted lines). The curves are smoothed by a Gaussian level broadening of 0.2 eV.

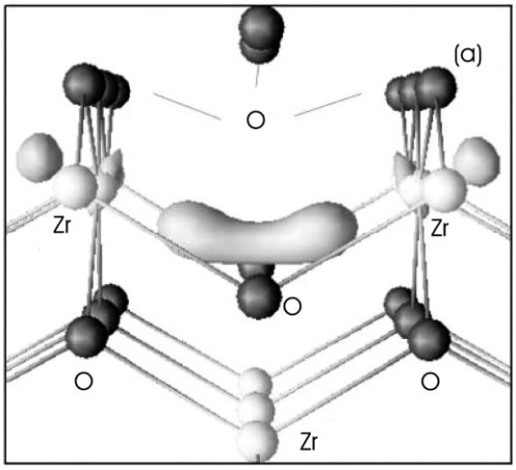

Fig. 16. Charge density isosurface of the defect state in reduced t-ZrO_2 from PW91 calculations. Figure reproduced with permission from Eichler [30]. © 2001, by the American Physical Society.

to be essential to avoid a metallic ground state using GGA functionals.

The relevant questions are why the excess electrons are trapped at the vacant site, and why GGA functionals yield a proper (qualitative) description of the defect's nature. The first question can be understood qualitatively. In ZrO_2, similarly to MgO [70,209], the excess electrons experience a fairly attractive Madelung potential favoring their stabilization at the vacant site, and the ground state is a (closed-shell) singlet. For instance, the Madelung potential at the $O^{(4)}$ site (cf. Fig. 11) in bulk t-ZrO_2, obtained from the Ewald summation assuming GGA (PW91) self-consistently calculated charges, equals -12.4 V [29]. We note that for the titania phases we have calculated values which are by approximately 4 V *less* attractive, whereas for MgO is -20.1 V (see Section 7 for further discussion and comparisons). As to the second question, in ZrO_2, the effect of the gross overestimation of electron delocalization and metallic character of gradient-corrected functionals is not too prominent because of its fairly wide band gap.

4.3.2. *The ZrO_2 bulk defect formation energy*

Foster et al. [31,32] calculated the defect formation energy of both fourfold and threefold coordinated oxygen atoms from the monoclinic phase. The E_f^O (cf. Eq. (1)) values were 8.88 ($O^{(4)}$) and 8.90 ($O^{(3)}$), respectively (PW91). These numbers refer to the singlet state. Using their calculated dissociation energy of the O_2 molecule value of 5.88 eV, they obtained 5.94 and 5.96 eV for $E_f^{\frac{1}{2}O_2}$ (cf. Eq. (2)), respectively (cf. Table 6).

The calculated PW91 $E_f^{\frac{1}{2}O_2}$ values for the tetragonal bulk phase were 5.92 eV [29], 5.73 eV [30], and 5.41 eV [29] for the $(2 \times 2 \times 2)$, $(3 \times 3 \times 2)$ and $(3 \times 3 \times 3)$ cell, respectively. The 0.51 eV decrease in the defect formation energy with the increase in the unit cell size from the $(2 \times 2 \times 2)$ to $(3 \times 3 \times 3)$ indicates repulsive interactions between closest defects. No systematic periodic study aiming at the isolated defect limit in ZrO_2 systems has been carried out yet.

According to the embedded cluster B3LYP calculations in Ref. [34], the vacancy formation energy in the t-ZrO_2 phase is $E_f^{\frac{1}{2}O_2} = 6.1$ eV ($E_f^O = 8.8$ eV). Safonov et al. [34] argued that the ~0.4 eV deviation from the value previously obtained by Eichler using periodic models and the PW91 functional (5.73 eV) [30], was an indication of the good quality of the cluster model and other details of the calculation (e.g., basis set). Because different functionals were used, this conclusion is a priori *not* justified. In addition, oxygen defect formation energies are almost certainly going to be *over*estimated with PW91 for models of similar quality, which the above comparison does *not* show.

4.4. Reduced t-ZrO_2 surfaces

As mentioned above, relative to the reduced bulk ZrO_2 phases much less is known about their surfaces. In fact, only defective t-ZrO_2(101) and (001) surfaces were investigated. These correspond to the most and second most stable orientations (cf. Section 4.1).

Hofmann et al. [35] carried out periodic spin-polarized PW91 calculations on the reduced (relaxed) t-ZrO_2(101) (1×1) surface at $\Theta_{\text{def}} = 1/2$ ($O^{(3)a}$ defect) using a 5L slab (see Fig. 12). The electronic structure resembles that of the bulk system with the occupied state in the gap at 2.7 eV above the valence band and the excess electrons localized at the defect site (cf. Fig. 16).

Recently, Hofmann et al. [29] considered a lower concentration of $O^{(3)a}$ defects, namely $\Theta_{\text{def}} = 1/16$. The vacancy induced displacements were small (up to 0.2 Å) with the adjacent Zr atoms moving *away* from the defect site. After reduction a doubly occupied state appeared *in* the gap at 2.9 eV above the valence band. The (closed-shell) singlet state is favored by about 0.08 eV, i.e., approximately two orders of magnitude less than for the bulk (cf. Section 4.3.2). The calculated surface $O^{(3)a}$ defect formation energy ($E_f^{\frac{1}{2}O_2}$) for $\Theta_{\text{def}} = 1/16$ is 5.48 eV.

Similar to the bulk results in Section 4.3.1, admixture of exact exchange to the exchange–correlation functional is *not* required to achieve the localization of the excess electrons and to obtain a doubly occupied state in the gap of the reduced t-ZrO_2(101) surface.

Safonov et al. [34] investigated the formation of isolated oxygen defects at the t-ZrO_2(101) and (001) surfaces using cluster models ($Zr_{35}O_{61}$ and $Zr_{25}O_{50}$, respectively) embedded in a set of point charges. The spin-polarized calculations were performed using the HF approach and the B3LYP functional (other details in Table 6). Lattice relaxations upon defect formation were considered and somewhat smaller displacements for the stable (101) surface (0.1–0.2 Å) than for the (001) orientation (0.2 Å) were reported. For the (101) surface the singlet state was preferred by 0.1 eV in agreement with the periodic PW91 calculations (cf. Table 6) [29,35], whereas for the (001) surface the triplet and singlet states differed by 0.01 eV. The B3LYP defect formation energies were 5.7 and 6.4 eV for (101) and (001), respectively. The former is close to the value obtained with periodic PW91 calculations (5.48 eV) [29]. As already discussed, this "agreement" does *not* necessarily validate the cluster models used; comparisons have to be made using the same exchange–correlation functional. Note that according to the B3LYP cluster calculations, the surface defect is more favorable than the bulk defect by ~0.4 eV for the (101) surface and less favorable for the (001) surface by a similar amount (cf. Table 6). With respect to the PW91 t-ZrO_2 bulk value of 5.41 eV ($3\times3\times3$), the (101) surface defects ($\Theta_{\text{def}} = 1/16$) have also a comparable stability. A systematic study aiming at both isolated surface and bulk limits would be desirable.

4.5. Summary ZrO_2

Less is known about oxygen defects in pure zirconia, surfaces in particular, than about defects in titania. One reason is that mostly doped or stabilized zirconia is used in industrial applications.

Both periodic (PW91) and cluster (B3LYP) approaches predict *small* and rather localized lattice relaxations on formation of neutral oxygen defects in ZrO_2 systems with atomic displacements of up to 0.1–0.2 Å. The excess electron density is localized at the vacant site and a partial reduction of the neighboring Zr sites is observed. The electrons populate a state *in* the band gap formed mainly by a linear combination of Zr 4d orbitals. For most zirconia systems, the (closed-shell) singlet state is more stable than the triplet state by up to a few tenths of an electronvolt, independent of the model (periodic or cluster) and the method (PW91 or B3LYP). The little relaxation and the trapped electrons resemble the F-centers in ionic oxides such as MgO, for which the inclusion of exact exchange is *not* essential for their proper description. The existence of occupied states in the wide-gap of ZrO_2 is reproduced with local and gradient-corrected functionals.

The PW91 functional predicts defect formation energies values in the 5.4–5.9 eV range for $O^{(4)}$ defects in the t-ZrO_2 and m-ZrO_2 bulk phases, with the largest values corresponding to m-ZrO_2. The t-ZrO_2(101) surface defect has similar stability in comparison to the bulk. Existing (cluster) B3LYP results for ZrO_2 systems are not conclusive due to the presumed inadequacy of the model, and the question of the energy to form the oxygen defects with hybrid functionals remains unanswered.

TiO_2 and ZrO_2 clearly represent two different cases of TM oxides with respect to the nature of the oxygen defects.

5. Vanadium oxide

5.1. Applications and basic information

Vanadium oxides are used in many technological applications such as in electrical and optical switching devices, light detectors, critical temperature sensors, and heterogeneous catalysis [2,210]. All solid oxide catalysts used at an industrial scale for production of organic anhydrides and acids contain vanadium as the main active component [211]. Since in oxides vanadium can have four different oxidation states, namely II, III, IV, and V, a wide range of stable bulk vanadia phases exists. The fundamental basis for the catalytic performance of vanadium oxides lies in the variability of their geometric and electronic structures.

The maximal valency oxide is V_2O_5. It exhibits an optical band gap of ~2.3 eV and is orange [212,213]. Bulk V_2O_5 has a layered structure and orthorhombic symmetry [214] ($a_{\text{exp}} = 11.51$, $b_{\text{exp}} = 3.56$, $c_{\text{exp}} = 4.37$ Å). There are three structurally different oxygen atoms in each layer, vanadyl oxygen ($O^{(1)}$), coordinated to one vanadium atom, bridging oxygen atoms ($O^{(2)}$), and two inequivalent threefold coordinated oxygen atoms ($O^{(3)}$ and $O^{(3')}$), see Fig. 17. The

layers are bound by weak van der Waals type interactions, thus forming a solid material which can be easily cleaved along the (001) plane without rupture of any covalent bond. Hence, the coordination of neither the oxygen nor vanadium atoms (distorted octahedron) changes upon formation of the (001) surface, which is the most stable. It is terminated by vanadyl groups which form up and down oriented double rows parallel to the [010] direction (Fig. 17).

Vanadia catalysts are usually synthesized as V_2O_5, but are reduced to lower oxides under reaction conditions. The catalytic behavior of vanadia in several oxidation reactions has been discussed based on the Mars and van Krevelen mechanism [215], which decouples the oxidation of the adsorptive from the reoxidation of the catalyst. Lattice oxygen is considered as a reactive intermediate [216,217]. Thus, the energy needed for creating lattice oxygen defects at V_2O_5 surfaces is of particular relevance, and reducibility is an important factor allowing this oxide to function as a catalyst in selective oxidation.

The interest in the lower oxides, namely VO_2, V_2O_3 and VO, is much centered around phase transitions and magnetism, and less around their reducibility. In particular the focus is on metal–insulator transitions as a function of temperature, which display peculiar structural, electronic and magnetic behavior that remain yet to be understood [210]. Thus, in the following we will restrict the discussion to the formation of oxygen defects in V_2O_5.

5.2. Experimental findings on oxygen vacancies

The vanadium–oxygen phase diagram is, like in the titanium–oxygen case, very rich and Magnéli phases also occur. Known superstructures of V_2O_5 resulting from oxygen loss are V_3O_7, V_4O_9, and V_6O_{13} [218].

There have been several photoemission studies of the clean and reduced V_2O_5(001) surfaces [219–221]. V_2O_5(001) is easily reduced by low-energy particle bombardment and thermal annealing, and it is very sensitive to all probing beams (see also Refs. [222–227]). It has been frequently claimed that the surface vanadyl oxygen atoms are the oxygen atoms easiest to remove. However, Tepper et al. [220] suggested that the surface oxygen defects formed after exposure to atomic hydrogen are likely to be the bridging oxygen atoms ($O^{(2)}$).

In the earlier studies by Zhang and Henrich [219], the electronic structure of the UHV-cleaved V_2O_5(001) surface was found to be similar to that of the bulk, namely, the UPS spectra showed that the V 3d band was unoccupied ($3d^0$ configuration) and the bottom of the O 2p valence band at about 2.5 eV below the Fermi level (consistent with the existence of an optical bulk band gap of ∼2.3 eV). When the clean surface was bombarded by low-energy electrons, oxygen defects were created, leading to reduced cations on the surface. UPS spectra of such reduced surfaces exhibited an occupied peak ∼1 eV below the Fermi energy (*in* the bulk band gap) due to partial population of the 3d orbitals on reduced vanadium ions. According to accompanying XPS measurements, V^{IV} centers were primarily present at the reduced surface [219]. We note here (and discuss in the next section) that under the assumption that surface vanadyl oxygen

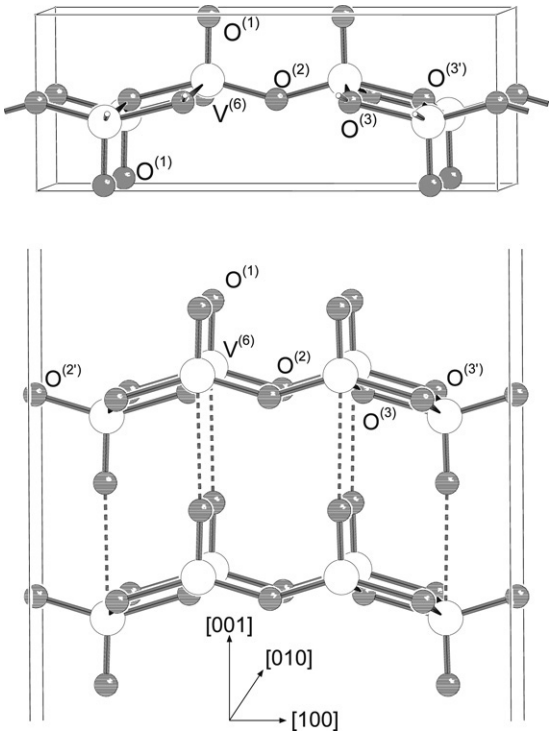

Fig. 17. V_2O_5 bulk structure and the bulk truncated (001) surface. Shown is a (1 × 1) 2L slab. The surface exposes five inequivalent oxygen atoms indicated as $O^{(1)}$, $O^{(2)}$, $O^{(2')}$, $O^{(3)}$, and $O^{(3')}$. Broken lines indicate the weak bonding between layers.

atoms were removed, the presence of V^{IV} species indicates that the two electrons left in the system upon $O^{(1)}$ removal did *not* remain together at the V atom to which the remove oxygen was initially bonded. Further oxygen loss could be induced by Ar^+ ion bombardment, as was indicated by the increased intensity from the defect induced peak in the gap which was accompanied by a shift of the V 2p levels towards lower binding energies. This shift suggests the presence of V species with oxidation states lower than IV.

Recent XPS and UPS experiments on thin V_2O_5 films have shown the presence of oxygen defects after annealing in UHV [221]. At ∼300 °C a prevailing V^{IV} valence state was observed. With increasing temperature V^{III} species were gradually created. The corresponding valence band spectra were similar to those of reduced surfaces by bombardment, i.e., a feature appeared in the bulk band gap at ∼1.3 eV below the Fermi energy.

The experimental characterization of the reduced V_2O_5(001) surface structure has been possible with modern surface science techniques such as STM. Images of the V_2O_5(001) surface cleaved in ultra-high vacuum (UHV) and at room temperature were recorded and inhomogeneities in the surface observed [227,228]. The vanadyl O is easily removed from the surface as a result of the cleavage and vacancies are left behind in a *non*-random distribution. Blum et al. [227] have recently observed thermally induced surface reconstructions of the V_2O_5(001) surface; using *in situ* band gap mapping derived from scanning tunneling spectroscopy data, they have observed a metal–insulator transition at 350–400 K, which occurs

inhomegeneously across the surface and expands preferentially in the direction of the vanadyl rows.

5.3. Reduced V_2O_5(001) surface

Theoretical studies on oxygen deficient V_2O_5 systems have been entirely devoted to the V_2O_5(001) surface [36–38,40–42]. One calculation was performed using both the hybrid B3LYP and the PBE functionals and cluster models [40], whereas most of the rest of the studies employed either cluster or periodic models with gradient-corrected functionals [37,38,41,42].

5.3.1. Structure relaxation and electronic structure

Lambrecht et al. [36] performed the first theoretical study of the electronic structure of surface vanadyl oxygen vacancies using a periodic single-layer tight-binding model of the surface with frozen geometry and argued that relaxations which introduce new types of interlayer coupling are *not* to be expected. They considered one defect in the (1 × 1) unit cell ($\Theta_{def} = 1/2$). This structure has alternate rows along the [010] direction with and without vanadyl oxygen atoms with a (1 × 1) periodicity. They found new occupied states within the gap, however *not* separated from the bottom of the conduction band. It is likely that the calculations were non-spin-polarized.

Hermann et al. [37,38] modelled isolated oxygen defects at the V_2O_5(001) surface using a $V_{10}O_{31}H_{12}$ cluster accounting for *one* crystal layer (1L cluster), and the (spin-polarized) LDA as well as the revised Perdew–Burke–Ernzerhof gradient-corrected functional (RPBE) [57], the latter with LDA geometries. The RPBE functional differs from the PBE functional only in the choice of the mathematical form for the exchange energy enhancement factor. Oxygen defects were created by removing one-, two-, or threefold coordinated surface oxygen atoms. The structures of the reduced clusters were fully optimized (using LDA only), except for the terminal hydrogen atoms. (Note that in Refs. [37] and [38], the *b*- and *c*-axis of the bulk unit cell are interchanged compared to the convention followed here: *b* and *c* parallel to the [010] and [001] directions, respectively.)

Hermann et al. [37,38] found a triplet ground state for all oxygen defect types (see also Ref. [39]), with the excess electrons occupying V 3d states at the bottom of the conduction band and *spreading* over the close V neighbors to the defect. This result was obtained using both LDA and RPBE functionals. The augmentation of the basis set with oxygen functions localized at the vacant sites on the clusters electronic structure did not yield lower lying occupied states in the gap [38].

Besides the 1L cluster, Hermann et al. [37,38] considered a $(V_{10}O_{31}H_{12})_2$ cluster accounting for two crystal layers and reported the changes in the relaxation patterns. On defect creation lattice relaxations were particularly large for the terminal oxygen atoms. In the 1L cluster model, the vanadium atom from which the oxygen atom was moved ∼0.5 Å downwards, while in the larger 2L cluster model, this atom shifted downwards by 0.94 Å and the vanadyl oxygen beneath moved upwards by 0.12 Å. As a result, a V–O–V bond between the layers was formed, cf. Fig. 18(a). Thus, proper description of this bond formation requires surface models that consist of at least two crystal layers. It is therefore somewhat surprising that calculations using 1L cluster models of $O^{(1)}$ defects are still being published [42].

Recent cluster (PBE and B3LYP) and periodic (PW91) studies have confirmed the large relaxations induced by the creation of a single vanadyl defect at the V_2O_5(001) surface and the V–O–V bond formation, and have discussed the associated changes in the electronic structure [40,41]. Ganduglia-Pirovano and Sauer [41] performed periodic spin-polarized calculations using a 2L slab (see Fig. 17). All atoms were allowed to relax. They considered vanadyl defect concentrations in the range $1/6 \leq \Theta_{def} \leq 1$ using (1 × 3), (1 × 2), and (1 × 1) unit cells. Additionally they considered two- and threefold coordinated defects at $\Theta_{def} = 1/4$ with (1 × 2) periodicity.

Fig. 18(a) shows the above-mentioned noticeable structure changes in the immediate vicinity of the $O^{(1)}$ surface defect site, V_{def}, i.e., the inversion of the VO_5 pyramid and the considerable local contraction of the interlayer spacing followed by the formation of a bond between the layers. The resulting V–O interlayer bond distances were 1.78 and 1.77 Å. Also, all V_{def}–O and V_b–O bonds within the crystal layers were shorter by up to ∼0.1 Å compared to the defect-free V_2O_5(001) surface.

Ganduglia-Pirovano and Sauer [41] reported the highest spin state for all vanadyl concentrations $1/6 \leq \Theta_{def} \leq 1$ and defect structures considered. For the other structurally different surface oxygen defects at $\Theta_{def} = 1/4$, the ground state was triplet, in agreement with the calculations of Hermann et al. [37,38] (cf. Table 7).

Fig. 19 shows the PW91 spin-projected total density of states of the isolated vanadyl defect (1 × 3) unrelaxed and relaxed structures at $\Theta_{def} = 1/6$. The difference DOS between up and down spin projections for the relaxed geometry upon O-removal is also shown. Virtually no contribution to the difference DOS from states within the valence band can be observed. For both geometries, the peak right at the Fermi level result from the partial occupation of the 3d orbitals on reduced V cations.

Fig. 20 shows the corresponding spin density distribution for the unrelaxed and relaxed structures. Without structure relaxation the two excess electrons localized primarily at the V_{def} site, whereas the interlayer bond formation results in a partial delocalization of the electrons over nearby metal sites. Note that the effect extends somewhat beyond the defect site and its counterpart at the second crystal layer.

At this point, this PW91 result for reduced vanadia systems, with a calculated band gap of 2.0 eV [41] (exp.: 2.3 eV), namely, the occupation of V 3d states at the bottom of the conduction band that are *not* actually split off, and a too *delocalized* electronic structure, should be expected. Indeed, Sauer and Döbler [40] have recently confirmed the spread of the spin density over adjacent V sites in a (010) plane containing the defect (see Fig. 21) using the PBE functional and the $(V_{10}O_{31}H_{12})_2$ cluster model of Refs. [37] and [38]. The structures of the clean and reduced clusters were fully

Table 7

Oxygen defect formation energies, $E_f^{\frac{1}{2}O_2}$ (in eV/atom), at the $V_2O_5(001)$ surface and associated changes in the electronic structure (see Sections 5.3.1 and 5.3.2)

Method[a]	Core-electrons	Basis set	Model	Cell, Θ_{def}	Defect	Spin state	Electronic structure[b]	$E_d^{\frac{1}{2}O_2}$[c]	$E_f^{\frac{1}{2}O_2}$	References
RPBE[d]	All-electron	DZVP[e]	$V_{10}O_{31}H_{12}$, $(V_{10}O_{31}H_{12})_2$	Isolated	$O^{(1)}$	Triplet	All types: HOMO level near the bottom of the conduction band; excess electrons spread over adjacent V sites	2.83	3.64[f], 2.65[f]	Hermann et al. [38] and Druzinić [39]
			1L, 2L		$O^{(2)}$[g]	Triplet			4.36[f], 3.87[f]	
					$O^{(3)}$[g]	Triplet			3.66[f], 3.26[f]	
PW91	PAW	800 eV	2L	$p(1\times3)1/6$	$O^{(1)}$	Triplet	Occupied states at the bottom of the conduction band; excess electrons spread (after relaxation) over adjacent V sites in a (010) plane containing the defect	3.13	1.93	Ganduglia-Pirovano and Sauer [41]
				$p(1\times3)1/3$	$O^{(1)}$ [100] pairs	High spin	Not discussed		1.97	
				$p(1\times2)1/3$	$O^{(1)}$ [010] pairs	High spin			1.90	
				$p(1\times2)1/2$	$O^{(1)}$ [010] rows	High spin			1.87	
				$p(1\times2)3/4$	$O^{(1)}$	High spin			1.99	
				$p(1\times1)1/1$	$O^{(1)}$	High spin			2.07	
				$p(1\times2)1/4$	$O^{(1)}$	Triplet			1.95	
					$O^{(2)}$[g]	Triplet			3.65	
					$O^{(3)}$[g]	Triplet			3.97	
PBE	All-electron	TZVP[e]	$(V_{10}O_{31}H_{12})_2$	Isolated	$O^{(1)}$	Triplet	Excess electrons spread over adjacent V sites in a (010) plane containing the defect	3.08	1.83	Sauer and Döbler [40]
B3LYP	All-electron	TZVP[e]	$(V_{10}O_{31}H_{12})_2$	Isolated	$O^{(1)}$	Triplet	Excess electrons strictly localized at the V sites involved in the interlayer V–O–V bonding	2.60	1.17	Sauer and Döbler [40]

The effect of lattice relaxations is included.

[a] Spin-polarized (unrestricted Kohn–Sham) calculations.

[b] In *all* studies electrons left in the system occupied V 3d states.

[c] O_2 molecule dissociation energy (in eV/atom).

[d] Revised Perdew–Burke–Ernzerhof gradient-corrected functional [57].

[e] For all atoms (V, O, and H).

[f] $E_f^O = 6.47/5.48$ ($O^{(1)}$), 7.19/6.70 ($O^{(2)}$), and 6.49/6.09 ($O^{(3)}$) eV (1L/2L cluster) were reported; $E_d^{\frac{1}{2}O_2} = 2.83$ eV [229] (RPBE) was used to convert E_f^O into $E_f^{\frac{1}{2}O_2}$ (cf. Eqs. (1) and (2)).

[g] The values for the $O^{(2)}$ and $O^{(3)}$ vacancies correspond to the average between the formation energies of the two inequivalent $O^{(2)}$ and $O^{(3)}$ defects, respectively.

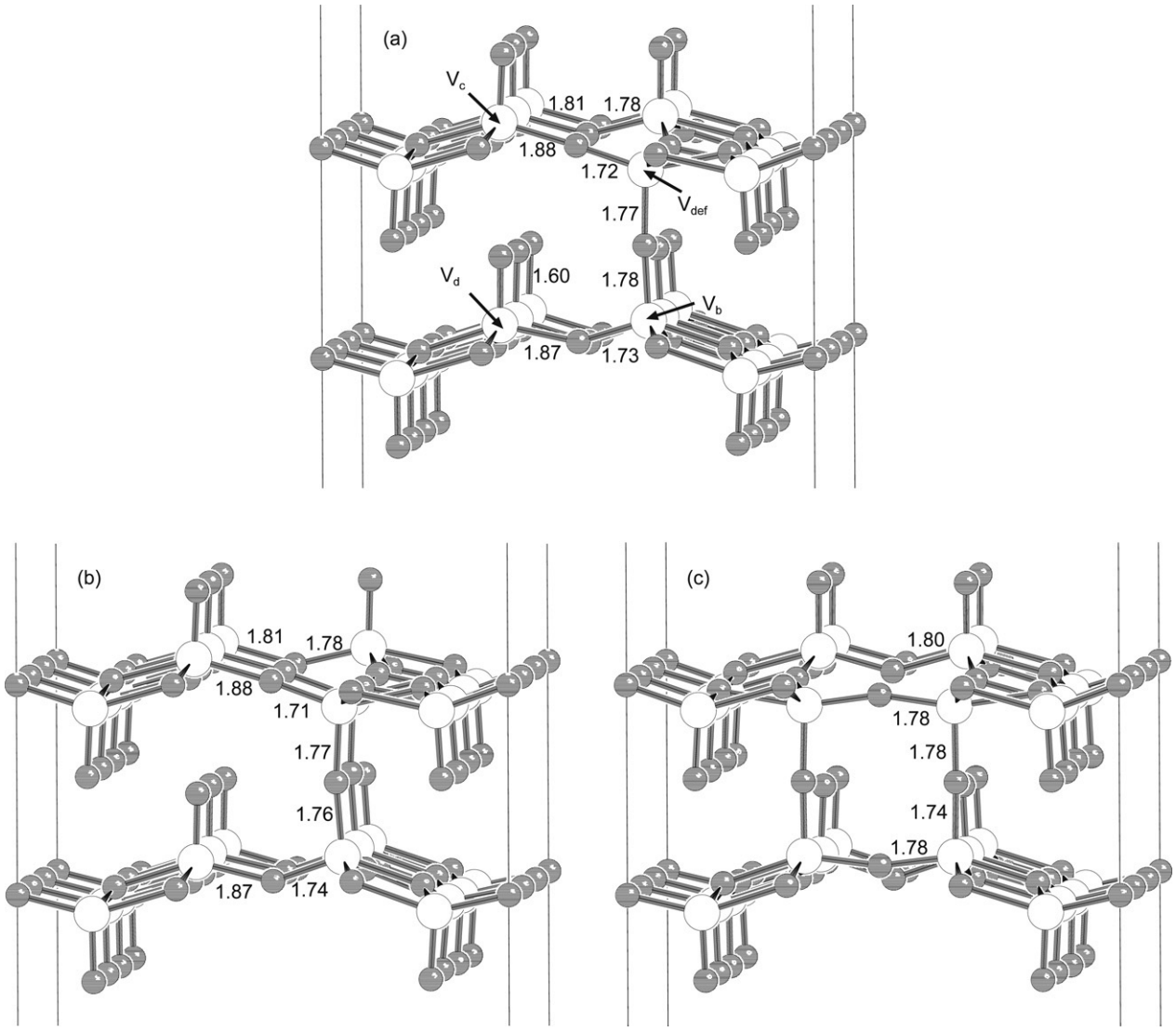

Fig. 18. Atomic geometry of (1×3) vanadyl oxygen defect structures from PW91 calculations, (a) $\Theta_{\mathrm{def}} = 1/6$, (b) and (c) $\Theta_{\mathrm{def}} = 1/3$ with defect pairs along the [010] and [100] directions, respectively. V atoms are depicted as white circles and O atoms as the smaller black circles. Selected bondlengths in Å. Adapted from Ganduglia-Pirovano and Sauer [41].

optimized (with constraints in selected dihedral angles that involved terminating hydroxyl groups).

The agreement between the cluster PBE and periodic PW91 results for the spin density together with that of the corresponding defect formation energies (see next section) indicates the adequacy of the cluster model used in Ref. [40]. Differently from these GGA results, the hybrid functional B3LYP applied to the two-layer cluster model, yielded *localized* electrons at the two V sites participating in the interlayer V–O–V bond only (see Fig. 21 and Table 7). On the one hand, these results show the importance of both exact exchange and lattice relaxations for the proper description of the localized electrons following vanadyl oxygen removal at the $V_2O_5(001)$ surface; on the other hand, they render the results of 1L cluster studies questionable. It is clear that the atomic displacements following the vanadyl defect formation play an essential role in the resulting electronic structure; the V defect site is not reduced to V^{III} but V^{IV}. Schematically,

$$
\begin{array}{ccccc}
\mathrm{O} & & & & \\
\| & & & & \\
\mathrm{V^{V}} & & \mathrm{V^{III}} & & \mathrm{V^{IV}} \\
\vdots & \xrightarrow{-\mathrm{O}} & \vdots & \xrightarrow{\text{relax}} & | \\
\mathrm{O} & & \mathrm{O} & & \mathrm{O} \\
\| & & \| & & | \\
\mathrm{V^{V}} & & \mathrm{V^{V}} & & \mathrm{V^{IV}}
\end{array}
$$

As mentioned above, XPS work by Zhang and Henrich [219] and Wu et al. [221] pointed out the existence of V^{IV} centers at V_2O_5 surfaces upon initial reduction induced by ion bombardment or annealing (cf. Section 5.2). Thus presupposing here the easiest V–O bond dissociation of surface vanadyl oxygen atoms (see next section), the results of Refs. [41] and [40] indicate that lattice relaxation plays a decisive role in creating V^{IV} sites. Both the gradient-corrected (PW91/PBE) and hybrid (B3LYP) functionals yielded the V–O–V bond between the layers, however, differences in the calculated

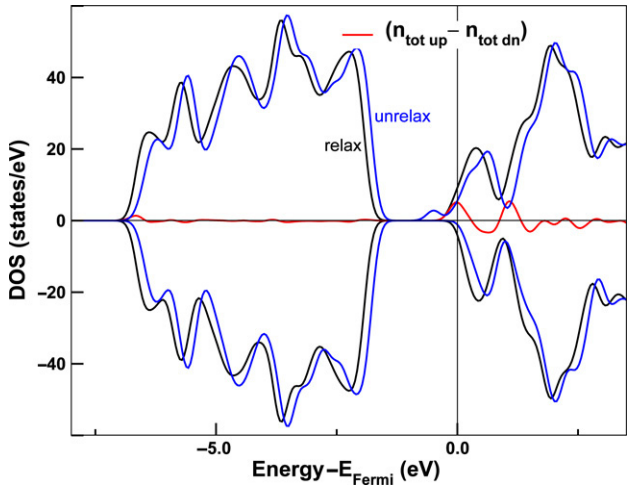

Fig. 19. Total spin-projected DOS from PW91 calculations (α-spin: $n_{\text{tot up}}$, β-spin: $-n_{\text{tot dn}}$,) of the fully relaxed (black lines) and unrelaxed (blue lines) defect structure at $\Theta_{\text{def}} = 1/6$. The red line correspond to the difference between α- and β-spin states of the relaxed structure. The curves are smoothed by a gaussian level broadening of 0.2 eV. Figure adapted with permission from Ganduglia-Pirovano and Sauer [41].

geometries were obtained. These are to be expected. For example, the V–O interlayer bond distances were 1.80/1.86 and 1.73/1.69 Å with (cluster) PBE/B3LYP (cf. 1.78 and 1.77 Å for periodic PW91, as reported above).

Furthermore, Ganduglia-Pirovano and Sauer [41] found that the additional lattice relaxations occurring when subsequent vanadyl defects are created (forming firstly pairs) along either the [010] or [100] directions, are distinct. Fig. 18(b) and (c) display the fully relaxed structures at $\Theta = 1/3$ induced by defect pairs along the [010] and [100] directions, respectively. For the former the atomic displacements around each vacancy were very similar to those for an isolated defect at $\Theta_{\text{def}} = 1/6$ (cf. Fig. 18(a)). That implies that the subsequent vacancy induced only very small additional changes in the local structure of the already existing defect. Thus, a *non*-counteracting defect induced relaxation effect with increasing coverage (from 1/6 to 1/3) was found when defects aligned along the [010] direction. Similar considerations applied when the concentration is further increased from 1/3 to 1/2 and a trench-like structure with a (1×1) periodicity and vacancy rows along the [010] direction form. In contrast, the lattice relaxations induced by subsequent vacancies that form [100] oriented pairs, were found to somewhat counteract those occurring after the first defect was created (cf. Fig. 18(a) and (c)). The reason for mentioning this will become apparent in the next section when discussing the effect of increasing the defect concentration on the formation energy of surface $O^{(1)}$ defects.

5.3.2. *The V_2O_5(001) surface defect formation energy*

Table 7 summarizes the calculated oxygen defect formation energies at the V_2O_5(001) surface. Hermann et al. [38] and Druzinić [39] computed RPBE E_f^{O} values of 6.47/5.48, 7.19/6.70, and 6.49/6.09 for the $O^{(1)}$, $O^{(2)}$, and $O^{(3)}$ defects, respectively, using the 1L/2L cluster model (for the LDA geometries). The numbers for the $O^{(2)}$ and $O^{(3)}$ vacancies correspond to the average between the formation energies of the two inequivalent $O^{(2)}$ and $O^{(3)}$ defects, respectively (cf. Fig. 17). In Table 7 these E_f^{O} values have been converted into $E_f^{\frac{1}{2}\text{O}_2}$ using the RPBE dissociation energy of the O_2 molecule $\frac{1}{2}E_d^{\frac{1}{2}\text{O}_2} = 2.83$ eV [229] (cf. Eqs. (1) and (2)). Thus, according to the 2L cluster (RPBE) results, the 1L cluster values in Ref. [38] are overestimated (by about 1, 0.5, and 0.4 eV for the $O^{(1)}$, $O^{(2)}$, and $O^{(3)}$ defects, respectively) because of the limited account for structure relaxations in the small model. The difference between the $E_f^{\frac{1}{2}\text{O}_2}$ values obtained using the 1L and 2L models is particularly large for the $O^{(1)}$ defect which leads to bond formation between the defective surface layer and the crystal layer beneath. The ease of removal of the terminal vanadyl oxygen atoms may be inferred, considering the 2L cluster (RPBE) values.

Ganduglia-Pirovano and Sauer [41] have recently reported that the formation energy of an isolated $O^{(1)}$ defect is smaller than that of $O^{(2)}$ and $O^{(3)}$ defects by about a factor of two with $E_f^{\frac{1}{2}\text{O}_2} = 1.95$, 3.65, and 3.97 eV for the $O^{(1)}$, $O^{(2)}$, and $O^{(3)}$, respectively. These numbers resulted from PW91 periodic 2L slab calculations for each inequivalent surface oxygen site at $\Theta_{\text{def}} = 1/4$; the formation energy of $O^{(2)}$ and $O^{(3)}$ defects correspond to average values. At $\Theta_{\text{def}} = 1/4$, the significant relaxations upon vanadyl oxygen removal contributed to a reduction of the energy from 3.78 to 1.95 eV. An additional 20 meV decrease is gained if the defect separation along the [010] direction is increased from $2 \cdot b$ to $3 \cdot b$ (i.e., a defect concentration decrease from 1/4 to 1/6, cf. Table 7). Thus, the value of 1.93 eV represents the isolated $O^{(1)}$ defect *limit* at the PW91 level. (Note that the extention of the V_2O_5(001) slab from 2L to 3L yielded deviations of ~3 meV.)

The RPBE functional is known to yield improved energies (i.e., to reduce the PBE or PW91 characteristic overbinding) [57]. The RPBE and PW91 O_2 dissociation energy ($E_d^{\frac{1}{2}\text{O}_2}$) used in the evaluation of the defect formation energies of Refs. [39] and [41] (2.83 and 3.13 eV/atom, respectively) are by 0.24 and 0.54 eV larger than the experimental value (2.59 eV/atom). However, the (2L cluster) RPBE defect formation energies ($E_f^{\frac{1}{2}\text{O}_2}$) are *not* lower than the (2L slab) PW91 values for all defect types (cf. Table 7). In particular, for the $O^{(1)}$ defect the RPBE formation energy is about 0.7 eV larger than the (periodic) PW91 limit (cf. 2.65 and 1.93 eV).

Sauer and Döbler [40] calculated the vanadyl defect formation energy using the 2L cluster with PBE for the corresponding geometry. Their PBE $E_f^{\frac{1}{2}\text{O}_2}$ value of 1.83 eV (cf. Table 7) with a relaxation energy contribution of 1.90 eV was in very good agreement with the (periodic) PW91 value of 1.93 eV (1.83 eV contribution from relaxation) for $\Theta_{\text{def}} = 1/6$. As already mentioned, the PBE and PW91 functionals are constructed so as to yield essentially the same results for structure and bond dissociation energies. Hence, this agreement

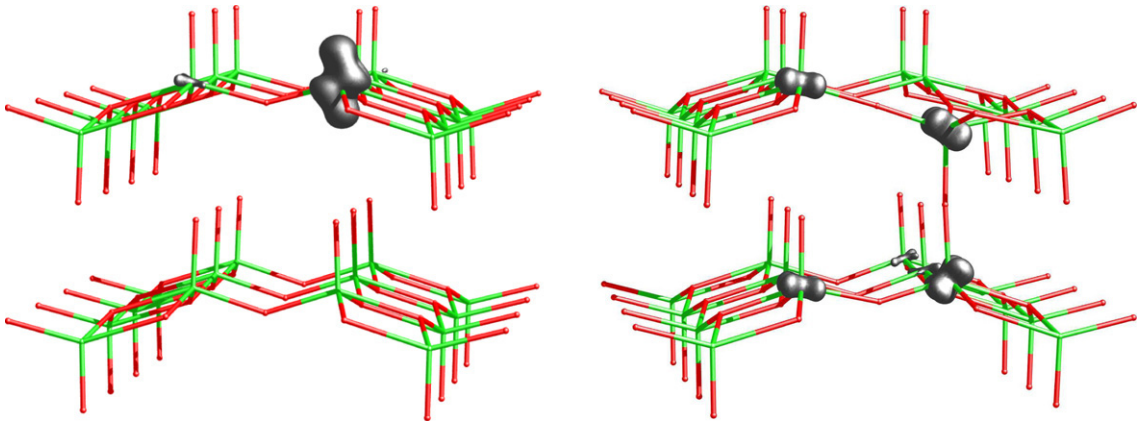

Fig. 20. Spin density distribution upon creation of a single vanadyl oxygen defect at the $V_2O_5(001)$ surface ($\Theta_{def} = 1/6$), with unrelaxed (left) and relaxed (right) geometries as obtained with PW91.

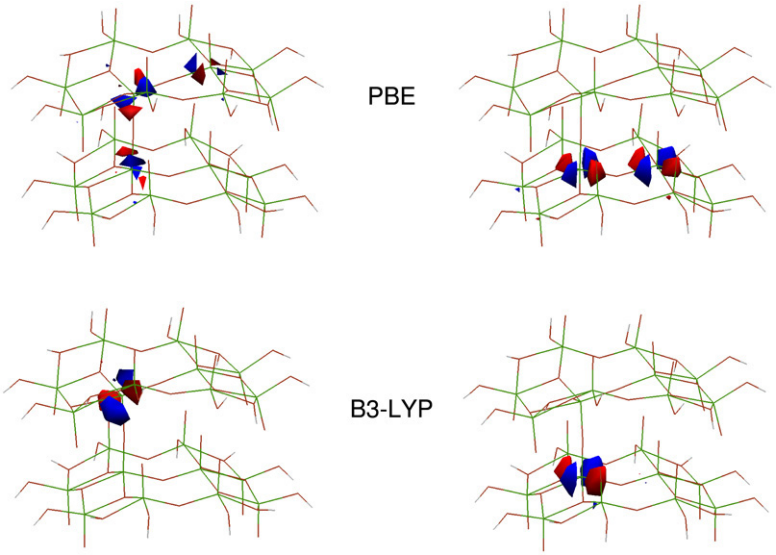

Fig. 21. The two singly occupied natural orbitals by the (two) excess-electrons for the oxygen deficient $V_2O_5(001)$ cluster model $(V_{10}O_{31}H_{12})_2$. Top left and right correspond to PBE results and bottom left and right to B3LYP results. Figure reproduced with permission from the The Royal Society of Chemistry [40].

is a clear indication of the adequacy of the cluster approach in Ref. [40] and raises some questions about quality of the 2L cluster RPBE results in Refs. [38] and [39]. To fully understand the origin of the RPBE overbinding, which may be due in part to the quality of the basis set, would require a very systematic testing.

When more than just isolated defects are created, the separation between them decreases and defects may interact. Ganduglia-Pirovano and Sauer [41] calculated the average defect formation energy of eight different structures at varying defect concentration with $1/3 \leq \Theta_{def} \leq 1$ (PW91 functional). Increasing the defect concentration from 1/4 to 1/3 led to an increase in the formation energy by ~20 meV (from 1.95 to 1.97 eV) when [100] oriented pairs formed, whereas a *decrease* by 50 and 80 meV was found when defect pairs ($\Theta_{def} = 1/3$) and rows ($\Theta_{def} = 1/2$) formed along the [010] direction, respectively (cf. Table 7). The lowest defect formation energy was found for the trenchlike structure with missing rows along the [010] direction at $\Theta_{def} = 1/2$.

The preference for the [010] alignment over other defect structures as the defect concentration increases from 1/6 to 1/3 and up to 1/2, was explained using the relaxation effects described in the previous section [41]. Specifically, the defects share the energy of inverting the VO_5 pyramids when subsequent defects are created along the [010] direction, and the formation energy of each additional defect decreases from 1.93 ($\Theta_{def} = 1/6$) to 1.87 ($\Theta_{def} = 1/3$) to 1.83 eV ($\Theta_{def} = 1/2$). In contrast, starting from an isolated defect site, the formation energy of an additional defect forming a [100] oriented pair increases by 0.27 eV due to counteracting lattice relaxation effects which render the reduction of the surface along this direction rather unlikely. Combining the DFT calculations with statistical thermodynamics, the stability of a missing-row structure under reducing conditions was predicted. This DFT (PW91) prediction appear to be consistent with STM observations of a non-random vanadyl oxygen defect distribution at the $V_2O_5(001)$ surface, which are created at room temperature under UHV [228]. Furthermore, it is

compatible with the recently observed [227] metal–insulator transition at 350–400 K (UHV), which expands preferentially in the [010] direction (cf. Section 5.2).

As mentioned above, the use of hybrid functionals is expected to yield improved defect formation energies. Using the 2L cluster model, Sauer and Döbler [40] calculated the vanadyl oxygen defect formation energy with the B3LYP functional for the correspondingly relaxed geometry. They obtained $E_f^{\frac{1}{2}O_2} = 1.17$ eV with a relaxation contribution of 1.79 eV (cf. Table 7). Thus, the use of exact-exchange resulted not only in the *complete* localization of the excess electrons upon vanadyl oxygen removal (cf. previous section) but also yielded a particularly small value for the corresponding defect formation energy that is consistent with the distinct sensitivity of the $V_2O_5(001)$ surface to any probing beam (cf. Section 5.2). The ∼0.7 eV difference between the $E_f^{\frac{1}{2}O_2}$ values obtained using the PBE and B3LYP functionals (cf. 1.83 and 1.17 eV), is related to the different description of the V=O and O–O binding at the oxide surface and in the O_2 molecule, respectively, with gradient-corrected and hybrid functionals (cf. Section 3.3.1).

The B3LYP prediction of about 1.2 eV is somewhat smaller than the experimental estimates from electrical conductivity measurements in molten V_2O_5 of 1.3–1.5 eV [230], whereas the GGA value of 1.9 is clearly larger. The better performance of B3LYP for V=O bond dissociation energies with respect to GGA functionals, is compatible with the corresponding results obtained for the $O{=}V{=}O^+$ cation [40]. B3LYP yielded results that deviate by less than 0.1 eV from a multi-reference ab initio calculation and were within the error bars from experiment, whereas GGA functionals gave overestimated values by more than 1 eV.

Here, it is important to mention that similar to the isolated $O^{(1)}$ defect formation energy, the PW91 values for higher defect concentrations are overestimated. However, we expect the general stability trend to be valid; corresponding (larger cluster or periodic) B3LYP studies would be desirable.

5.4. Summary V_2O_5

The study of the formation of (vanadyl) oxygen vacancies at the $V_2O_5(001)$ surface with DFT (cluster and periodic) methods using local, gradient-corrected, and hybrid functionals led to a number of interesting observations that are summarized next.

The relaxation pattern at the (001) surface of the layered V_2O_5 structure upon reduction is *particular*, i.e., without an analogue among the TM oxide surfaces discussed so far (TiO_2 and ZrO_2). Similar to $TiO_2(110)$, lattice rearrangements extend up to two (slab) layers. At the $V_2O_5(001)$ surface, however, the atom displacements can be significantly larger, up to ∼1 Å.

The terminal vanadyl defects are a special case among the different types of surface oxygen atoms; they are the easiest to form. Vanadyl defect formation at the $V_2O_5(001)$ surface leads to V–O–V bond formation between the two outermost crystal layers. Both gradient-corrected (periodic and cluster) and hybrid functionals (cluster) describe this lattice rearrangement reasonably well provided that the model includes *two* crystal layers.

The vanadyl defect induced structure relaxation plays an essential role in the resulting electronic structure and in reducing the energy to create such defects. Without relaxation a V^{III} site would form on oxygen removal, whereas the formation of a V–O–V interlayer bond leads to the creation of two V^{IV} sites instead.

With GGA functionals, independent of the surface model, the electrons left in the system upon vanadyl defect formation, spread over adjacent V sites in a (010) plane containing the defect, and occupy V 3d states at the bottom of the conduction band. These states are *not* split from the conduction band at variance with what has been observed. The use of hybrid functionals led to the complete localization of the excess electrons on the V atoms forming the interlayer bond. The resulting electronic ground state is triplet; that of higher vanadyl defect concentrations as well as that of all other types of isolated defects is (also) high spin.

There is a clear agreement on the results of the cluster and periodic gradient-corrected studies (PBE/PW91) of (isolated) vanadyl oxygen defects at the $V_2O_5(001)$ surface, namely, on the *limitations* of GGA functionals. The use of a hybrid approach (B3LYP) utilizing the (validated) cluster model yields not only an improved description of the electronic structure of reduced V_2O_5 but a quantitative difference in the oxygen defect formation energy, namely, a ∼0.7 eV lowering of the (isolated) vanadyl defect formation energy. Hence, the hybrid functional represents an important tool to interpret and complement the experimental information on reduced $V_2O_5(001)$, and considerably enhances the predictive power of DFT with GGA functionals. Yet, we recognize the merit of PW91 in *predicting* the alignment of vanadyl defects along the [010] direction and the formation of a missing-row structure at $\Theta_{def} = 1/2$. Line defects are favored by the sharing of the energy needed to deform the structure.

6. Cerium oxide

6.1. CeO_2 applications and basic information

The major application of the RE oxide ceria (CeO_2) is in catalysis [3]. Its main use is connected with the reduction of noxious components from automotive exhaust gases. The cleaning system comprises a three-way catalyst which uses a ceramic or metallic substrate with an active coating incorporating alumina, ceria, and other oxides and combinations of metals such as platinum, palladium, and rhodium. The importance of ceria in catalysis originates from its remarkable oxygen storage capability, i.e., its ability to undergo rapid and repeatable redox cycles depending on the conditions in the reactor stream. This feature is strongly related to the facile creation, healing, and diffusion of oxygen vacancies, especially at the ceria surfaces. In addition, ceria has potential uses in fuel cell technology [231–235].

CeO_2 exists in the cubic fluorite structure (CaF_2), i.e., the same structure as c-ZrO_2 ($a_{exp} = 5.41$ Å) [236,237]. It consists

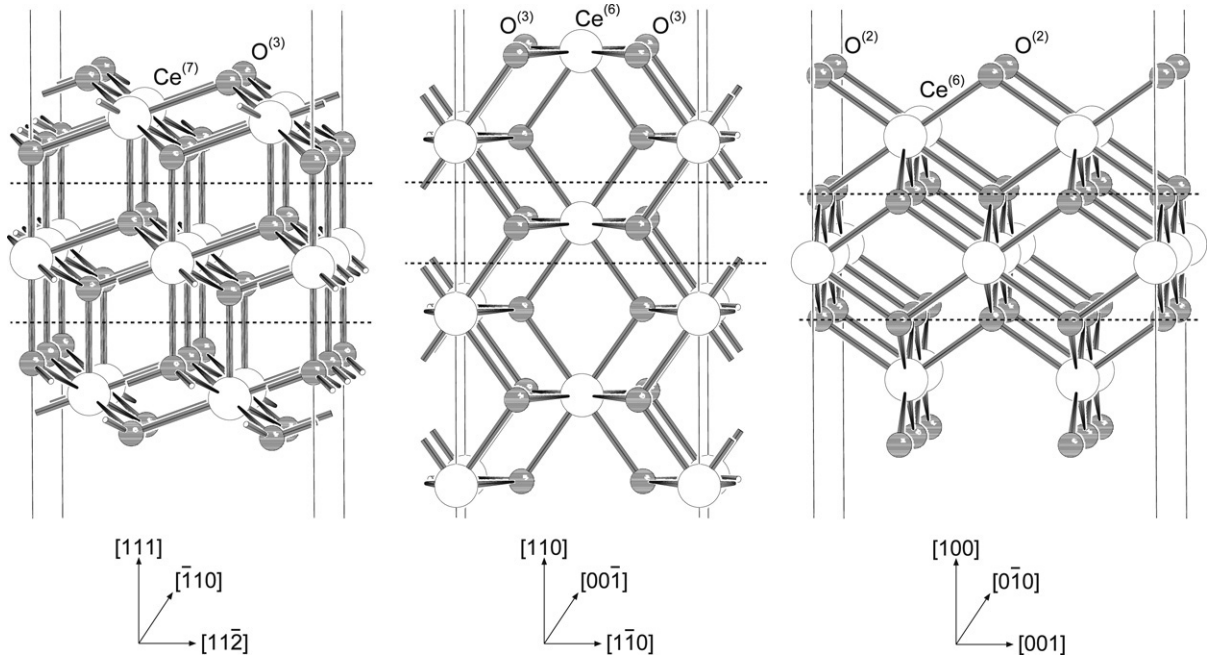

Fig. 22. Bulk truncated CeO_2(111), (110), and (100) surfaces. Shown are the ($\sqrt{3} \times 2$) 3L, (1 × 1) 6L, and (2 × 2) 3L slabs, respectively. The dotted lines indicate the repeating unit (1L) in the direction perpendicular to the surface. Small and large circles represent the oxygen and cerium atoms, respectively.

of a cubic array of fourfold coordinated oxygen ions, with the metal ions occupying half of the eightfold coordinated cationic interstices. The relative stability of the low-index ceria surfaces decreases in the (111) > (110) > (100) order [51,238,239]. The non-polar CeO_2(111) surface is observed to undergo little relaxation [240,241].

It is terminated by threefold coordinated oxygen atoms, $O^{(3)}$, and exhibits sevenfold coordinated cerium atoms, $Ce^{(7)}$ (see Fig. 22) [242–245]. The (110) and (100) surfaces undergo significant surface relaxations [246–248]. The (110) surface is terminated by a CeO_2 plane with threefold oxygen and sixfold coordinated cerium atoms, $Ce^{(6)}$, whereas the (100) surface is terminated by twofold coordinated oxygen atoms, $O^{(2)}$.

CeO_2 is an insulator. The experimental band gap is 6.0 eV between the O 2p and Ce 5d states [249–252]. The nature of the electronic ground state was controversial. One scenario featured a formally fully occupied O 2p band and *empty* 4f states (Ce $4f^0$) *in* the band gap [250,253–257], and the other involved a mixture of Ce $4f^0$ and Ce $4f^1$O2p-hole states [258–260]. The intermediate valence of the latter was deduced mostly from core-level XPS [258,259,261]. The analysis of the CeO_2 XPS spectra is not straightforward and one cannot easily conclude from the final state photoemission spectra on the intermediate valence of the initial state. In general, the experimentally obtained 4f occupancy does not distinguish localized from extended f-symmetry states in the initial state [262]. There is agreement with the facts that the valence band contains a non-negligible admixture of f-symmetry, and that the occupancy of strictly localized 4f states (if any) is very small [250,262]. On the basis of optical reflectivity measurements, a possible partial occupation of the $4f^1$ states of less than 5% could not be excluded [256]. These states are located about 1.5 eV *above* the Fermi level with a measured full width at half maximum of 1.2 eV [250]. When CeO_2 is exposed to reducing conditions (i.e., low O_2 pressure and high temperature), the existence of these unoccupied f-states close to the Fermi level results in the change of the nature of the electronic states associated with the f-electrons as discussed in the next section.

6.2. Experimental findings on oxygen vacancies

Like in ZrO_2, it is possible to accommodate a large number of mobile oxygen vacancies in ceria by doping with aliovalent cations [263–265], but also by oxygen removal. Oxygen can either be removed from the bulk by annealing [266] with subsequent diffusion to the surface, or directly from the surface by annealing, sputtering [252,267–269], electron irradiation [250], exposure to X-rays [270], or chemical reduction [271, 272].

In oxides, cerium has two oxidation states, Ce^{III} and Ce^{IV}. In fact, removal of oxygen from ceria, when exposed to an O_2 deficient atmosphere at high temperatures, leads to the formation of several cerium oxide phases of the type CeO_{2-x} with a range of possible compositions ($0 \leq x \leq 0.5$) [273–275].

A great deal of experimental work was devoted to the determination of the oxidation state of Ce at reduced CeO_2 surfaces. Using several techniques, such as X-ray and ultraviolet photoelectron spectroscopy (UPS) and high-resolution energy loss spectroscopy [243,252,268,269,276–278], UV–Vis diffuse reflectance, and infrared spectroscopy [271], and EPR [279], indications for the presence of Ce^{III} at the surface and in deeper layers were found. In particular, an additional emission at a binding energy of 1.2–1.5 eV above the top of the O 2p band *in* the band gap is observed in the UPS spectra of reduced surfaces [243,252,268,269,278].

The additional peak is assigned to emission from *localized* Ce 4f orbitals. Thus, the excess electrons left behind upon oxygen removal occupy strongly localized f states driving the $Ce^{IV} \rightarrow Ce^{III}$ reduction. We note here and discuss below that any proper theoretical description of reduced ceria systems needs to be able to treat both, the Ce^{IV} 4f electrons participating to the bonding and the tightly bound Ce^{III} 4f electrons. This requirement challenges computational approaches *more* than the proper description of reduced 3d (TiO_2, V_2O_5) or 4d (ZrO_2) TM oxides discussed so far.

Using STM and noncontact atomic force microscopy the structure of reduced surfaces was imaged [240,244,245,247, 267,280]. Oxygen defects created by annealing the (111) surface were found to be either isolated or aggregated in extended clusters [240,244,245,267,280]. For the slightly reduced surface, defect clusters were not dominant and both surface and subsurface defects were present at similar concentrations. Upon prolonged annealing, linear (surface) defect clusters became dominant with triangular clusters being next most abundant. Esch et al. [280] have recently reported that actually subsurface defects are required to nucleate linear surface clusters that expose exclusively reduced Ce^{III} ions.

6.3. Reduced low-index CeO_2 surfaces

Theoretical studies on reduced ceria surfaces used classical interatomic potentials [43,44], periodic DFT with the local density and gradient-corrected functionals, and the DFT + U approach [46,50–52,280]. Embedded-cluster calculations [90] with explicit treatment of the electron correlations by Møller–Plesset perturbation theory (MP2) were also employed. In contrast to the transition (d) metal oxides discussed so far, no (periodic or cluster) study of partially reduced CeO_2 systems (surfaces and bulk) using hybrid approaches has been reported yet.

6.3.1. Structure relaxation and electronic structure

Earlier studies of reduced ceria surfaces using force-fields [43,44] assumed the existence of two Ce^{III} ions per neutral oxygen defect, and the more recent calculations using gradient-corrected functionals badly *fail* to describe the excess electrons localization upon reduction as discussed below [46,50,51].

Yang et al. [46] considered the reduction of the (111) and (110) CeO_2 surfaces (see Fig. 22) and employed the (spin-polarized) PW91 functional [157]. The surfaces were modelled as periodically repeated (in z-direction) slabs. The (111) oriented surface contained four O–Ce–O repeating units (or slab layers), while the (110) surface consisted of five identical planes with CeO_2 stoichiometry. Lattice relaxations upon reduction were taken into account with the bottom 2L of both slabs fixed at their bulk positions. Defects were considered at the surface and in the subsurface oxygen atomic layers at two concentrations. Specifically, orthorhombic $p(\sqrt{3} \times 1)$ [$\Theta_{def} = 1/2$] and $p(\sqrt{3} \times 2)$ [$\Theta_{def} = 1/4$] unit cells were used for the (111) orientation, while $p(1 \times 2)$ [$\Theta_{def} = 1/4$] and $p(2 \times 2)$ [$\Theta_{def} = 1/8$] cells were used for the (110) surface. In this ($a' \times b'$) nomenclature of the (reduced) surface unit cells the a'- and b'-axis are parallel to the bulk $[1\bar{1}2]$ and $[\bar{1}10]$ directions for the (111) orientation, and to the $[1\bar{1}0]$ and $[00\bar{1}]$ directions for the (110). Within this choice the $p(\sqrt{3} \times 1)$ (111) and $p(1 \times 2)$ (110) surface unit cell has dimensions of $\frac{1}{2}\sqrt{6}a \times \frac{1}{2}\sqrt{2}a$ and $a \times \sqrt{2}a$ (with a the bulk lattice parameter), respectively.

Yang et al. [46] reported that the structural modifications induced by the surface defects at the differently oriented surfaces followed a quite general pattern, namely, Ce atoms nearest neighbors to the vacant site moved away from the defect while O atoms next-nearest neighbors contracted in the vacant region. Moreover, the resulting atomic structures provided some insight into the (inadequate) PW91 description of the electronic structure of the corresponding reduced surfaces. For example, for the (111) surface at $\Theta_{def} = 1/4$, the initially (by symmetry) equivalent *three* Ce atoms neighboring the defects remained equivalent upon reduction, i.e., *no* distorted structure formed around the vacant sites. Thus, in this final geometry, there *cannot* be just *two* neighboring Ce^{III} ions to the defects. Ce^{III} ions have a larger atomic radius than the Ce^{IV} and this should be reflected in different Ce–O bond lengths.

The detailed analysis of the electronic structure of the reduced systems for the example of the (111) $p(\sqrt{3} \times 1)$ and (110) $p(1 \times 2)$ structures, yielded *metallic* ground states with the excess electrons distributed rather evenly on the Ce atoms of the three outermost layers. An antiparallel magnetic order for the (111) $p(\sqrt{3} \times 1)$ structure and a parallel magnetic order for the (110) $p(1 \times 2)$ reduced surface were found (see Table 8).

The inadequacy of PW91 to provide a proper account of the Ce valency change upon reduction of surfaces of ceria as shown by Yang et al. [46], has been confirmed recently [50,51]. Fabris et al. [50] and Nolan et al. [51] investigated defective ceria surfaces using the PBE and PW91 functional, respectively, and both described *metallic* ground states and report on the failure of GGA functionals. The LDA approximation fails as well [50]. We note the importance of properly accounting for the overlap between core and valence densities in the description of the electronic structure of reduced ceria systems [49,281]; the inclusion of the nonlinear core corrections in the pseudopotentials has little effect on the structural properties, though. Fig. 23 shows an isosurface of spin-density for the example of the reduced $p(2 \times 1)$ (100) surface ($\Theta_{def} = 1/4$) of the work of Nolan et al. [51]. The ground state was triplet. The *complete* delocalization of the excess electrons is clearly seen. We observe that the extent of the excess charge delocalization is greater than that for the TM oxides discussed so far. The unphysical self-interaction introduced by gradient-corrected functionals can be substantial for the cases in which the orbital overlaps are small, the bands narrow, and the electrons nearly localize in atomic-like orbitals [60], resulting in the *complete* failure of the GGA approximations.

Both Nolan et al. [51,52] and Fabris et al. [50] further applied periodic spin-polarized DFT + U approaches which represent a very pragmatic way to overcome the limitations of GGA functionals (see Section 2). The former studied surface oxygen defects at the (111), (110), and (100) ceria surfaces using PW91 + U [157] with an empirically determined $U' = 5$ eV together with projectors based on standard Ce 4f atomic

Table 8

Oxygen defect formation energies, $E_f^{\frac{1}{2}O_2}$ (in eV/atom), at CeO_2 surfaces and associated changes in the electronic structure (see Section 6.3)

Surfaces	Method[a]	Core-electrons	Basis set	Model	Cell, Θ_{def}	Spin state	Electronic structure[b]	$E_d^{\frac{1}{2}O_2}$[c]	$E_f^{\frac{1}{2}O_2}$ surf/sub	References
(111)	PW91	PAW	400 eV	4L	$p(\sqrt{3}\times 1)1/2$	Singlet	Metallic antiferromagnetic ground state; fully delocalized excess electrons	3.02	3.98[d]/3.80[d]	Yang et al. [46]
					$p(\sqrt{3}\times 2)1/4$		Same as for $\Theta_{def}=1/2$		3.39[d]/3.21[d]	
(111)	PW91 + U ($U'=5.0$)	PAW	500 eV	4L	$p(2\times 2)1/4$	Triplet	Insulating ferromagnetic ground state; occupied f state at 1.1 eV above O 2p band	–	2.60/–	Nolan et al. [52]
(111)	PBE + U ($U'=4.5$)	US-PP	408 eV	3L/4L[e]	$p(2\times 2)1/4$	Singlet	Insulating antiferromagnetic ground state; defect state at 1.5 eV above O 2p band	–	4.95[f]/4.81[f] 2.15[g]/1.89[g]	Fabris et al. [50]
(111)	LDA + U ($U'=5.3$)						Same as PBE + U with occupied f state at 1.9 eV above O 2p band		6.10[f]/6.25[f] 2.92[g]/2.95[g]	
(110)	PW91	PAW	400 eV	5L	$p(1\times 2)1/4$	Triplet	Metallic ferromagnetic ground state; fully delocalized excess electrons	3.02	3.17[d]/3.66[d]	Yang et al. [46]
					$p(2\times 2)1/8$		Same as for $\Theta_{def}=1/4$		2.48[d]/3.39[d]	
(110)	PW91 + U ($U'=5.0$)	PAW	500 eV	7L	$p(1\times 2)1/4$	Triplet	Insulating ferromagnetic ground state; defect state at 1.0 eV above O 2p band	–	1.99/–	Nolan et al. [52]
(110)	PBE + U ($U'=4.5$)	US-PP	408 eV	6L	$p(2\times 2)1/8$	Triplet	Insulating ferromagnetic ground state; occupied f state at 1.4 eV above O 2p band	–	4.42[f]/– 1.57[g]/–	Fabris et al. [50]
(110)	LDA + U ($U'=5.3$)				$p(2\times 2)1/8$	Triplet	Same as PBE + U with the filled defect state at 1.8 eV above O 2p band		5.50[f]/– 2.33[g]/–	
(110)	HF	Ce: ECP[h]; O: all-electron	Ce: DZ; O: 8-51G	Cluster	Isolated	Triplet	Excess electrons localization at the two Ce nearest neighbors	–	1.70/–	Herschend et al. [90]
(110)	MP2					Triplet	Same as for HF		3.26/–	Herschend et al. [90]
(100)	PW91 + U ($U'=5.0$)	PAW	500 eV	3L	$p(2\times 2)1/4$	Triplet	Insulating ferromagnetic ground state; defect state at 0.9 eV above O 2p band	–	2.27/–	Nolan et al. [51,52]

The effect of lattice relaxations is included.

[a] Spin-polarized (unrestricted Kohn–Sham) calculations.

[b] In *all* DFT + U studies the excess electrons occupied f states localized at two Ce nearest neighbors to the defect.

[c] O_2 molecule dissociation energy (in eV/atom).

[d] In Eq. (2), E_{def} might correspond to non-spin-polarized calculations (but not E_{O_2}); spin polarization amounted to ~0.02 eV (see Ref. [46]).

[e] Used to model subsurface defects.

[f] Value using projectors based on localized Wannier orbitals.

[g] Value using projectors based on atomic orbitals.

[h] Ce core: [Kr]$4d^{10}$.

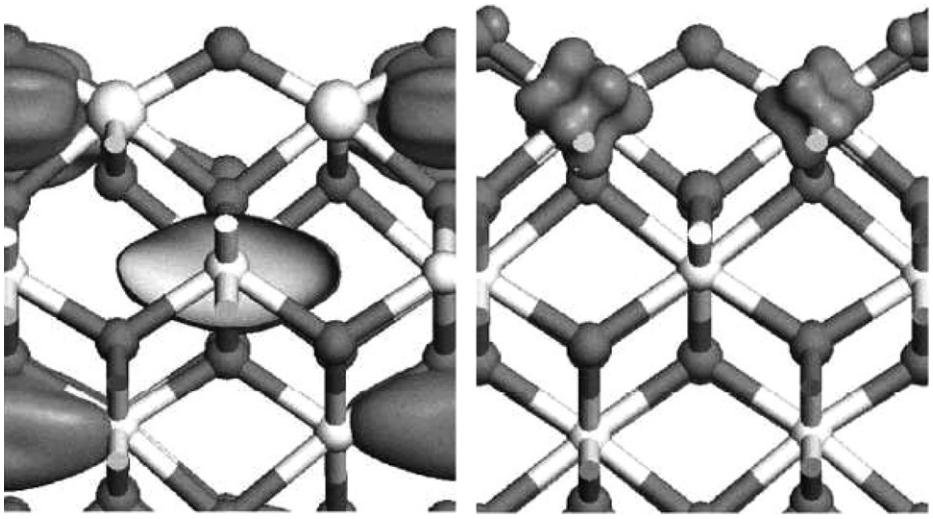

Fig. 23. Isosurface of spin density for the optimized defective (100) ceria surface ($\Theta_{def} = 1/4$) using (left) DFT (PW91) and (right) DFT + U (PW91 + U) methods. Large and small circles denote Ce and O atoms, respectively. Figure reproduced from Nolan et al. [51].

orbitals as determined by solving the Schrödinger equation numerically for the isolated atom in the reference configuration [Xe] $4f^1 5d^1 6s^2$. The (111), (110), and (100) surfaces were modelled using 4L, 7L, and 3L symmetric slabs (i.e., with oxygen defects on both sides), respectively. They considered a defect concentration of 1/4 using $p(2 \times 2)$ (hexagonal), $p(1 \times 2)$, $p(2 \times 1)$ for the (111), (110), and (100) orientations, respectively. The latter investigated reduced (111) and (110) surfaces employing both the LDA + U ($U' = 5.3$ eV) and PBE + U ($U' = 4.5$ eV) approaches [282] with two different choices for the localized Ce 4f-orbitals, namely standard atomic orbitals and the Wannier functions [283] that resulted from self-consistently calculated Ce 4f bands. The Wannier orbitals are becoming common in recent schemes to deal with strongly correlated electrons [284,285]. The U' values were determined using a method based on a linear response approach by Cococcioni and de Gironcoli [99], as applied to bulk Ce_2O_3 [48, 49]. Fabris et al. [50] considered a (111) 3L slab (4L to model subsurface defects) and defect concentrations of 1/2 and 1/4 using orthorhombic $p(\sqrt{3} \times 1)$ and hexagonal $p(2 \times 2)$ unit cells, respectively, whereas for a 6L (110) slab, they studied $\Theta_{def} = 1/4$ and 1/8 using $p(1 \times 2)$ and $p(2 \times 2)$ cells, respectively. Yet, they discussed in detail their results for the lower concentrations only.

Both DFT + U studies [50,52] considered lattice relaxations. In Ref. [50] only the upper half of the non-symmetric slabs (containing the defect) was allowed to relax. The resulting geometries of the (111) and (110) surfaces with defects at the surface layer could be compared and they were in good quantitative agreement. This suggests that structural properties do not significantly depend on the various variants of the DFT + U method used; however, that is not the case for the defect formation energies (see Sections 6.4 and 6.3.2). Similar to the PW91 relaxation pattern described above, as calculated by Yang et al. [46], with DFT + U the closest Ce and O atoms to the defect moved away from and towards the defect site, respectively [50,52]. However, the DFT + U surface relaxations were more complex than the corresponding GGA ones. Fig. 24(a) and (c) display the PBE + U optimized (111) and (110) with a surface defect concentration of 1/4 and 1/8, respectively, calculated with the localized Wannier orbitals as obtained by Fabris et al. [50], as examples.

For the (111) surface defect, for instance, the initial hexagonal symmetry around the defect is distorted, in contrast to the earlier PW91 calculations [46]. Namely, the *two* nearest neighbor Ce atoms relaxed further (0.16 Å) than the third one (0.11 Å). There is also an asymmetry in the amount by which the bond lengths between these Ce atoms and the oxygen atoms in the second oxygen atomic layer (next-nearest neighbors) were contracted (by 0.18 or 0.06 Å). The smallest contraction corresponded to oxygen atoms bonded to those two Ce atoms that relaxed further. The six surface oxygen atoms (third nearest neighbors to the defect) relaxed by 0.09 Å outward perpendicular to the surface (see Fig. 24(a)). There was some very weak perturbation of inner atomic layers. The resulting (asymmetric) relaxed (111) structures are compatible with recent STM images of oxygen vacancies at and below the surface [280], and are expected if Ce atoms in different oxidation states are present at the surface.

In contrast to the GGA results [46,50,51] which predicted metallic ground states, both DFT + U calculations [50,52] yielded insulating solutions with filled f states *in* the band gap. The spin analysis in Ref. [50] showed that the reduced (111) surfaces were antiferromagnetic while the defective (110) surface was ferromagnetic, in agreement with the PW91 calculations by Yang et al. [46], whereas in Ref. [52] the ground state was ferromagnetic for all three orientations; it is likely that the magnitude of the energy difference between the (open-shell) singlet and triplet solutions is small (i.e., less than 0.1 eV). This statement is supported by DFT and DFT + U calculations on partially reduced bulk CeO_2 and Ce_2O_3 for

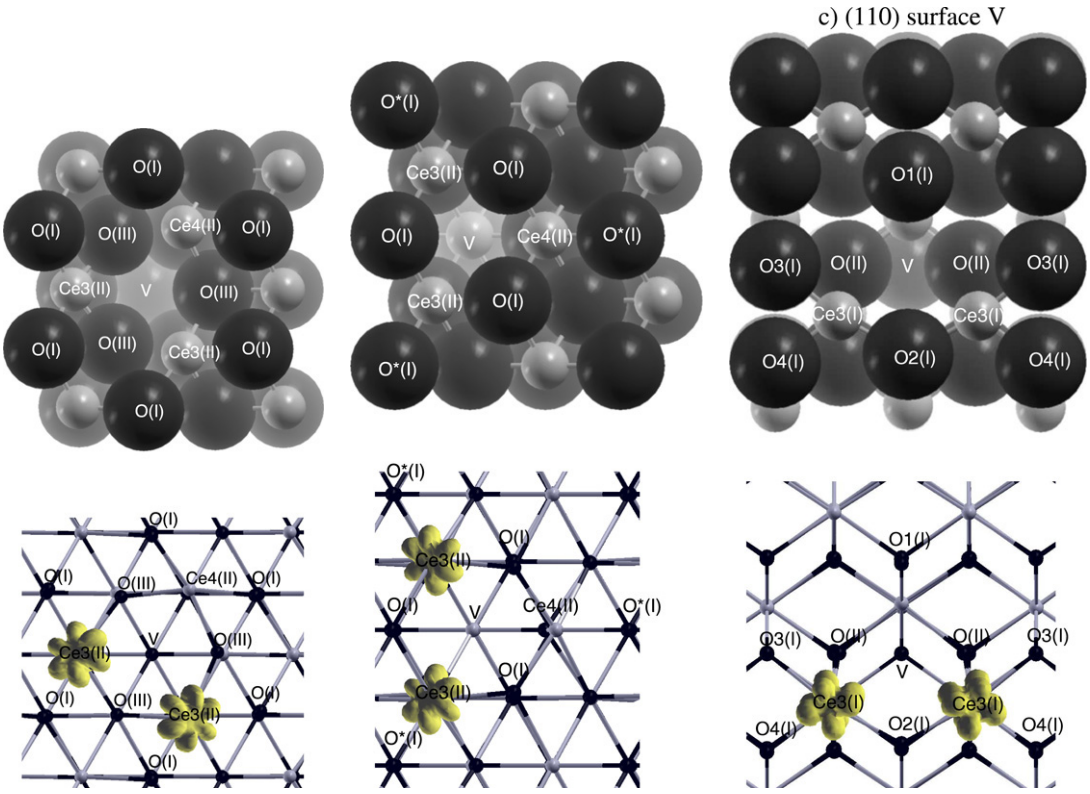

(a) (111) surface V. (b) (111) subsurface V. (c) (110) surface V.

Fig. 24. Top panel: Top view of the reduced (111) and (110) surfaces ($\Theta_{def} = 1/4$ and 1/8, respectively). Large and small circles denote O and Ce atoms, respectively. The index in parenthesis indicate the atomic layer (e.g., (I) outermost). The defect (V) is (a) at the (111) surface (b) below the (111) surface, and (c) at the (110) surface. Bottom (from left to right): The charge density of the gap states in Fig. 25(a), (b), and (c), respectively. Figure reproduced with permission from Fabris et al. [50].

which such difference was never larger than 0.1 eV [49,54,89,281,286].

Fig. 25(b), (c), and (d) display the spin-polarized PBE + U density of states of the reduced (111) and (110) surfaces of Fig. 24(a), (b), and (c), respectively [50]. The position of the occupied f states for the reduced (111) and (110) surfaces is approximately 1.5 and 1.4 eV, respectively, above the top of the valence band (1.9 and 1.8 eV in LDA + U). Nolan et al. [51,52] also obtained occupied f states in the band gap using PW91 + U which were at 1.1, 1.0, and 0.9 eV above the top of the valence band for the reduced (111), (110), and (100) surfaces, respectively, i.e., by about ~0.4 eV closer to the valence band edge compared to the results of Fabris et al. [50] (cf. Table 8). This difference may be due to the different DFT + U implementations. These occupied levels can be related to the observed additional emission in the UPS spectra of reduced surfaces [243,252,268,269,278] at binding energies of 1.2–1.5 eV above the top of the O 2p band (see Section 6.2).

For *all* reduced surfaces, the occupied states were due to the formation of Ce^{III} ions. Charge density isosurfaces of the gap states are shown at the bottom panel of Fig. 24 for a defect at the (111) surface [Fig. 24(a)], below the (111) surface [Fig. 24(b)], and at the (110) surface [Fig. 24(c)]. That for the (100) defective surfaces is displayed in Fig. 23(a). In all cases, localization of charge is observed at the *two* closest Ce atoms to the defect. Thus, the occupied states unequivocally arise from the formation of reduced Ce^{III} ions with an electronic configuration $4f^1$, in agreement with many experimental observations (see Section 6.2).

Herschend et al. [90] employed unrestricted (but also restricted open-shell) HF and MP2 methods to deal with the strong on-site correlation effects that tend to localize the excess electrons in atomic-like orbitals. They investigated the reduced $CeO_2(110)$ surface using an embedded cluster approach. The embedded cluster $Ce_{10}O_{20}$ used consisted of 3L of composition Ce_2O_8, Ce_6O_8, and Ce_2O_4 in the first, second and third layer, respectively. We refer to Ref. [287] for details about the embedding scheme. The oxygen defect was created by removing one of the central surface threefold coordinated oxygen atoms. An all-electron basis set for the O atoms and two different basis sets with an effective core potential for the Ce atoms were used (see Table 8). The larger basis set included f-functions and was of double-ζ valence quality while a reduced version did not contain f-functions and the most diffuse sp-shell. The smaller basis was used for those atoms which were *assumed* to remain Ce^{IV}, namely all but the four most central Ce atoms. Thus, in this model

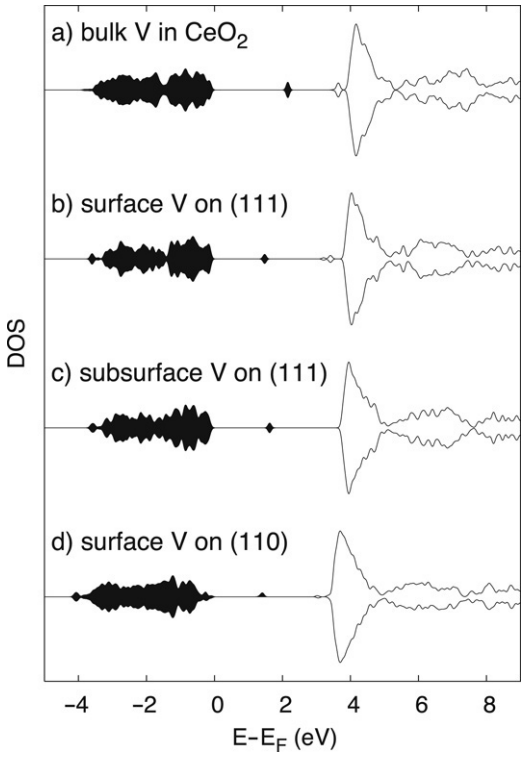

Fig. 25. Spin-polarized PBE+U density of states of ceria supercells containing one oxygen (V) vacancy (a) in the bulk, (b) at the (111) surface, (c) below the (111) surface, and (d) at the (110) surface. Figure reproduced with permission from Fabris et al. [50].

only first neighbor Ce^{IV} ions have the possibility to become Ce^{III}.

Upon defect formation, the geometries of the reduced clusters were only partially reoptimized at the UHF level by relaxing just one O atom and two Ce atoms closest to the defect (but the removed oxygen was threefold coordinated). Despite the relatively limited relaxation, the (UHF) resulting atomic displacements in the immediate vicinity of the defect led to longer Ce–Ce and shorter Ce–O distances in qualitative agreement with the periodic DFT + U studies [50,51].

With respect to the defect induced changes in the electronic structure, nothing importantly different from the results of the DFT + U calculations was obtained (cf. Table 8). At both the UHF and UMP2 levels, the ground state of the reduced cluster was a ferromagnetic insulator with the two excess electrons localized at the two closest Ce atoms, and a new occupied state appeared *in* the band gap. However, since they only reported densities of states from UHF calculations, the peak position cannot be directly compared to those of DFT+U. As we already mentioned using the example of TiO_2, the HF method is known to significantly exaggerate band gaps (see Section 3.3.1).

In brief, the embedded cluster calculations using UHF and UMP2 did *not* lead to qualitative differences in the calculated geometric and electronic structures compared to periodic DFT + U. However, *all* of them strongly disagree with plain DFT (LDA/GGA) results.

6.3.2. The surface defect formation energy

Despite the PW91 description of the electronic structure of reduced ceria surfaces being incorrect, the associated defect formation energies were calculated. Yang et al. [46] reported $E_f^{\frac{1}{2}O_2}$ values for the (111) defective surface with defects at the surface ($\Theta_{def} = 1/4$ and $1/2$) which are by about 0.2 eV larger than those for *subsurface* defects (cf. Table 8). For the (110) reduced structures, *surface* defects were preferred by about 0.5 and 0.9 eV at $\Theta_{def} = 1/4$ and $1/8$, respectively. The decrease of Θ_{def} from $1/2$ to $1/4$ and from $1/4$ to $1/8$ while increasing the closest defect separation between (most stable) defects by about 2.80 Å [$\frac{1}{2}a(\sqrt{3}-1)$] and 2.25 Å [$a(\sqrt{2}-1)$] at the (111) and (110) surfaces, respectively, resulted in the reduction of the defect formation energy by 0.6–0.7 eV. Moreover, less energy is required to form stable defects at the (110) surface than on (111) (cf. 3.17 (110) and 3.21 eV (111) for $\Theta_{def} = 1/4$ in Table 8). This dependence of $E_f^{\frac{1}{2}O_2}$ on the surface orientation was already noticed in the earlier force-field calculations [43,44]. We note here and discuss later in this section that the preference for the subsurface to accommodate oxygen defects at the (111) oriented surface using PW91 is *not* in particularly good agreement with the recent experimental observations by Esch et al. [280]: upon short annealing, surface and subsurface defects formed in the same proportion (cf. Section 6.2).

The $E_f^{\frac{1}{2}O_2}$ values as obtained with DFT + U deserve some discussion. Inspection of Table 8 reveals that according to *all* DFT + U calculations [50,52], i.e., for all different implementations, the formation energies of defects at the (111) surface are larger than for the (110) orientation (independent of the defect location at the (111) surface). These findings are in qualitative agreement with those obtained using PW91 discussed above [46]. However, we observe that actual values may lie within a wide energy range of up to ~3 eV depending on the actual details of the DFT + U implementations used.

Fabris et al. [50] provided *four* completely different values for each defect position at the (2×2) reduced (111) and (110) structures ($\Theta_{def} = 1/4$). For the surface positions at the (111) and (110) surfaces, the PBE + U (LDA + U) energies with the projector functions based on standard atomic orbitals were 2.15 (2.92) and 1.57 (2.33) eV respectively. When the Wannier orbitals were employed the corresponding values became 4.95 (6.10) and 4.42 (5.50) eV, respectively. The values for the subsurface position at the (111) surface were 1.89 (2.95) eV with atomic orbitals, and 4.81 (6.25) eV with Wannier orbitals.

Nolan et al. [52] considered only the surface position at the (111), (110), and (100) surfaces and computed $E_f^{\frac{1}{2}O_2} = 2.60$, 1.99, and 2.27 eV, respectively, at $\Theta_{def} = 1/4$ using PW91 + U ($U' = 5.0$) (cf. Table 8). The values for the (111) and (110) orientations differ by ~0.4 eV from those of Ref. [50] that were calculated using projectors based on standard atomic orbitals (as in Ref. [52]) and the PBE + U ($U' = 4.5$) functional (cf. 2.60 with 2.15 eV (111) as well as 1.99 with 1.57 eV (110) in Table 8). The reason for this discrepancy may be related to the different U' values, but also to the choice for the pseudopotentials, cutoff, and other details of the

model. However, much more *dramatic* effects were obtained for different choices for the projector functions (but the same functional and computational technique), as well as for different underlying functionals (GGA or LDA) with identical projector functions. The calculated values of Fabris et al. [50] using the self-consistently calculated Wannier functions are about twice as large as those obtained from standard atomic orbitals, whereas discrepancies due to different underlying functionals are less severe. We deem the performance of DFT + U for predicting defect formation energies at ceria surfaces *unsatisfactory*. However, does the *relative* stability of surface/subsurface defects depend on the methodology?

The surface/subsurface stability at the (111) surface showed *qualitative* different results between PBE + U and LDA + U calculations [50]. Specifically, the subsurface position was more stable in the PBE + U approximation by 0.26 and 0.14 eV when using the standard and the Wannier local functions, respectively (cf. Table 8). The subsurface preference is in agreement with the PW91 result by Yang et al. [46] (0.18 eV). Quite differently, the LDA + U predicted the surface defects to be more stable by 0.03 (atomic orbitals) and 0.15 eV (Wannier orbitals). The latter are in better agreement with the already mentioned high-resolution STM of the (111) surface where surface and subsurface defects were initially present in equivalent proportions [280]. The reason for this discrepancy between the LDA+U and GGA+U calculations is unclear. This inconsistency is particularly disturbing because of the failure to produce reliable *relative* energies of defect formation in this specific example.

A possible remedy to these problems is, in principle, the use of hybrid functionals [58,59,80,81,84,85], which include a certain amount of Fock exchange. We have seen above that in transition (d) metal oxides (e.g., TiO_2 [12,23,25], V_2O_5 [40]) hybrid functional approaches yield accurate oxygen defect formation energies and a proper description of the extent of the localization of the electrons left behind upon reduction. But also, it has been recently shown that they can correctly reproduce the ground state properties of strongly correlated systems (e.g., containing f electrons) for which LDA and GGA approximations are known to be from inadequate to completely wrong [75–77,89,281,288–292]. As already mentioned, such calculations have *not* been performed for partially reduced ceria systems yet, but would be desirable. The reason may be that electronic convergence of spin-polarized DFT calculations with hybrid functionals is extremely hard to achieve for systems with (few) localized f electrons [89].

The recent cluster calculation at the MP2 level by Herschend et al. [90] predicted a defect formation energy at the Ce(110) surface of 3.26 eV. Compared to the DFT + U values in Table 9, the MP2 result deviates by about 0.9–2.2 eV. The closest LDA + U value of 2.33 eV was obtained using the standard projectors [50]; an approach that had produced the experimentally observed similar stabilities for defects at the surface and subsurface positions at the (111) surface. Unfortunately, DFT results are not available for the cluster model, which — by comparison with calculations on periodic models — would allow for a judgement of the quality of the cluster model.

6.4. Reduced CeO_2 bulk

The above-discussed limitations of LDA and GGA functionals in dealing with the change in valency of cerium atoms upon reduction of ceria surfaces also apply to the reduced bulk. In terms of the electronic structure, partially reduced ceria represents an intermediate case between CeO_2 and Ce_2O_3 in which all the Ce ions are in the Ce^{IV} and Ce^{III} oxidation state, respectively. Ce_2O_3 is an antiferromagnetic insulator with a single *occupied* Ce 4f peak 2.4 eV below the conduction band [293], which is formed to a large extent by Ce 5d + 4f states. Local and gradient-corrected functionals yield a ferromagnetic *metallic* and semi-metallic (with ∼10 meV between the occupied f state and the bottom of the conduction band) ground state, respectively, when the Ce 4f electrons are treated explicitly as valence electrons [49,54,77,89,281,286,294]. DFT + U and hybrid functionals were employed in the study of Ce_2O_3 [49,54,77,89,281,286], however for CeO_{2-x} with $0 < x < 0.5$, *only* plain DFT (LDA/GGA) and DFT+U calculations were performed [45–47,49,50,53,54]. Similar to the ceria surfaces, a broad range of calculated defect formation energies was obtained from these investigations, and the question for a converged bulk defect formation energy has remained unanswered.

Skorodumova et al. [45] performed spin-polarized FP-LMTO [295,296] calculations with the PW91 functional (see Ref. [297]). They employed a $Ce_{32}O_{64}$ unit cell consisting of eight elementary cells of CeO_2 for which relaxations of the atomic positions upon reduction were probably considered, however not explicitly mentioned. They treated the Ce 4f states within two simple models, as valence band states and as fully localized core states. In the former case, the 5s, 5p, 5d, 4f, and 6s basis functions were included in the Ce valence basis set (12 valence electrons), whereas only 5s, 5p, 5d, and 6s states were included when the f electron was treated as a localized core (i.e., 11 valence electrons). The basis for the O atom contained 2s, 2p, and 3d basis functions.

For the calculation of the oxygen defect formation energy in CeO_2, Skorodumova et al. [45] removed an oxygen atom from the $Ce_{32}O_{64}$ cell while treating the 4f electrons of *all* Ce atoms as valence electrons and obtained a value of 4.55 eV with respect to $1/2O_2$ (see Table 9). Moreover, they also created a defect in the 96 atoms cell with two Ce^{III} centers at different Ce lattice positions, i.e., the 4f electrons of two Ce atoms where treated as core electrons. (Note that in Eq. (2) both the unreduced and reduced cells contained the two Ce^{III} species.) The defect formation energy for oxygen *next* to the pair of Ce^{III} sites was lowest, and by 4.29 eV *lower* than for the cell in which electron localization had not been imposed, i.e., $E_f^{\frac{1}{2}O_2} = 0.26$ eV. Using these numbers Skorodumova et al. [45] argued that the oxygen vacancy formation in CeO_2 is greatly facilitated by the simultaneous localization of two electrons into f states of two cerium atoms neighboring the oxygen that leaves; however, the predictive power of this approach is limited since the

Table 9

Oxygen defect formation energies, $E_f^{\frac{1}{2}O_2}$ (in eV/atom), in bulk CeO_2 and associated changes in the electronic structure (see Section 6.4)

Method[b]	Core-electrons	Basis set[c]	Unit cell	Spin state	Electronic structure[d]	$E_d^{\frac{1}{2}O_2}$[e]	$E_f^{\frac{1}{2}O_2}$	References
PW91	All-electron	LMTO LMTO[f]	$Ce_{32}O_{64}$, $(2\times2\times2)$	–	Not discussed	–	4.55 0.26	Skorodumova et al. [45]
PW91	PAW	408 eV	Ce_4O_8, $(1\times1\times1)$	–	Not discussed	3.02	4.73	Yang et al. [46]
PBE	PAW	400 eV	$Ce_{32}O_{64}$, $(2\times2\times2)$	–	Not discussed	–	3.62	Jiang et al. [47]
LDA/PBE	US-PP	408 eV	Ce_8O_{16}, $(2\times1\times1)$	Triplet	Metallic ground state	–	–	Fabris et al. [48–50]
LDA/PW91	PAW	400 eV	$Ce_{32}O_{64}$, $(2\times2\times2)$	Triplet[g]	Metallic ground state	–	4.09/3.13	Andersson et al. [54]
LDA + U ($U'=6.3$)	PAW	400 eV	$Ce_{32}O_{64}$, $(2\times2\times2)$	–	Not discussed	–	2.35[h]	Jiang et al. [47]
LDA + U ($U'=5.3$)	US-PP	408 eV	Ce_8O_{16}, $(2\times1\times1)$	–	Insulating ground state	–	6.74[i]/3.45[h]	Fabris et al. [48–50]
PBE + U ($U'=4.5$)				Singlet	Insulating antiferromagnetic ground state; occupied Ce f state at 2.1 eV above O 2p band		5.55[i]/2.58[h]	
LDA + U ($U'=6.0$)	PAW	400 eV	$Ce_{32}O_{64}$, $(2\times2\times2)$	Triplet[g]	Insulating ground state; occupied Ce f states at 1.4 eV above O 2p band	–	3.61[h]	Andersson et al. [54]
PW91 + U ($U'=5.0$)				Triplet[g]	Insulating ground state as with LDA + U		2.88[h]	
PW91 + U ($U'=5.0$)	PAW	500 eV	$Ce_{32}O_{64}$, $(2\times2\times2)$	–	Insulating ground state; occupied Ce f state at ∼1.6 eV above O 2p band	–	3.39[h]	Nolan et al. [53]

The effect of lattice relaxations is included.[a]

[a] In some studies the inclusion of geometry relaxations upon reduction was neither explicitly mentioned nor denied (see text).
[b] Spin-polarized (unrestricted Kohn–Sham) calculations.
[c] The 4f electrons were treated as valence electrons unless otherwise specified.
[d] In *all* DFT + U studies the excess electrons occupied f states localized at two Ce nearest neighbors to the defect.
[e] O_2 molecule dissociation energy (in eV/atom).
[f] The 4f electrons of two Ce atoms closest to the defect were treated as core electrons (see text).
[g] The ferromagnetic and antiferromagnetic solutions differ by less than 1 meV.
[h] Value using projectors based on atomic orbitals.
[i] Value using projectors based on localized Wannier orbitals.

distribution of reduced centers has to be assumed. Moreover, the calculated energies cannot be compared between systems with a different number of Ce^{III} sites.

Yang et al. [46], Jiang et al. [47], and Fabris et al. [48–50] also performed gradient-corrected calculations of reduced ceria using a 12-, 96-, and 24-atom unit cell, respectively, in which the 4f electrons of all cerium atoms were treated as valence electrons. The latter also performed calculations with the LDA. For all calculations the atoms were allowed to relax upon defect formation (relaxations were not explicitly mentioned in Ref. [46], though). Recently, Andersson et al. [54] considered the 96-atom cell and both LDA and PW91.

The PBE defect formation energy of 3.62 eV for the $(2\times2\times2)$ supercell of Jiang et al. [47] is by about 0.5 eV larger than the recent PW91 value of 3.13 eV [54], using the same supercell. These values are by 0.9 and 1.4 eV smaller than the FP-LMTO-PW91 value of 4.55 eV [45], respectively (cf. Table 9). Several factors may contribute to these differences such as a different core description (PAW in Refs. [47] and [54] and all-electron in Ref. [45]), the number of integration points in the irreducible wedge of the Brillouin zone (Γ-point in Ref. [47] and eight k-points in Refs. [45]) and [54]; one needs more than just the Γ-point for metallic systems. The extent of lattice relaxations considered may also differ and last but not least, deviations may be partly reflecting differences in the calculated O_2 dissociation energies as discussed in Section 3.3.2. However, the $E_d^{\frac{1}{2}O_2}$ values used in Refs. [45,47], and [54] were not reported. It is clearly non-trivial to understand the origin of these significant differences without careful testing.

Yang et al. [46] calculated a PW91 defect formation energy in bulk ceria of 4.73 eV for the $(1\times1\times1)$ supercell. Thus, according to their surface defect formation energies, oxygen defects were predicted to be more stable within the outermost oxygen layers [(111): subsurface; (110): surface] than in the bulk (cf. Table 8). Moreover, the $E_f^{\frac{1}{2}O_2}$ bulk value is by about 1.1 and 1.6 eV larger than that reported by Jiang et al. [47] and Andersson et al. [54], respectively, for an oxygen defect concentration eight times smaller (cf. Table 9). The $E_f^{\frac{1}{2}O_2}$ values in Refs. [46,47] and [54] were obtained with the same computational technique (i.e., working with the same code [157]) and may be reflecting some concentration dependence; however, to discuss such effects quantitatively, the used methodology has to be identical (i.e., same cutoff, equivalent k-point meshes, etc.).

As for reduced ceria surfaces (cf. Section 6.3.1), Fabris et al. [48–50] found that using LDA and PBE the ground state of defective ceria was *metallic* with the two excess electrons left upon reduction of the Ce_8O_{16} cell evenly distributed among *all four* Ce nearest neighbors to the defect in a parallel ordering (see Table 9). Consistently, these four atoms relaxed symmetrically with respect to the vacany (the four Ce atoms 0.18 Å outward, while the six O atoms 0.15 Å inward) [48]. Hence, as previously discussed, in this geometry there are not two neighboring Ce^{III} ions to the oxygen defect. The metallic character of partially reduced CeO_2 with LDA and PW91 has been once more recently reported [54].

The Hubbard-U correction to the local and gradient-corrected functionals resulted in insulating (ferromagnetic or antiferromagnetic) ground states, and the expected localization of the excess electrons on *two* (rather than four) neighboring Ce atoms [48–50,53,54] (see Table 9). The DFT + U solutions exhibited a complex relaxation pattern of the defect's nearest and next-nearest neighbors with the relaxed structure being relatively insensitive to the details of the functionals (LDA + U or PBE+U) [48]. For instance, the Ce^{III} and Ce^{IV} atoms around the defect in a $(2\times1\times1)$ cell moved outward by 0.11 and 0.17 Å, respectively. Five O atoms relaxed inward (four by 0.12 Å, one by 0.25 Å), and one outward by less than 0.03 Å. All other atoms in the supercell relaxed by less than 0.05 Å [48]. This is a renewed demonstration of the importance of self-consistent relaxation of reduced ceria using functionals that can correctly reproduce its ground state electronic properties.

As noticed for ceria surfaces (cf. Section 6.3.2) the DFT + U calculated bulk defect formation energy may also lie within a wide energy range (~4 eV) depending on the DFT + U implementation used; manifestly this is most unsatisfactory and undesirable (cf. Table 9). For example, the $E_f^{\frac{1}{2}O_2}$ values at a defect concentration of 1/16 were 5.55 eV (PBE + U) and 6.74 (LDA + U) with Wannier orbitals, whereas using standard atomic orbitals values of 2.58 eV (PBE + U) and 3.45 (LDA + U) were calculated [50]. As observed above, the effect of the type and extent of the localized functions is most prominent, whereas that of the different underlying functional is less striking, i.e., ~1 eV, with the LDA + U values being larger than the PW91 + U values with the same projector functions.

As for the previously discussed DFT (i.e., without U') results, the difference between the DFT + U defect formation energies corresponding to different unit cell sizes may feature some dependence on the defect concentration. For example, from the LDA + U values with projectors based on atomic orbitals in Table 9, one sees that the value of 3.45 eV ($U'=5.3$ eV) [50] with the Ce_8O_{16} cell is by 1.1 eV larger compared to that (2.35 eV) calculated at a four times lower defect concentration ($U'=6.3$ eV) [47]. However, the recent LDA+U value of 3.61 eV ($U'=6.0$ eV) [54] would indicate the increase in $E_f^{\frac{1}{2}O_2}$ as the vacancy concentration decreases.

Similarly, the PBE + U ($U'=4.5$ eV) [50] value of 2.58 eV with the Ce_8O_{16} cell is by about 0.3 and 0.8 eV smaller compared to the PW91 + U ($U'=5.0$ eV) values of 2.88 and 3.39 eV with the four times larger cell ($Ce_{32}O_{64}$) [53,54]. These ambiguities are in part due to the different U' values and are problems that must be lived with until a better DFT + U prescription is formulated. Thus, from the data in Table 9, it is too early to draw a definite conclusion about the converged energy value to form an isolated oxygen defect in bulk CeO_2. We note that defects are found to be more stable at the surfaces than in the bulk with DFT+U, consistent with the PW91 results of Yang et al. [46].

Experimental values of the heat of reduction per oxygen vacancy determined by thermogravimetry, electrical conductivity, and calorimetry, are in the 3.94–4.67 eV range [298]. The results obtained with GGA functionals lie more or less within the

experimental range. In all likelihood, this is related to a fortuitous cancellation of errors, and not related to a proper description of the underlying physical properties of reduced ceria.

6.5. Summary CeO_2

Theoretical studies on reduced ceria systems are very recent and as a whole they do *not* constitute a systematic and conclusive database, in particular as far as the formation energy of the isolated neutral oxygen defect is concerned. Nevertheless, the following picture emerged: The main effect of the removal of lattice oxygen atoms from ceria is the important change in the nature of the f electrons, namely from valence to core-like. A theoretical approach that would correctly describe both situations has to take proper account of the strong on-site f–f interactions that push the f electrons towards localization. In particular, the formally two electrons left in the system upon formation of a neutral oxygen defect drive the $Ce^{IV} \rightarrow Ce^{III}$ reduction of two nearest neighbor cerium atoms of the defect. Using the GGA (but also LDA), the resulting electronic structure of reduced ceria systems is simply *wrong*. The ground state is metallic and the excess electrons are evenly shared by *all* cerium atoms; not even a perceivable indication of the existence of occupied states that "would like to split" from the bottom of the conduction band is to be seen. The use of periodic DFT + U approaches (independent of the particular implementation) that take explicit account of electron interactions in the narrow f band, yields the expected insulating state and localization of the excess electrons. These results have been corroborated by MP2 cluster studies (i.e., by the simplest explicit treatment of electron correlations). Hybrid functionals, which include a portion of exact exchange, have not yet been used in (periodic or cluster) studies on partly reduced ceria, but would be most desirable.

The geometrical and electronic structures of reduced ceria systems have to be calculated self-consistently employing a method that is able to properly describe the electronic structure, i.e., plain LDA or GGA *cannot* be applied. The latter yield a locally symmetric environment of oxygen defects which is inconsistent with the locally distorted environment produced by the existence of neighboring Ce^{IV} and Ce^{III} ions. Yet, the amplitude of the displacements is fairly small (less than 0.2 Å).

The two localized f electrons (per oxygen defect) on nearest neighbor Ce atoms to the defect in reduced ceria systems have been found (DFT + U) to be antiferromagnetically coupled in some systems, but ferromagnetically coupled in others; the answer to the magnetic ground state may vary depending on the DFT + U implementation. The energy difference between the triplet and closed-shell singlet states is estimated to be less than 0.1 eV. As for the isolated defect formation energy, the DFT + U results are not final. Values depend *significantly* on the specific implementation, in particular, the nature and extent of the localized f orbitals defining the projection operators, the underlying level of theory (LDA or GGA), and the actual value of the effective Coulomb parameter U'. From the reviewed theoretical studies we gather that for reduced ceria surfaces, one may not even be able to obtain reliable energy differences, which is particularly discouraging. Specifically, the relative stability of surface and subsurface defects at the $CeO_2(111)$ surface depend on the choice of the functional; while GGA + U favors subsurface sites ($\Theta_{def} = 1/4$), LDA + U favors sites at the surface leading to better agreement with experiments.

7. Similarities and differences between TiO_2, ZrO_2, V_2O_5, and CeO_2

Table 10 summarizes the main structural and electronic properties as well as energetic quantities related to the formation of isolated oxygen defects in TiO_2, ZrO_2, V_2O_5, and CeO_2, as *examples* of reduced TM and RE oxides, and the ability of state-of-the-art methods to describe them.

From comparison of experimental data and those in Tables 1 and 3–9, we conclude that oxygen defects in TiO_2 (rutile and anatase) and V_2O_5 systems belong to the same class: The excess electrons occupy d states ~1 eV below the conduction band in the band gap, and lattice relaxations are sizable. In V_2O_5 in particular (we considered the $V_2O_5(001)$ surface), removal of a vanadyl oxygen atom results in large displacements and the formation a V–O–V bond between the weakly interacting layers. As far as the electronic structure is concerned, the two electrons left at the $V_2O_5(001)$ surface localize (after relaxation) at the V sites forming the interlayer bond (one electron at each V), driving the $V^V \rightarrow V^{IV}$ reduction. In TiO_2, upon formation of a bridging oxygen defect at the rutile $TiO_2(110)$ surface in particular, the excess electrons occupy Ti 3d states localized at two Ti atoms close to the defect (but not necessarily both nearest neighbors).

In reduced ZrO_2, the two electrons occupy a state ~2.6 eV above the valence band in the band gap. The state is formed (mainly) by a linear combination of d orbitals on nearest neighboring Zr atoms, but the charge is for the most part localized at the vacant site. With the large band gap, the little relaxation upon reduction, and the "trapped" electrons, the oxygen defects in ZrO_2 resemble the F-centers in the ionic oxide MgO. Thus, they are different from those of TiO_2 and V_2O_5.

CeO_2 with empty f-states in the ≈6 eV wide O 2p–Ce 5d band gap belongs to yet another class than the TiO_2, ZrO_2, and V_2O_5 TMs with O 2p–M d band gaps (M = Ti, Zr, and V). After the creation of oxygen defects, the excess electrons populate f states that split from the conduction band (its bottom now formed by Ce 5d4f states), forming an extremely narrow band which leads to localized electrons in atomic-like orbitals of neighboring Ce sites to the defect. Lattice relaxations are distinct, but small.

When may we expect the excess electrons to remain at the oxygen vacant site of TM oxides as it is described in ionic oxides such as MgO? In order to answer this question *qualitatively*, we consider the Madelung potential at the oxygen sites (that become vacant) in bulk TiO_2 (rutile/anatase), t-ZrO_2, and V_2O_5 and compare to MgO. The results are listed in Table 11, as obtained from the Ewald summation assuming formal charges (V^{form}), as well as those resulting from self-consistent PW91 calculations (V^{PW91}) performed for this

Table 10
Summary of the main properties of isolated neutral oxygen defects in TiO_2, ZrO_2, V_2O_5, and CeO_2 systems and band gaps

Property	TiO_2	ZrO_2	V_2O_5	CeO_2
Geometrical relaxation	Sizable rearrangements involving a number inner layers (∼0.3 Å)	Fairly small and localized (<0.2 Å)	Large displacements (∼1 Å); V–O–V bond formation	Small displacements (<0.2 Å) involving up to next-nearest neighbors
Band gap [eV] Obs./Calc.[a]	Rutile: 3.0/1.8 Anatase: 3.2/2.1	5.8–6.6[b]/3.9	2.3/2.0	6.0/5.6[c]
States occupied by the excess electrons (Obs.)	Ti 3d in the gap (∼1 eV below the conduction band)	Zr 4d in the gap (∼2.3 eV above the valence band)	V 3d in the gap (∼1 eV below the conduction band)	Ce 4f in the gap (about 1.2–1.5 eV above the valence band)
Excess electrons distribution	Localized at two neighboring Ti sites (Ti^{III})	Trapped at the defect site; F-*like* center	Localized at the two V sites forming a bond (V^{IV})	Localized at two neighboring Ce sites (Ce^{III})
Quantum mechanical level of description of the electronic structure	B3LYP (periodic/cluster): Excess electrons localized GGA (periodic): Fairly spread	GGA/LDA (periodic): Well described	B3LYP (cluster): Excess electrons localized GGA (periodic/cluster): Moderately delocalized	DFT + U (periodic) and MP2 (cluster): Well described GGA/LDA: Fully wrong
Calc. $E_f^{\frac{1}{2}O_2}$ [eV/atom][d]	TiO_2(110) (rutile): 3.0 (GGA); 2.7[e,f] (B3LYP)	t-ZrO_2(101): 5.5 (GGA) 5.6 (B3LYP)[f]	V_2O_5(001): 1.9 (GGA) 1.2 (B3LYP)[g]	CeO_2(110): 1.6–5.5 (DFT + U); 3.3 (MP2)[f]
Obs. $E_f^{\frac{1}{2}O_2}$ [eV/atom][h]	3.9–5.7 (rutile)	Not found	1.3–1.54 (molten)	3.9–4.7

[a] Values of the band gap as obtained with gradient-corrected functionals.
[b] t-ZrO_2 phase, VUV reflectance results.
[c] The gap between the valence and conduction bands formed by (predominantly) the O 2p and Ce 5d states, respectively.
[d] For selected examples from Tables 3 to 9.
[e] Estimated.
[f] Non-validated cluster model.
[g] Validated cluster model.
[h] In bulk phases.

Table 11
The Madelung potential in volt at the site of an oxygen atom in the bulk of V_2O_5, TiO_2, t-ZrO_2, and MgO

System	V^{form}	Formal charge	V^{PW91}	PW91 charge
V_2O_5	−24.31	+5	−4.72	+1.10
TiO_2 rutile	−25.68	+4	−8.73	+1.30
TiO_2 anatase	−26.19	+4	−8.51	+1.30
t-ZrO_2	−22.98	+4	−12.41	+2.16
MgO	−23.76	+2	−20.10	+1.69

In V_2O_5 and t-ZrO_2, this oxygen atom is the vanadyl $O^{(1)}$ and the $O^{(4)}$ atom, respectively (cf. Figs. 11 and 17). The Madelung potentials are obtained using formal charges, V^{form}, and self-consistent charges on the metal atoms, V^{PW91}; corresponding charges of the metal atoms in the second and fourth columns (see text).

review using the VASP code [157] (PAW potentials and 400 eV cutoff); these are site-projected DOS (onto non-overlapping spheres), integrated up to the Fermi level. Lattice constants were optimized.

The absolute values of V^{PW91} follow the V_2O_5 < TiO_2 < t-ZrO_2 < MgO trend. The difference between the self-consistent and formal charges and that between V^{PW91} and V^{form} is smallest for the highly ionic MgO (followed by t-ZrO_2). This indicates that the TM oxides are characterized by significant covalent bonding. Ionic solids with large lattice enthalpies, reflecting large Madelung energies, have large band gaps (cf. observed band gaps: MgO, 7.8 eV; t-ZrO_2, 5.8–6.6 eV; TiO_2, 3.0/3.2 eV (rutile/anatase); V_2O_5, 2.3 eV). For *all* three TM oxides (and MgO), population of states in the band gap upon reduction has been observed.

As in MgO, the attractive Madelung potential in t-ZrO_2 is sufficiently strong to stabilize the excess electrons at the vacant site. However, this is not the case in TiO_2 and V_2O_5, and therefore the electrons are expected not to be trapped at the vacant site but localized at cation sites formerly neighboring the oxygen removed. The effect of lattice relaxation is not considered in these simple arguments. This qualitative considerations apply to the reduction of insulating simple and TM oxides with fairly sizable band gaps (formed predominantly by the oxygen p and the metal d states); they are not suitable for RE oxides such as CeO_2, where other mechanisms related to the localization of f electrons in nearly core-like orbitals upon oxygen removal apply.

The defect formation energies in the TM oxides follow the V_2O_5 < TiO_2 (rutile) < TiO_2 (anatase) < t-ZrO_2 trend (cf. Table 10). To rationalize this trend, we calculated $E_f^{\frac{1}{2}O_2}$ for the example of defects in the bulk, employing $V_{24}O_{60}$, $Ti_{90}O_{180}$ (rutile), $Ti_{32}O_{64}$ (anatase), and $Zr_{54}O_{108}$ (t-ZrO_2) unit cells with PW91. The corresponding $E_f^{\frac{1}{2}O_2}$ values of 1.98, 4.05, 4.27, and 5.41 eV are plotted as a function of the Madelung potential (V^{PW91}) in Fig. 26; for MgO $E_f^{\frac{1}{2}O_2}$ equals 6.95 eV [70]. The trend is roughly linear for both relaxed and unrelaxed structures. In the following, we qualitatively discuss the observed trends, however, keeping in mind that these numbers might not correspond to the isolated defect limit and that size effects can vary from one system to the other.

In V_2O_5 lattice relaxations facilitate reduction enormously; they become less important as the Madelung potential becomes more attractive (i.e., the system more ionic). Note that

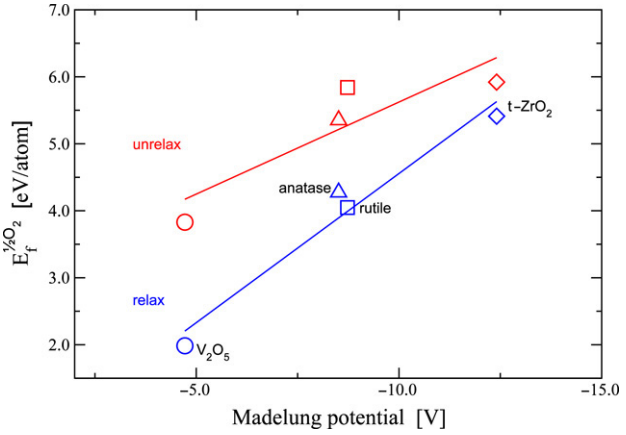

Fig. 26. Defect formation energies from PW91 calculations for isolated defects in V_2O_5 ($V_{24}O_{60}$), TiO_2 rutile ($Ti_{90}O_{180}$), TiO_2 anatase ($Ti_{32}O_{64}$), and t-ZrO_2 ($Zr_{54}O_{108}$) with respect to the Madelung potential at the oxygen site of the unreduced structures. The red (blue) symbols correspond to the unrelaxed (relaxed) structures.

relaxations are larger for the rutile than for the anatase phase, the latter being more difficult to reduce, however the Madelung potential at oxygen sites in the two TiO_2 phases is very similar.

It is found that the Madelung potential (which correlates with the band gap), in a way "controls" the defect properties, namely the less attractive the potential, the smaller the band gap (the larger the relaxations), the less likely trapped electrons will be found at the vacant site, and the smaller the defect formation energy. In turn, the challenge for local and gradient-corrected functionals increases as band gaps narrow.

The existence of occupied states in the gap of TMs is *not* reproduced with local and gradient-corrected functionals for the *narrow*-gap materials, namely, TiO_2 and V_2O_5 (see Fig. 27). Band gaps are actually narrower according to gradient-corrected DFT (cf. calculated PW91 band gaps: MgO, 4.5 eV; t-ZrO_2, 3.9 eV; TiO_2, 1.8/2.1 eV (rutile/anatase); V_2O_5, 2.0 eV), and defect states are *not* split from the conduction band. This is in contrast to t-ZrO_2 (and MgO) for which defect states are qualitatively well described with functionals that do not contain Fock exchange, i.e., the GGA deficiencies are less critical for wide-gap (5–15 eV) systems. The well-known significant overestimation of electron delocalization and metallic character by these functionals render the description of the electronic structure of reduced narrow-gap systems inaccurate. The extent to which the excess electrons are found to spread, however, varies. Nonetheless, one can safely state that gradient-corrected

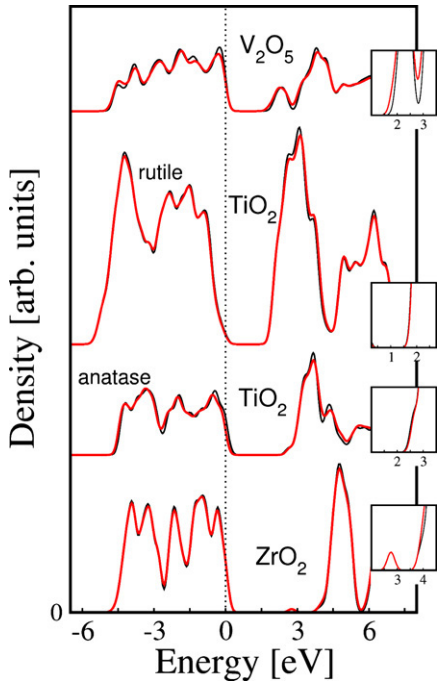

Fig. 27. Spin-polarized DOS from PW91 calculations for V_2O_5 ($V_{24}O_{60}$), TiO_2 rutile ($Ti_{90}O_{180}$), TiO_2 anatase ($Ti_{32}O_{64}$), and *t*-ZrO_2 ($Zr_{54}O_{108}$) bulk cells with a single oxygen defect (red). The ground state is triplet for V_2O_5 whereas is closed-shell singlet for TiO_2 (rutile and anatase) and ZrO_2. The DOS of the defect free cell is shown as a reference (black). The majority spin-component (α-spin) is shown in every case. The energy zero is set to the top of the O 2p band. The curves are smoothed by a Gaussian level broadening of 0.2 eV. The four inserts show the energy region around the bottom of the conduction band (the *x* and *y* scales in the inserts are the same).

functionals give *too delocalized* excess-electrons, but describe the significant defect induced relaxations moderately well. These inherent problems to local and GGA functionals peak for reduced ceria, leading to the *complete* failure of the method to describe reduced ceria's electronic structure and geometry.

The predicted delocalization of charge (that reduces Coulomb repulsion because local and gradient-corrected functionals are *not* free of the self-interaction energy) can be corrected using hybrid functionals within DFT. As applied to reduced titania (periodic and cluster) and vanadia (cluster), they *properly* describe the charge localization at nearby cation sites, and the existence of occupied states in the band gaps. In addition, hybrid functionals yield *improved* band gaps. No hybrid functional study on defective ceria has been reported, but DFT + *U* and MP2. The latter are also found to improve results over (plain) DFT.

Turning to the accuracy of the calculated defect formation energies, the use of hybrid approaches should reduce the characteristic overbinding of gradient-corrected functionals, for *all* systems. For instance, cluster (B3LYP) studies on the V_2O_5(001) and TiO_2(110) surfaces yielded a reduction of about 0.7 and 0.3 eV, respectively. The latter is expected to increase after the proper inclusion of structure relaxation. No hybrid numbers exist for ZrO_2 (that are reliable) and CeO_2 (at all). Those obtained with DFT + *U* for CeO_2 lack predictability, and those with MP2 corresponded to a somewhat restrictive cluster model. One point that cannot be emphasized strongly enough is *validation* of the models, (embedded) clusters in particularly. *First* perform a calculation using GGA and compare to either bigger clusters or periodic results, *then* perform cluster studies that include Fock exchange. An example is the (fully self-consistent) V_2O_5 cluster study using GGA and B3LYP functionals. Thus, the question for a converged surface (and bulk) defect formation energy for TiO_2, ZrO_2, and CeO_2 remained mostly unanswered, but well worth further research and study.

8. Summary and outlook

The field of the theoretical characterization of oxygen defects in TM and RE oxides has reached a state of maturity in recent years. Getting *more* accurate defect formation energies and a more reliable distribution of the excess electrons requires going *beyond* the GGA in DFT, using hybrid approaches, for example. In general that means increasing the computational demands. Thus, the choice of the model of the reduced system may become crucial. Will the widely used periodic models be useful in this respect? Very recent work on the electronic structure of defective TiO_2(110) surfaces using periodic models and hybrid functionals [23,25] indicates that we can expect an increased interest in this type of calculation in the near future. Yet, cluster approaches will still be useful (and less costly computationally). Nonetheless, a universal hybrid functional that includes a *fixed* amount of exact exchange might not necessarily be able to describe the electronic structure (and magnetic properties) of all (different) TM and RE oxides with the same accuracy.

Some theoretical approaches have been applied to reduced TM and RE oxides that produce some improvements over GGA such as DFT + *U* and the self-interaction-corrected DFT (see Refs. [294,299–301]) and are less challenging computationally compared to hybrid methods. These methods do cure GGA shortcomings such as the predicted metallicity of actual insulating (reduced) TM and RE oxides and significantly improve the underestimation of band gaps. Yet, further development is necessary to obtain reliable energies, i.e., the quest for improved functionals is still open.

Once a more accurate description of the surface electronic structure has been reached, the next logical step would be to re-inspect results of surface chemistry studies on TM and RE oxides, e.g., on the binding of selected adsorbates on reduced surfaces and the nature of reaction intermediates on easily reducible oxides. We think that there is room for surprises considering that the surface chemistry of TM and RE oxides is often defect-driven.

Also, the experimental know-how in the field is growing. It is only recently that atomic-resolution imaging using STM has gained the capability to characterize defect structures and defect mobility, and with scanning tunnel spectroscopy new possibilities emerge. Joint efforts are likely to improve our current knowledge of the defects related properties and their influence on the chemical and physical behavior of TM and RE oxides systems.

Acknowledgements

We would like to thank many colleagues, namely, Mónica Calatayud, Alexis Markovits, Javier Fernández Sanz, Andrea Vittadini, Cristiana Di Valentin, Stefano Fabris, Juarez L.F. da Silva, Graeme Watson, Kersti Hermansson, Hannes Jonsson, and David A. Andersson for providing us with further details on their published results as well as preprints. Special thanks to Francesc Illas and Ibério de P.R. Moreira for discussions on electrostatic properties. We thank Cristiana Di Valentin, Jens Döbler, Bjørk Hammer, Annabella Selloni, Javier Fernández Sanz and Yong-Fan Zhang for providing original figures. We also owe thanks to Jens Döbler for many insightful discussions and Gernot Katzer for technical assistance. The Deutsche Forschungsgemeinschaft (Sonderforschungsbereich 546 and Schwerpunktprogramm 1091) is acknowledged for financial support. The calculations were carried out on the IBM p690 system of the Norddeutscher Verbund für Hoch- und Höchstleistungsrechnen (HLRN) and the Bundeshöchstleistungsrechenzentrum in Bayern (HLRB).

References

[1] C.N.R. Rao, B. Raveau, Transition Metal Oxides: Structure, Properties, and Synthesis of Ceramic Oxides, 2nd ed., Wiley-VCH, New York, 1998.
[2] V.E. Henrich, P.A. Cox, The Surface Science of Metal Oxides, Cambridge University Press, Cambridge, 1994.
[3] A. Trovarelli (Ed.), Catalysis by Ceria and Related Materials, in: Catalytic Science Series, vol. 2, Imperial College Press, London, 2002.
[4] N. Tit, Electronic-structure of a single oxygen vacancy in rutile TiO_2, Nuovo Cimento Soc. Ital. Fis. D-Condens. Matter At. Mol. Chem. Phys. Fluids Plasmas Biophys. 15 (1993) 1405.
[5] J. Purton, D.W. Bullett, P.M. Oliver, S.C. Parker, Electronic-structure and atomistic simulations of the ideal and defective surfaces of rutile, Surf. Sci. 336 (1995) 166.
[6] K.D. Schierbaum, W.X. Xu, The electronic structure of intrinsic defects at TiO_2(110) surfaces: An ab initio molecular orbital study, Int. J. Quantum Chem. 57 (1996) 1121.
[7] M. Ramamoorthy, R.D. Kingsmith, D. Vanderbilt, Defects on TiO_2(110) surfaces, Phys. Rev. B 49 (1994) 7709.
[8] W.C. Mackrodt, E.A. Simson, N.M. Harrison, An ab initio Hartree–Fock study of the electron-excess gap states in oxygen-deficient rutile TiO_2, Surf. Sci. 384 (1997) 192.
[9] P.J.D. Lindan, N.M. Harrison, M.J. Gillan, J.A. White, First-principles spin-polarized calculations on the reduced and reconstructed TiO_2(110) surface, Phys. Rev. B 55 (1997) 15919.
[10] P.J.D. Lindan, J. Muscat, S. Bates, N.M. Harrison, M.J. Gillan, Ab initio simulation of molecular processes on oxide surfaces, Faraday Discuss. 106 (1997) 135.
[11] A.T. Paxton, L. Thiên-Nga, Electronic structure of reduced titanium dioxide, Phys. Rev. B 57 (1998) 1579.
[12] T. Bredow, G. Pacchioni, Electronic structure of an isolated oxygen vacancy at the TiO_2(110) surface, Chem. Phys. Lett. 355 (2002) 417.
[13] M. Menetrey, A. Markovits, C. Minot, Reactivity of a reduced metal oxide surface: Hydrogen, water and carbon monoxide adsorption on oxygen defective rutile TiO_2(110), Surf. Sci. 524 (2003) 49.
[14] A. Bouzoubaa, A. Markovits, M. Calatayud, C. Minot, Comparison of the reduction of metal oxide surfaces: TiO_2-anatase, TiO_2-rutile and SnO_2-rutile, Surf. Sci. 583 (2005) 107.
[15] A. Vijay, G. Mills, H. Metiu, Adsorption of gold on stochiometric and reduced rutile TiO_2(110) surfaces, J. Chem. Phys. 118 (2003) 6536.
[16] J. Oviedo, M.A. San Miguel, J.F. Sanz, Oxygen vacancies on TiO_2(110) from first-principles calculations, J. Chem. Phys. 121 (2004) 7427.
[17] X.Y. Wu, A. Selloni, S.K. Nayak, First principles study of CO oxidation on TiO_2(110): The role of surface oxygen vacancies, J. Chem. Phys. 120 (2004) 4512.
[18] M.D. Rasmussen, L.M. Molina, B. Hammer, Adsorption, diffusion and dissociation of molecular oxygen at defected TiO_2(110). A density functional study, J. Chem. Phys. 120 (2004) 988.
[19] X. Wu, A. Selloni, M. Lazzeri, S.K. Nayak, Oxygen vacancy mediated adsorption and reactions of molecular oxygen on the TiO_2(110) surface, Phys. Rev. B 68 (2003) 241402(R).
[20] N. Capron, G. Boureau, Density functional theory study of point defects in the Si–SiO_2 system and in substoichiometric titanium dioxide TiO_{2-x}, Int. J. Quantum Chem. 99 (2004) 677.
[21] S.-G. Wang, X.-D. Wen, D.-B. Cao, Y.-W. Li, J. Wang, H. Jiao, Formation of oxygen vacancies on the TiO_2(110) surfaces, Surf. Sci. 577 (2005) 69.
[22] A. Vittadini, A. Selloni, Small gold clusters on stochiometric and defected TiO_2 anatase (101) and their interaction with CO: A density functional study, J. Chem. Phys. 117 (2002) 353.
[23] Y.-F. Zhang, W. Lin, Y. Li, K. Ding, J. Li, A theoretical study on the electronic structures of TiO_2: Effect of Hartree–Fock exchange, J. Phys. Chem. B 109 (2005) 19270.
[24] Y. Wang, D.J. Doren, First-principles calculations on TiO_2 doped by N, Nd, and vacancy, Solid State Commun. 136 (2005) 186.
[25] C. Di Valentin, G. Pacchioni, A. Selloni, Electronic structure of defect states in hydroxylated and reduced rutile TiO_2(110) surfaces, Phys. Rev. Lett. 97 (2006) 166803.
[26] E. Cho, S. Han, H.-S. Ahn, K.-R. Lee, S.K. Kim, C.S. Hwang, First-principle study of defects in rutile TiO_{2-x}, Phys. Rev. B 73 (2006) 193202.
[27] C. Di Valentin, G. Pacchioni, A. Selloni, Theory of carbon doping of titanium dioxide, Chem. Mater. 17 (2005) 6656.
[28] K. Hameeow, G. Cantele, D. Ninno, F. Trani, G. Iadonisi, Influence of surface and subsurface defects on the behavior of the rutile TiO_2(110) surface, Phys. Status Solidi A 203 (2006) 2219.
[29] A. Hofmann, M.V. Ganduglia-Pirovano, J. Sauer, Calculations for this review, 2006.
[30] A. Eichler, Tetragonal Y-doped zirconia: Structure and ion conductivity, Phys. Rev. B 64 (2001) 174103.
[31] A.S. Foster, V.B. Sulimov, F.L. Gejo, A.L. Shluger, R.M. Nieminen, Structure and electrical levels of point defects in monoclinic zirconia, Phys. Rev. B 64 (2001) 224108.
[32] A.S. Foster, V.B. Sulimov, F.L. Gejo, A.L. Shluger, R.M. Nieminen, Modelling of point defects in monoclinic zirconia, J. Non-Cryst. Solids 303 (2002) 101.
[33] B. Králik, E.K. Chang, S.G. Louie, Structural properties and quasiparticle band structure of zirconia, Phys. Rev. B 57 (1998) 7027.
[34] A.A. Safonov, A.A. Bagatur'yants, A.A. Korkin, Oxygen vacancies in tetragonal ZrO_2: Ab initio embedded cluster calculations, Microelectron. Eng. 69 (2003) 629.
[35] A. Hofmann, S.J. Clark, M. Oppel, I. Hahndorf, Hydrogen adsorption on the tetragonal ZrO_2(101) surface: A theoretical study of an important catalytic reactant, Phys. Chem. Chem. Phys. 4 (2002) 3500.
[36] W. Lambrecht, B. Djafari-Rouhani, J. Vennik, Electronic structure of the vanadyl oxygen vacancy in V_2O_5: Periodic vacancy single layer model, Solid State Commun. 39 (1981) 257.
[37] K. Hermann, M. Witko, R. Druzinic, Electronic properties, structure and adsorption at vanadium oxide: Density functional theory studies, Faraday Discuss. 114 (1999) 53.
[38] K. Hermann, M. Witko, R. Druzinić, R. Tokarz, Oxygen vacancies at oxide surfaces: Ab initio density functional theory studies on vanadium pentoxide, Appl. Phys. A 72 (2001) 429.
[39] R. Druzinić, Ph. D. Thesis, Freie Universität, Berlin, 1999.
[40] J. Sauer, J. Döbler, Structure and reactivity of V_2O_5: Bulk solid, nanosized clusters, species supported on silica and alumina, cluster cations and anions, Dalton Trans. 19 (2004) 3116.
[41] M.V. Ganduglia-Pirovano, J. Sauer, Stability of reduced V_2O_5(001) surfaces, Phys. Rev. B 70 (2004) 045422.

[42] R. Tokarz-Sobieraj, M. Witko, R. Gryboś, Reduction and re-oxidation of molybdena and vanadia: DFT cluster model studies, Catal. Today 99 (2005) 241.
[43] T.X.T. Sayle, S.C. Parker, C.R.A. Catlow, The role of oxygen vacancies on ceria surfaces in the oxidation of carbon-monoxide, Surf. Sci. 316 (1994) 329.
[44] J.C. Conesa, Computer modeling of surfaces and defects on cerium dioxide, Surf. Sci. 339 (1995) 337.
[45] N.V. Skorodumova, S.I. Simak, B.I. Lundqvist, I.A. Abrikosov, B. Johansson, Quantum origin of the oxygen storage capability of ceria, Phys. Rev. Lett. 89 (2002) 166601.
[46] Z. Yang, T.K. Woo, M. Baudin, K. Hermansson, Atomic and electronic structure of unreduced and reduced CeO_2 surfaces: A first-principles study, J. Chem. Phys. 120 (2004) 7741.
[47] Y. Jiang, J.B. Adams, M. van Schilfgaarde, R. Sharma, P.A. Crozier, Theoretical study of environmental dependence of oxygen vacancy formation in CeO_2, Appl. Phys. Lett. 87 (2005) 141917.
[48] S. Fabris, S. de Gironcoli, S. Baroni, G. Vicario, G. Balducci, Taming multiple valency with density functionals: A case study of defective ceria, Phys. Rev. B 71 (2005) 041102(R).
[49] S. Fabris, S. de Gironcoli, S. Baroni, G. Vicario, G. Balducci, Reply to "Comment on 'Taming multiple valency with density functionals: A case study of defective ceria"', Phys. Rev. B 72 (2005) 237102.
[50] S. Fabris, G. Vicario, G. Balducci, S. de Gironcoli, S. Baroni, Electronic and atomistic structures of clean and reduced ceria surfaces, J. Phys. Chem. B 109 (2005) 22860.
[51] M. Nolan, S. Grigoleit, D.C. Sayle, S.C. Parker, G.W. Watson, Density functional theory studies of the structure and electronic structure of pure and defective low index surfaces of ceria, Surf. Sci. 576 (2005) 217.
[52] M. Nolan, S.C. Parker, G.W. Watson, The electronic structure of oxygen vacancy defects at the low index surfaces of ceria, Surf. Sci. 595 (2005) 223.
[53] M. Nolan, J.E. Fearon, G.W. Watson, Oxygen vacancy formation and migration in ceria, Solid State Ion. 177 (2006) 3069.
[54] D.A. Andersson, S.I. Simak, B. Johansson, I.A. Abrikosov, N.V. Skorodumova, Modelling of CeO_2, Ce_2O_3, and CeO_{2-x} in the LDA + U formalism, Phys. Rev. B 75 (2007) 035109.
[55] J.P. Perdew, J.A. Chevary, S.H. Vosko, K.A. Jackson, M.R. Pederson, D.J. Singh, C. Fiolhais, Atoms, molecules, solids and surfaces: Applications of the generalized gradient approximation for exchange and correlation, Phys. Rev. B 46 (11) (1992) 6671.
[56] J.P. Perdew, K. Burke, M. Ernzerhof, Generalized gradient approximation made simple, Phys. Rev. Lett. 77 (1996) 3865.
[57] B. Hammer, L.B. Hansen, J. Nørskov, Improved adsorption energetics within density-functional theory using revised Perdew–Burke–Ernzerhof functionals, Phys. Rev. B 59 (1999) 7413.
[58] A.D. Becke, Density-functional thermochemistry. III. The role of exact exchange, J. Chem. Phys. 98 (1983) 5648.
[59] C. Lee, W. Yang, R.G. Parr, Development of the Colle–Salvetti correlation-energy formula into a functional of the electron density, Phys. Rev. B 37 (1988) 785.
[60] V.I. Anisimov, J. Zaanen, O.K. Andersen, Band theory and Mott insulators: Hubbard U instead of Stoner I, Phys. Rev. B 44 (1991) 943.
[61] V.I. Anisimov, I.V. Solovyev, M.A. Korotin, M.T. Czyzyk, G.A. Sawatzky, Density-functional theory and NiO photoemission spectra, Phys. Rev. B 48 (1993) 16929.
[62] A.I. Liechtenstein, V.I. Anisimov, J. Zaanen, Density-functional theory and strong interactions: Orbital ordering in Mott–Hubbard insulators, Phys. Rev. B 52 (1995) R5467.
[63] V.I. Anisimov, F. Aryasetiawan, A.I. Lichtenstein, First-principles calculations of the electronic structure and spectra of strongly correlated systems: The LDA + U method, J. Phys.: Condens. Matter 9 (1997) 767.
[64] P. Mori-Sánchez, J.M. Recio, B. Silvi, C. Sousa, A.M. Pendás, V. Luaña, F. Illas, Rigorous characterization of oxygen vacancies in ionic oxides, Phys. Rev. B 66 (2002) 075103.
[65] G. Pacchioni, Ab initio theory of point defects in oxide materials: Structure, properties, chemical reactivity, Solid State Sci. 2 (2000) 161.
[66] G. Pacchioni, Quantum chemistry of oxide surfaces: From CO chemisorption to the identification of the structure and nature of point defects on MgO, Surf. Rev. Lett. 7 (2000) 277.
[67] G. Pacchioni, Theory of point defects on ionic oxides, in: The Chemical Physics of Solid Surfaces — Oxide Surfaces, vol. 9, Elsevier, Amsterdam, 2001, p. 94.
[68] M. Menetrey, A. Markovits, C. Minot, G. Pacchioni, Formation of Schottky defects at the surface of MgO, TiO_2, and SnO_2: A comparative density functional theoretical study, J. Phys. Chem. B 108 (2004) 12858.
[69] J. Carrasco, N. Lopez, F. Illas, First principles analysis of the stability and difussion of oxygen vacancies in metal oxides, Phys. Rev. Lett. 93 (2004) 225502.
[70] J. Carrasco, N. Lopez, F. Illas, On the convergence of isolated neutral oxygen vacancy and divacancy properties in metal oxides using supercell models, J. Chem. Phys. 122 (2005) 224705.
[71] A.L. Shluger, A.S. Foster, J. Gavartin, P.V. Sushko, Defects in wide-gap oxides: Computer modelling and challenges, in: Nano and Giga Challenges in Microelectronics, Elsevier, Amsterdam, 2003, p. 151.
[72] F. Illas, R.L. Martin, Magnetic coupling in ionic solids studied by density functional theory, J. Chem. Phys. 108 (1998) 2519.
[73] T. Bredow, A.R. Gerson, Effect of exchange and correlation on bulk properties of MgO, NiO, and CoO, Phys. Rev. B 61 (2000) 5194.
[74] J. Muscat, A. Wander, N.M. Harrison, On the prediction of band gaps from hybrid functional theory, Chem. Phys. Lett. 342 (2001) 397.
[75] K. Kudin, G. Scuseria, R. Martin, Hybrid density-functional theory and the insulating gap of UO_2, Phys. Rev. Lett. 89 (2002) 266402.
[76] I. de P.R. Moreira, F. Illas, R.L. Martin, Effect of Fock exchange on the electronic structure and magnetic coupling in NiO, Phys. Rev. B 65 (2002) 155102.
[77] P.J. Hay, R.L. Martin, J. Uddin, G.E. Scuseria, Theoretical study of CeO_2 and Ce_2O_3 using a screened hybrid density functional, J. Chem. Phys. 125 (2006) 034712.
[78] F. Gygi, A. Baldereschi, Self-consistent Hartree-Fock and screened-exchange calculations in solids — application to silicon, Phys. Rev. B 34 (1986) 4405.
[79] S. Chawla, G.A. Voth, Exact exchange in ab initio molecular dynamics: An efficient plane-wave based algorithm, J. Chem. Phys. 108 (1998) 4697.
[80] J. Heyd, G.E. Scuseria, M. Ernzerhof, Hybrid functionals based on a screened Coulomb potential, J. Chem. Phys. 118 (2003) 8207.
[81] J. Heyd, G.E. Scuseria, Assessment and validation of a screened Coulomb hybrid density functional, J. Chem. Phys. 120 (2004) 7274.
[82] J. Heyd, G.E. Scuseria, Erratum: "Hybrid functionals based on a screened Coulomb potential" [J. Chem. Phys. 118 (2003) 8207], J. Chem. Phys. 124 (2006) 219906 (Erratum).
[83] J.P. Perdew, M. Ernzerhof, S. Burke, Rationale for mixing exact exchange with density functional approximations, J. Chem. Phys. 105 (1996) 9982.
[84] C. Adamo, V. Barone, Toward reliable density functional methods without adjustable parameters: The PBE0 model, J. Chem. Phys. 110 (1999) 6158.
[85] M. Ernzerhof, G.E. Scuseria, Assessment of the Perdew–Burke–Ernzerhof exchange–correlation functional, J. Chem. Phys. 110 (1999) 5029.
[86] J. Paier, R. Hirsch, M. Marsman, G. Kresse, The Perdew–Burke–Ernzerhof exchange–correlation functional applied to the G2-1 test set using a plane-wave basis set, J. Chem. Phys. 122 (2005) 234102.
[87] J. Paier, M. Marsman, K. Hummer, G. Kresse, I.C. Gerber, J.G. Angyan, Screened hybrid density functionals applied to solids, J. Chem. Phys. 124 (2006) 154709.
[88] T. Todorova, A.P. Seitsonen, J. Hutter, I.F.W. Kuo, C.J. Mundy, Molecular dynamics simulation of liquid water: Hybrid density functionals, J. Phys. Chem. B 110 (2006) 3685.
[89] J.L.F. da Silva, M.V. Ganduglia-Pirovano, J. Sauer, V. Bayer, G. Kresse, A hybrid functionals applied to rare earth oxides: The example of ceria, Phys. Rev. B 75 (2007) 045121.

[90] B. Herschend, M. Baudin, K. Hermansson, Electronic structure of the $CeO_2(110)$ surface oxygen vacancy, Surf. Sci. 599 (2005) 173.
[91] A. Svane, O. Gunnarsson, Transition-metal oxides in the self-interaction corrected density-functional formalism, Phys. Rev. Lett. 65 (1990) 1148.
[92] J. Hubbard, Electron correlations in narrow energy bands, Proc. R. Soc. Lond., Ser. A 276 (1963) 238.
[93] J. Hubbard, Electron correlations in narrow energy bands. II. The degenerate band case, Proc. R. Soc. Lond., Ser. A 277 (1964) 237.
[94] J. Hubbard, Electron correlations in narrow energy bands. III. An improved solution, Proc. R. Soc. Lond., Ser. A 281 (1964) 401.
[95] S.L. Dudarev, G.A. Botton, S.Y. Savrasov, C.J. Humphreys, A.P. Sutton, Electron-energy-loss spectra and the structural stability of nickel oxide: An LSDA + U study, Phys. Rev. B 57 (1998) 1505.
[96] W.E. Pickett, S.C. Erwin, E.C. Ethridge, Reformulation of the LDA + U method for a local-orbital basis, Phys. Rev. B 58 (1998) 1201.
[97] O. Bengone, M. Alouani, P. Blöchl, J. Hugel, Implementation of the projector augmented-wave LDA + U method: Application to the electronic structure of NiO, Phys. Rev. B 62 (2000) 16392.
[98] G.K.H. Madsen, P. Novák, Charge order in magnetite. An LDA + U study, Europhys. Lett. 69 (2005) 777.
[99] M. Cococcioni, S. de Gironcoli, Linear response approach to the calculation of the effective interaction parameters in the LDA + U method, Phys. Rev. B 71 (2005) 035105.
[100] D. Vanderbilt, Soft self-consistent pseudopotentials in a generalized eigenvalue formalism, Phys. Rev. B 41 (1990) 7892.
[101] G. Kresse, J. Hafner, Norm-conserving and ultrasoft pseudopotentials for first-row and transition elements, J. Phys.: Condens. Matter 6 (1994) 8245.
[102] U. Diebold, The surface science of titanium dioxide, Surf. Sci. Rep. 48 (2003) 53.
[103] L. Kavan, M. Grätzel, S.E. Gilbert, C. Klemenz, H.J. Scheel, Electrochemical and photoelectrochemical investigation of single-crystal anatase, J. Amer. Chem. Soc. 118 (1996) 6716.
[104] J. Muscat, V. Swamy, N.M. Harrison, First-principles calculations of the phase stability of TiO_2, Phys. Rev. B 65 (2002) 224112.
[105] A.S. Barnard, P. Zapol, Effect of particle morphology and surface hydrogenation on the phase stability of TiO_2, Phys. Rev. B 70 (2004) 235403.
[106] M. Ramamoorthy, D. Vanderbilt, R.D. Kingsmith, First principles calculations of the energetics of stoichiometric TiO_2 surfaces, Phys. Rev. B 49 (1994) 16721.
[107] M. Lazzeri, A. Vittadini, A. Selloni, Structure and energetics of stochiometric TiO_2 anatase surfaces, Phys. Rev. B 63 (2001) 155409.
[108] U. Diebold, N. Ruzycki, G.S. Herman, A. Selloni, One step towards bridging the materials gap: Surface studies of TiO_2 anatase, Catal. Today 85 (2003) 93.
[109] G.V. Samsonov, The Oxide Handbook, 2nd ed., IFI/Plenum Press, New York, 1982.
[110] S. Andersson, B. Collen, U. Kuylenstierna, A. Magnéli, Phase analysis studies on the titanium–oxygen system, Acta Chem. Scand. 11 (1957) 1641.
[111] J.B. Goodenough, Metallic oxides, in: H. Reiss (Ed.), Progress in Solid State Chemistry, vol. 5, Pergamon, New York, 1972, p. 145.
[112] T.G. Gray, C.C. McCain, N.G. Masse, Defect structure and catalysis in the TiO_2 system (semi-conducting and magnetic properties), J. Phys. Chem. 63 (1959) 472.
[113] U. Diebold, M. Li, O. Dulub, E.L.D. Hebenstreit, The relationship between bulk and surface properties of rutile $TiO_2(110)$, Surf. Rev. Lett. 7 (2000) 613.
[114] R.D. Iyengar, M. Codell, J. Tara, J. Turkevich, Electron spin resonance studies of the surface chemistry of rutile, J. Amer. Chem. Soc. 88 (1966) 5055.
[115] R.A. Bennet, S. Poulston, P. Stone, M. Bowker, STM and LEED observations of the surface structure of $TiO_2(110)$ following crystallographic shear plane formation, Phys. Rev. B 59 (1999) 10341.
[116] D.C. Hurum, A.G. Agrios, K.A. Gray, T. Rajh, M.C. Thurnauer, Explaining the enhanced photocatalytic activity of Degussa P25 mixed-phase TiO_2 using EPR, J. Phys. Chem. B 107 (2003) 4545.
[117] T. Berger, M. Sterrer, O. Diwald, E. Knözinger, D. Panayotov, T.L. Thompson, J.T. Yates Jr., Light-induced charged separation in anatase TiO_2 particles, J. Phys. Chem. B 109 (2005) 6061.
[118] T.L. Thompson, J.T. Yates, TiO_2-based photocatalysis: Surface defects, oxygen and charge transfer, Topics in Catal. 35 (2005) 197.
[119] J.M. Pan, B.L. Maschhoff, U. Diebold, T.E. Madey, Interaction of water, oxygen, and hydrogen with $TiO_2(110)$ surfaces having different defect densities, J. Vac. Sci. Technol. A 10 (1992) 2470.
[120] M.A. Henderson, An HREELS and TPD study of water on $TiO_2(110)$: The extent of molecular versus dissociative adsorption, Surf. Sci. 355 (1996) 151.
[121] R. Schaub, E. Wahlström, A. Rønnau, E. Lægsgaard, I. Stensgaard, F. Besenbacher, Oxygen-mediated diffusion of oxygen vacancies on the $TiO_2(110)$ surface, Science 299 (2003) 377.
[122] E. Wahlström, E.K. Vestergaard, R. Schaub, A. Rønnau, M. Vestergaard, E. Lægsgaard, I. Stensgaard, F. Besenbacher, Electron transfer-induced dynamics of oxygen molecules on the $TiO_2(110)$ surface, Science 303 (2004) 511.
[123] R. Schaub, Oxygen-mediated diffusion of oxygen vacancies on the $TiO_2(110)$ surface (vol. 311, p. 377 (2003)), Science 314 (2006) 925.
[124] S. Wendt, J. Matthiesen, R. Schaub, E.K. Vestergaard, E. Lægsgaard, F. Besenbacher, B. Hammer, Formation and splitting of paired hydroxyl groups on reduced $TiO_2(110)$, Phys. Rev. Lett. 96 (2006) 066107.
[125] S. Wendt, R. Schaub, J. Matthiesen, E.K. Vestergaard, E. Wahlström, M.D. Rasmussen, P. Thostrup, L.M. Molina, E. Lægsgaard, I. Stensgaard, B. Hammer, F. Besenbacher, Oxygen vacancies on $TiO_2(110)$ and their interaction with H_2O and O_2: A combined high-resolution STM and DFT study, Surf. Sci. 598 (2005) 226.
[126] M. Harutaa, Size- and support-dependency in the catalysis of gold, Catal. Today 36 (1997) 153.
[127] M. Valden, X. Lai, D.W. Goodman, Onset of catalytic activity of gold clusters on titania with the appearance of nonmetallic properties, Sience 281 (1998) 1647.
[128] C.T. Campbell, The active site in nanoparticle gold catalysis, Sience 306 (2004) 234.
[129] M.S. Chen, D.W. Goodman, The structure of catalytically active gold on titania, Sience 306 (2004) 252.
[130] U. Diebold, Dispersed Au atoms, supported on $TiO_2(110)$, Surf. Sci. 578 (2005) 1.
[131] V.E. Henrich, R.L. Kurtz, Surface electronic structure of TiO_2: Atomic geometry, ligand coordination, and the effect of adsorbed hydrogen, Phys. Rev. B 23 (1981) 6280.
[132] Y. Aiura, Y. Nishihara, Y. Haruyama, T. Komeda, S. Kodaira, Y. Sakisaka, T. Maruyama, H. Kato, Effects of surface oxygen vacancies on electronic states of $TiO_2(110)$, $TiO_2(001)$ and $SrTiO_3(001)$ surfaces, Physica B 194–196 (1994) 1215.
[133] Z. Zhang, S.-P. Jeng, V.E. Henrich, Cation–ligand hybridization for stoichiometric and reduced $TiO_2(110)$ surfaces determined by resonant photoemission, Phys. Rev. B 43 (1991) 12004.
[134] R. Heise, R. Courths, S. Witzel, Valence band densities-of-states of $TiO_2(110)$ from resonant photoemission and photoelectron diffraction, Solid State Commun. 84 (1992) 599.
[135] J. Nerlov, Q. Ge, P.J. Møller, Resonant photoemission from $TiO_2(110)$ surfaces: Implications on surface bonding and hybridization, Surf. Sci. 348 (1996) 28.
[136] A.G. Thomas, W.R. Flavell, A.R. Kumarasinghe, A.K. Mallick, D. Tsoutsou, G.C. Smith, R. Stockbauer, S. Patel, M. Grätzel, R. Hengerer, Resonant photoemission of anatase $TiO_2(101)$ and (001) single crystals, Phys. Rev. B 67 (2003) 035110.
[137] R.L. Kurtz, R. Stock-Bauer, T.E. Msdey, E. Román, J.L.D. Segovia, Synchrotron radiation studies of H_2O adsorption on $TiO_2(110)$, Surf. Sci. 218 (1989) 178.
[138] S. Krischok, J. Günster, D.W. Goodman, O. Höfft, V. Kempter, MIES and UPS(HeI) studies on reduced $TiO_2(110)$, Surf. Interface Anal. 37 (2005) 77.
[139] V.E. Henrich, G. Dresselhaus, H.J. Ziegler, Observation of two-dimensional phases associated with defect states on the surface of TiO_2, Phys. Rev. Lett. 36 (1976) 1335.

[140] H.R. Sadeghi, V.E. Henrich, Electronic interactions in the rhodium/TiO_2 system, J. Catal. 109 (1988) 1.
[141] M.A. Henderson, W.S. Epling, C.H.F. Peden, C.L. Perkins, Insights into photoexcited electron scavenging processes on TiO_2 obtained from studies of the reaction of O_2 with OH groups adsorbed at electronic defects on TiO_2(110), J. Phys. Chem. B 107 (2003) 534.
[142] R. Dovesi, V.R. Saunders, C. Roetti, M. Causà, N.M. Harrison, R. Orlando, E. Aprà, CRYSTAL95, 1995.
[143] C.J. Howard, T.M. Sabine, F. Dickson, Structural and thermal parameters for rutile and anatase, Acta Cryst. B47 (1991) 462.
[144] D.M. Ceperley, B.J. Alder, Ground state of the electron gas by a stochastic method, Phys. Rev. Lett. 45 (1980) 566.
[145] A. Zunger, J.P. Perdew, G.L. Oliver, A self-interaction corrected approach to many-electron systems: Beyond the local spin density approximation, Solid State Commun. 32 (1980) 933.
[146] J.P. Perdew, M. Levy, Physical content of the exact Kohn-Sham orbital energies: Band gaps and derivative discontinuities, Phys. Rev. Lett. 51 (1983) 1884.
[147] K.M. Glassford, J.R. Chelikowsky, Structural and electronic properties of titanium dioxide, Phys. Rev. B 46 (1992) 1284.
[148] S.-D. Mo, W.Y. Ching, Electronic and optical properties of three phases of titanium dioxide: Rutile, anatase, and brookite, Phys. Rev. B 51 (1995) 13023.
[149] M.-Y. Kuo, C.-L. Chen, C.-Y. Hua, H.-C. Yang, P. Shen, Density functional theory calculations of dense TiO_2 polymorphs: Implication for visible-light-responsive photocatalysts, J. Phys. Chem. B 109 (2005) 8693.
[150] T. Bredow, L. Giordano, F. Cinquini, G. Pacchioni, Electronic properties of rutile TiO_2 ultrathin films: Odd-even oscillations with the number of layers, Phys. Rev. B 70 (2004) 035419.
[151] B. Silvi, N. Fourati, R. Nada, C.R.A. Catlow, Pseudopotential periodic Hartree–Fock study of rutile TiO_2, J. Phys. Chem. Solids 52 (1991) 1005.
[152] M. Methfessel, Elastic constants and phonon frequencies of Si calculated by a fast full-potential linear-muffin-tin-orbital method, Phys. Rev. B 38 (1988) 1537.
[153] M. Methfessel, C.O. Rodriguez, O.K. Andersen, Fast full-potential calculations with a converged basis of atom-centered linear muffin-tin orbitals: Structural and dynamic properties of silicon, Phys. Rev. B 40 (1989) 2009.
[154] U. von Barth, L. Hedin, A local exchange–correlation potential for the spin polarized case. I, J. Phys. C 5 (1972) 1629.
[155] V.L. Moruzzi, J.F. Janak, A.R. Williams, Calculated Electronic Properties of Metals, Pergamon, New York, 1978.
[156] G. Kresse, J. Furthmüller, Efficiency of ab initio total energy calculations for metals and semiconductors using a plane-wave basis set, Comput. Mater. Sci. 6 (1996) 15.
[157] URL: http://cms.mpi.univie.ac.at/vasp/.
[158] R. Car, M. Parrinello, Unified approach for molecular dynamics and density-functional theory, Phys. Rev. Lett. 55 (2) (1985) 2471.
[159] URL: http://www.cpmd.org/.
[160] S.P. Bates, G. Kresse, M.J. Gillan, A systematic study of the surface energetics and structure of TiO_2(110) by first-principles calculations, Surf. Sci. 385 (1997) 386.
[161] K.J. Hameeuw, G. Cantele, D. Ninno, F. Trani, G. Iadonisi, The rutile TiO_2(110) surface: Obtaining converged structural properties from first-priciples calculations, J. Chem. Phys. 124 (2006) 024708.
[162] G. Herzberg, Molecular Spectra and Molecular Structure. I. Spectra of Diatomic Molecules, 2nd ed., Robert E. Krieger Publishing Co., Inc., 1989.
[163] J. Woning, R.A. van Santen, Electrostatic potential calculations on crystalline TiO_2: The surface reducibility of rutile and anatase, Chem. Phys. Lett. 101 (1983) 541.
[164] L. Kleinman, D.M. Bylander, Efficacious form for model pseudopotentials, Phys. Rev. Lett. 48 (1982) 1425.
[165] P. Kofstad, Thermogravimetric studies of the defect structure of in rutile TiO_2, J. Phys. Chem. Solids 23 (1962) 1579.
[166] F. Furche, J.P. Perdew, The performance of semilocal and hybrid density functionals in 3d transition-metal chemistry, J. Chem. Phys. 124 (2006) 044103.
[167] A.H. Heuer, L.W. Hobbs. (Eds.), Science and Technology of Zirconia I, in: Advances in Ceramics, vol. 3, The American Ceramic Society, Westerville, OH, 1981.
[168] A.H. Heuer, L.W. Hobbs. (Eds.), Science and Technology of Zirconia II, in: Advances in Ceramics, vol. 12, The American Ceramic Society, Westerville, OH, 1984.
[169] A.I. Kingon, J.-P. Maria, S.K. Streiffer, Alternative dielectrics to silicon dioxide for memory and logic deviced, Nature 406 (2000) 1032.
[170] S. Chandra, Superionic Solids: Principles and Applications, North-Holland, Amsterdam, 1981.
[171] F.J. Rohr, Solid electrolytes, in: Material Science Series, Academic, New York, 1978, p. 431.
[172] A. Dittmar, H. Kosslick, D. Herein, Microwave plasma assisted preparation of disperse chromium oxide supported catalysts influence of the microwave plasma treatment on the properties of the supports, Catal. Today 89 (2004) 169.
[173] J.D. McCullough, K.N. Trueblood, The crystal structure of monoclinic ZrO_2, Acta Cryst. 12 (1959) 507.
[174] D.K. Smith, H.W. Newkirk, The crystal structure of baddeleyite (monoclinic ZrO_2) and its relation to the polymorphism of ZrO_2, Acta Cryst. 18 (1965) 983.
[175] G. Teufer, The crystal structure of tetragonal ZrO_2, Acta Cryst. 15 (1962) 1187.
[176] D.K. Smith, C.F. Cline, Verification of existence of cubic zirconia at high temperature, J. Amer. Chem. Soc. 45 (1962) 249.
[177] D.W. McComb, Bonding and electronic structure in zirconia pseudopolymorphs investigated by electron energy-loss spectroscopy, Phys. Rev. B 54 (1996) 7094.
[178] R.H. French, S.J. Glass, F.S. Ohuchi, Y.-N. Xu, W.Y. Ching, Experimental and theoretical determination of the electronic structure and optical properties of three phases of ZrO_2, Phys. Rev. B 49 (1994) 5133.
[179] C. Morterra, G. Cerrato, L. Ferroni, A. Negro, L. Montanaro, Surface characterization of tetragonal ZrO_2, Appl. Surf. Sci. 65–66 (1993) 257.
[180] A. Christensen, E.A. Carter, First-principles study of the surfaces of zirconia, Phys. Rev. B 58 (1998) 8050.
[181] F. Haase, J. Sauer, The surface structure of sulfated zirconia, J. Amer. Chem. Soc. 120 (1998) 13503.
[182] A. Eichler, G. Kresse, First-principles calculations for the surface termination of pure and yttria-doped zirconia surfaces, Phys. Rev. B 69 (2004) 045402.
[183] R. Ben-Michael, D.S. Tannhauser, J. Genossar, ESR centers in reduced stabilized zirconia, Phys. Rev. B 43 (1991) 7395.
[184] V.R. PaiVernecker, A.N. Patelin, F.J. Crowne, D.C. Nagle, Color-center-induced band-gap shift in yttria-stabilized zirconia, Phys. Rev. B 40 (1989) 8555.
[185] R.I. Merino, V.M. Orera, E.E. Lomonoya, S.K. Batygov, Paramagnetic electron traps in reduced stabilized zirconia, Phys. Rev. B 52 (1995) 6150.
[186] C.B. Azzoni, A. Paleari, Effects of yttria concentration on the EPR signal in X-Ray-irradiated yttria-stabilized zirconia, Phys. Rev. B 40 (1989) 9333.
[187] V.M. Orera, R.I. Merino, Y. Chen, R. Cases, P.J. Alonso, Intrinsic electron and hole defects in stabilized zirconia single crystals, Phys. Rev. B 42 (1990) 9782.
[188] J.-M. Constantini, F. Beuneu, D. Gourier, C. Trautmanm, G. Calas, M. Toulemonde, Colour-centre production in yttria-stabilized zirconia by swift charged particle irradiation, J. Phys.: Condens. Matter 16 (2004) 3957.
[189] N. Mommer, T. Lee, J.A. Gardner, W.E. Evenson, Oxygen vacancy trapping in tetragonal ZrO_2 studied by In–111/Cd perturbed angular correlation, Phys. Rev. B 61 (2000) 162.
[190] E. Karapetrova, R. Platzer, J.A. Gardner, E. Torne, J.A. Sommers, W.E. Evenson, Oxygen vacancies in pure tetragonal zirconia powders: Dependence on the presence of chlorine during processing, J. Amer. Ceram. Soc. 84 (2001) 65.

[191] J.M. Sanz, A.R. Gonzalez-Elipe, A. Fernandez, D. Leinen, L. Galan, A. Stampfl, A.M. Bradshaw, A resonant photoemission study of the ZrO_2 valence band, Surf. Sci. 307 (1994) 848.
[192] C. Morant, J.M. Sanz, L. Galan, Ar-ion bombardment effects on ZrO_2 surfaces, Phys. Rev. B 45 (1992) 1391.
[193] G. Stapper, M. Bernasconi, N. Nicoloso, M. Parrinello, Ab initio study of structural and electronic properties of yttria-stabilized cubic zirconia, Phys. Rev. B 59 (1999) 797.
[194] A. Bogicevic, C. Wolverton, G.M. Crosbie, E.B. Stechel, Defect ordering in aliovalently doped cubic zirconia from first principles, Phys. Rev. B 6401 (2001) 014106.
[195] A. Bogicevic, C. Wolverton, Elastic reversal of electrostatically driven defect ordering in stabilized zirconia, Europhys. Lett. 56 (2001) 393.
[196] A. Bogicevic, C. Wolverton, Nature and strength of defect interactions in cubic stabilized zirconia, Phys. Rev. B 67 (2003) 024106.
[197] T. Tojo, H. Kawaji, T. Atake, Molecular dynamics study on lattice vibration and heat capacity of yttria-stabilized zirconia, Solid State Ion. 118 (1999) 349.
[198] S. Ostanin, E. Salamatov, Effect of point defects on heat capacity of yttria-stabilized zirconia, Phys. Rev. B 68 (2003) 172106.
[199] M.S. Khan, M.S. Islam, D.R. Bates, Cation doping and oxygen diffusion in zirconia: A combined atomistic simulation and molecular dynamics study, J. Mater. Chem. 8 (1998) 2299.
[200] M. Kilo, C. Argirusis, G. Borchardt, R.A. Jackson, Oxygen diffusion in yttria stabilised zirconia — experimental results and molecular dynamics calculations, Phys. Chem. Chem. Phys. 5 (2003) 2219.
[201] M. Kilo, R.A. Jackson, G. Borchardt, Computer modelling of ion migration in zirconia, Philos. Mag. 83 (2003) 3309.
[202] G.A. Ol'khovic, I.I. Naumov, O.I. Velikokhatnyi, Band structure of cubic ZrO_2 containing oxygen vacancies and calcium ions, J. Phys.: Condens. Matter 7 (1995) 1273.
[203] P. Aldebert, J.P. Traverse, Structure and ionic mobility of zirconia at high-temperature, J. Amer. Ceram. Soc. 68 (1985) 34.
[204] J.E. Wertz, J.W. Orton, R. Auzins, Electron spin resonance studies of radiation effects in inorganic solids, Discuss. Faraday Soc. 31 (1961) 140.
[205] G. Jomard, T. Petit, A. Pasturel, L. Magaud, G. Kresse, J. Hafner, First-principles calculations to describe zirconia pseudopolymorphs, Phys. Rev. B 59 (1999) 4044.
[206] L. Hedin, S. Lundquist, in: F. Seitz, D. Turnbull, H. Ehrenreich (Eds.), Solid State Physics, vol. 23, Academic Press, New York, 1969, p. 1.
[207] M.S. Hybertsen, S.G. Louie, Electron correlation in semiconductors and insulators: Band gaps and quasiparticle energies, Phys. Rev. B 34 (1986) 5390.
[208] J. Robertson, K. Xiong, S.J. Clark, Band gaps and defect levels in functional oxides, Thin Solid Films (2006) 1.
[209] L. Giordano, C.D. Valentin, J. Goniakowski, G. Pacchioni, Nucleation of Pd dimers at defect sites of the MgO(100) surface, Phys. Rev. Lett. 92 (2004) 096105.
[210] P.A. Cox, Transitition Metal Oxides: An Introduction to their Electronic Structure and Properties, Clarendon Press, Oxford, 1992.
[211] B.M. Weckhuysen, D.E. Keller, Chemistry, spectroscopy and the role of supported vanadium oxides in heterogeneous catalysis, Catal. Today 78 (2003) 25. And references therein.
[212] N. Kenny, C.R. Kannerwurf, D.H. Whitmore, Optical absorption coefficient of vanadium pentoxide single crystals, J. Phys. Chem. Solids 27 (1966) 1237.
[213] Z. Bodó, I. Hevesi, Optical absorption near the absorption edge in V_2O_5 single crystals, Phys. Status Solidi 20 (1967) K45.
[214] R. Enjalbert, J. Galy, A refinement of the structure of V_2O_5, Acta Cryst. C42 (1986) 1467.
[215] P. Mars, D.W. van Krevelen, Oxidation carried out by means of vanadium oxide catalysts, Spec. Suppl. Chem. Eng. Sci. 3 (1954) 41.
[216] K. Chen, A. Khodakov, J. Yang, A.T. Bell, E. Iglesia, Isotopic tracer and kinetic studies of oxidative dehydrogenation pathways on vanadium oxide catalysts, J. Catal. 186 (1999) 325.
[217] K. Chen, E. Iglesia, A.T. Bell, Kinetic isotopic effects in oxidative dehydrogenation of propane on vanadium oxide catalysts, J. Catal. 192 (2000) 197.
[218] L. Fiermans, P. Clauws, W. Lambrecht, L. Vandenbroucke, J. Vennik, Single crystal V_2O_5 and lower oxides a survey of their electronic, optical, structural and surface properties, Phys. Status Solidi A 59 (1980) 485.
[219] Z. Zhang, V.E. Henrich, Surface electronic structure of $V_2O_5(001)$: Defect states and chemisorption, Surf. Sci. 321 (1994) 133.
[220] B. Tepper, B. Richter, A.-C. Dupuis, H. Kuhlenbeck, C. Hucho, P. Schilbe, M.A. bin Yarmo, H.-J. Freund, Adsorption of molecular and atomic hydrogen on vacuum cleaved $V_2O_5(001)$, Surf. Sci. (2002) 64.
[221] Q.H. Wu, A. Thissen, W. Jaegermann, M.L. Liu, Photoelectron spectroscopy study of oxygen vacancy on vanadium oxides surface, Appl. Surf. Sci. 236 (2004) 473.
[222] L. Fiermans, J. Vennik, LEED study of the vanadium pentoxide (010) surface, Surf. Sci. 9 (1968) 187.
[223] L. Fiermans, J. Vennik, Particular LEED features on the $V_2O_5(010)$ surface and their relation to the LEED beam induced transition $V_2O_5 \rightarrow V_6O_{13}$, Surf. Sci. 18 (1969) 317.
[224] M.N. Colpaert, P. Clauws, L. Fiermans, J. Vennik, Thermal and low energy electron bombardment induced oxygen loss of V_2O_5 single crystals: Transition into V_6O_{13}, Surf. Sci. 36 (1973) 513.
[225] R.A. Goschke, K. Vey, M. Maier, U. Walter, E. Goering, M. Klemm, S. Horn, Tip induced changes of atomic scale images of the vanadium pentoxide surface, Surf. Sci. 348 (1996) 305.
[226] K. Devriendt, H. Poelman, L. Fiermans, Thermal reduction of vanadium pentoxide: An XPD study, Surf. Sci. (1999) 734.
[227] R.-P. Blum, C. Hucho, H. Niehus, S. Shaikhutdinov, H.-J. Freund, Surface metal–insulator transitions of a vanadium pentoxide (001) single crystal, unpublished.
[228] R.L. Smith, W. Lu, G.S. Rohrer, The observation of oxygen disorder on the $V_2O_5(001)$ surface using scanning tunneling microscopy, Surf. Sci. 322 (1995) 293.
[229] K. Hermann, private communication.
[230] P. Kofstad, Nonstoichiometry, Diffusion, and Electrical Conductivity in Binary Metal Oxides, John Wiley & Sons, Inc., New York, 1972.
[231] M. Sahibzada, B.C.H. Steele, K. Zheng, R.A. Rudkin, I.S. Metcalfe, Development of solid oxide fuel cells based on a $Ce(Gd)O_{2-x}$ electrolyte film for intermediate temperature operation ceria-based solid electrolytes, Catal. Today 38 (1997) 459.
[232] T. Hibino, A. Hashimoto, T. Inoue, J.-I. Tokuno, S.-I. Yoshida, M. Sano, A low-operating-temperature solid oxide fuel cell in hydrocarbon–air mixtures, Science 288 (2000) 2031.
[233] S. Park, J.M. Vohs, R.J. Gorte, Direct oxidation of hydrocarbons in a solid-oxide fuel cell, Nature 404 (2000) 265.
[234] Q. Fu, H. Saltsburg, M. Flytzani-Stephanopoulos, Active nonmetallic Au and Pt species on ceria-based water–gas shift catalysts, Sience 301 (2003) 935.
[235] G.A. Deluga, J.R. Salge, L.D. Schmidt, X.E. Verykios, Renewable hydrogen from ethanol by autothermal reforming, Science 303 (2004) 993.
[236] L. Eyring, in: K.A. Gschneider, L. Eyring, M.B. Maple (Eds.), Handbook on the Physics and Chemistry of Rare Earths, vol. 3, North Holland, Amsterdam, 1979 (Chapter 27).
[237] L. Gerward, J.S. Olsen, L. Petit, G. Vaitheeswaran, K. V., A. Svane, Bulk modulus of CeO_2 and PrO_2—An experimental and theoretical study, J. Alloys Comp. 400 (2005) 56.
[238] N.V. Skorodumova, M. Baudin, K. Hermansson, Surface properties of CeO_2 from first principles, Phys. Rev. B 69 (2004) 075401.
[239] Y. Jiang, J.B. Adams, M. van Schilfgaarde, Density functional calculation of CeO_2 surfaces and prediction of effects of oxygen partial pressure and temperature on stabilities, J. Chem. Phys. 123 (2005) 064701.
[240] H. Nörenberg, G.A.D. Briggs, Defect formation on $CeO_2(111)$ surfaces after annealing studied by STM, Surf. Sci. 424 (1999) L352.
[241] A. Siokou, R.M. Nix, Interaction of methanol with well-defined ceria surfaces: Reflection/absorption infrared spectroscopy, X-ray photoelectron spectroscopy, and temperature-programmed desorption study, J. Phys. Chem. B 103 (1999) 6984.

[242] H. Norenberg, G.A.D. Briggs, Surface structure of CeO_2(111) studied by low current STM and electron diffraction, Surf. Sci. 404 (1998) 734.
[243] D.R. Mullins, P.V. Radulovic, S.H. Overbury, Ordered cerium oxide thin films grown on Ru(0001) and Ni(111), Surf. Sci. 429 (1999) 186.
[244] Y. Namai, K.I. Fukui, Y. Iwasawa, Atom-resolved noncontact atomic force microscopic observations of CeO_2(111) surfaces with different oxidation states: Surface structure and behavior of surface oxygen atoms, J. Phys. Chem. B 107 (2003) 11666.
[245] Y. Namai, Y. Fukui, K. Iwasawa, Atom-resolved noncontact atomic force microscopic and scanning tunneling microscopic observations of the structure and dynamic behavior of CeO_2(111) surfaces, Catal. Today 85 (2003) 79.
[246] H. Nörenberg, G.A.D. Briggs, The surface structure of CeO_2(110) single crystals studied by STM and RHEED, Surf. Sci. 433 (1999) 127.
[247] H. Nörenberg, J.H. Harding, The surface structure of CeO_2(001) single crystals studied by elevated temperature STM, Surf. Sci. 477 (2001) 17.
[248] G.S. Herman, Surface structure determination of CeO_2(001) by angle-resolved mass spectroscopy of recoiled ions, Phys. Rev. B 59 (1999) 14899.
[249] D.D. Koellig, A.M. Boring, J.H. Wood, The electronic structure of CeO_2 and PrO_2, Solid State Commun. 47 (1983) 227.
[250] E. Wuilloud, B. Delley, W.-D. Schneider, Y. Baer, Spectroscopic evidence for localized and extended f-symmetry states in CeO_2, Phys. Rev. Lett. 53 (1984) 202.
[251] E. Wuilloud, B. Delley, W.-D. Schneider, Y. Baer, Spectroscopic study of localized and extended f-symmetry states in CeO_2, CeN and $CeSi_2$, J. Magn. Magn. Mater. 47–48 (1985) 197.
[252] A. Pfau, K.D. Schierbaum, The electronic structure of stoichiometric and reduced CeO_2 surfaces: An XPS, UPS and HREELS study, Surf. Sci. 321 (1994) 71.
[253] M.Y.T. Hanyu, H. Ishii, T. Kamada, T. Miyahara, K. Naito, H. Kato, S. Suzuki, T. Ishii, On the valence states of cerium in CeO_2, Solid State Commun. 56 (1985) 381.
[254] H. Dexpert, R.C. Karnatak, J.M. Esteva, J.P. Connerade, M. Gasgnier, P.E. Caro, L. Albert, X-ray absorption studies of CeO_2, PrO_2, and TbO_2. ii. rare-earth valence state by liii absorption edges, Phys. Rev. B 36 (1987) 1750.
[255] R.C. Karnatak, J.M. Esteva, H. Dexpert, M. Gasgnier, P.E. Caro, L. Albert, X-ray absorption studies of CeO_2, PrO_2, and TbO_2. I. Manifestation of localized and extended f states in the 3d absorption spectra, Phys. Rev. B 36 (1987) 1745.
[256] F. Marabelli, P. Wachter, Covalent insulator CeO_2: Optical reflectivity measurements, Phys. Rev. B 36 (1987) 1238.
[257] P. Wachter, Empty f-states, Kondo insulators—or what? Physica B 300 (2001) 105.
[258] A. Fujimori, Mixed-valent ground state of CeO_2, Phys. Rev. B 28 (1983) 2281.
[259] J.W. Allen, Valence fluctuations in narrow band oxides, J. Magn. Magn. Mater. 47–48 (1985) 168.
[260] M. Matsumoto, K. Soda, K. Ichikawa, S. Tanaka, Y. Taguchi, K. Jouda, O. Aita, Y. Tezuka, S. Shin, Resonant photoemission study of CeO_2, Phys. Rev. B 50 (1994) 11340.
[261] P. Burroughs, A. Hamnett, A.F. Orchard, G. Thornton, Satellite structure in the X-ray photoelectron spectra of some binary and mixed oxides of lanthanum and cerium, J. Chem. Soc., Dalton Trans. (1976) 1686.
[262] A. Fujimori, Comment on "spectroscopic evidence for localized and extended f-symmetry states in CeO_2", Phys. Rev. Lett. 53 (1984) 2518.
[263] H. Yoshida, H. Deguchi, K. Miura, M. Horiuchi, T. Inagaki, Investigation of the relationship between the ionic conductivity and the local structures of singly and doubly doped ceria compounds using EXAFS measurement, Solid State Ion. 140 (2001) 191.
[264] H. Inaba, H. Tagawa, Ceria-based solid electrolytes, Solid State Ion. 83 (1996) 1.
[265] X. Guo, S. Mi, R. Waser, Nonlinear electrical properties of grain boundaries in oxygen ion conductors: Acceptor-doped ceria, Electrochem. Solid State Lett. 8 (2005) J1.
[266] H.L. Tuller, A.S. Nowick, Small polaron electron transport in reduced CeO_2 single crystals, J. Phys. Chem. Solids 38 (1977) 859.
[267] H. Norenberg, G.A.D. Briggs, Defect structure of nonstoichiometric CeO_2(111) surfaces studied by scanning tunneling microscopy, Phys. Rev. Lett. 79 (1997) 4222.
[268] D.R. Mullins, S.H. Overbury, D.R. Huntley, Electron spectroscopy of single crystal and polycrystalline cerium oxide surfaces, Surf. Sci. 409 (1998) 307.
[269] M.A. Henderson, C.L. Perkins, M.H. Engelhard, S. Thevuthasan, C.H.F. Peden, Redox properties of water on the oxidized and reduced surfaces of CeO_2, Surf. Sci. 526 (2003) 1.
[270] M.A. Panhans, R.N. Blumenthal, A thermodynamic and electrical conductivity study of nonstoichiometric cerium dioxide, Solid State Ion. 60 (1993) 279.
[271] C. Binet, A. Badri, J.-C. Lavalley, A spectroscopic characterization of the reduction of ceria from electronic transitions of intrinsic point defects, J. Phys. Chem. 98 (1994) 6392.
[272] V. Perrichon, A. Laachir, G. Bergeret, R. Fréty, L. Tournayan, Reduction of cerias with different textures by hydrogen and their reoxidation by oxygen, J. Chem. Soc. Faraday Trans. 90 (1994) 773.
[273] M. Ricken, J. Nölting, I. Riess, Specific heat and phase diagram of nonstoichiometric ceria (CeO_{2-x}), J. Solid State Chem. 54 (1984) 89.
[274] E.A. Kümmerle, G. Heger, The structures of C–$Ce_2O_3+\delta$, Ce_7O_{12}, and $Ce_{11}O_{20}$, J. Solid State Chem. 147 (1999) 485.
[275] J. Zhang, Z.C. Kang, L. Eyring, Binary higher oxides of the rare-earths, J. Alloys Comp. 192 (1993) 57.
[276] M. Romeo, K. Bak, J.E. Fallah, F.L. Normand, L. Hilaire, XPS study of the reduction of cerium dioxide, Surf. Interface Anal. 20 (1993) 508.
[277] S.H. Overbury, D.R. Mullins, D.R. Huntley, L. Kundakovic, Chemisorption and reaction of NO and N_2O on oxidized and reduced ceria surfaces studied by soft X-Ray photoemission spectroscopy and desorption spectroscopy, J. Catal. 186 (1999) 296.
[278] U. Berner, K. Schierbaum, G. Jones, P. Wincott, S. Haq, G. Thornton, Ultrathin ordered CeO_2 overlayers on Pt(111): Interaction with NO_2, NO, H_2O and CO, Surf. Sci. 467 (2000) 201.
[279] J. Soria, A. Martinez-Arias, J. Conesa, Spectroscopic study of oxygen adsorption as a method to study surface defects on CeO_2, J. Chem. Soc. Faraday Trans. 91 (1995) 1669.
[280] F. Esch, S. Fabris, L. Zhou, T. Montini, C. Africh, P. Fornasiero, G. Comelli, R. Rosei, Electron localization determines defect formaton on ceria substrates, Science 309 (2005) 752.
[281] G. Kresse, P. Blaha, J.L.F. da Silva, M.V. Ganduglia-Pirovano, Comment on "Taming multiple valency with density functionals: A case study of defective ceria", Phys. Rev. B 72 (2005) 237101.
[282] S. Baroni, A.D. Corso, S. de Gironcoli, P. Giannozzi, http://www.pwscf.org.
[283] N. Marzari, D. Vanderbilt, Maximally localized generalized wannier functions for composite energy bands, Phys. Rev. B 56 (1997) 12847.
[284] E. Pavarini, S. Biermann, A. Poteryaev, A.I. Lichtenstein, A. Georges, O.K. Andersen, Mott transition and suppression of orbital fluctuations in orthorhombic $3d^1$ perovskites, Phys. Rev. Lett. 92 (2004) 176403.
[285] V.I. Anisimov, D.E. Kondakov, A.V. Kozhevnikov, I.A. Nekrasov, Z.V. Pchelkina, J.W. Allen, S.-K. Mo, H.-D. Kim, P. Metcalf, S. Suga, A. Sekiyama, G. Keller, I. Leonov, X. Ren, D. Vollhardt, Full orbital calculation scheme for materials with strongly correlated electrons, Phys. Rev. B 71 (2005) 125119.
[286] C. Loschen, J. Carrasco, K.M. Neyman, F. Illas, First principles LDA+U and GGA + U study of cerium oxides: Dependence on the effective U-parameter, Phys. Rev. B 75 (2007) 035115.
[287] B. Herschend, M. Baudin, K. Hermansson, A combined molecular dynamics plus quantum mechanics method for investigation of dynamic effects on local surface structures, J. Chem. Phys. 120 (2004) 4939.
[288] X. Feng, Electronic structure of MnO and CoO from the B3LYP hybrid density functional method, Phys. Rev. B 69 (2004) 155107.
[289] X. Feng, N.M. Harrison, Magnetic coupling constants from a hybrid density functional with 35% Hartree–Fock exchange, Phys. Rev. B 70 (2004) 092402.
[290] W.C. Mackrodt, D.S. Middlemiss, T.G. Owens, Hybrid density functional theory study of vanadium monoxide, Phys. Rev. B 69 (2004) 115119.

[291] C. Franchini, V. Bayer, R. Podloucky, J. Paier, G. Kresse, Density functional theory study of MnO by a hybrid functional approach, Phys. Rev. B 72 (2005) 045132.
[292] J. Uddin, J.E. Peralta, G.E. Scuseria, Density functional theory of bulk platinum monoxide, Phys. Rev. B 71 (2005) 155112.
[293] A.V. Prokofiev, A.I. Shelykh, B.T. Melekh, Periodicity in the band gap variation of Ln_2X_3 (X = O, S, Se) in the lanthanide series, J. Alloys Comp. 242 (1996) 41.
[294] L. Petit, A. Svane, Z. Szotek, W.M. Temmerman, First-principles study of rare-earth oxides, Phys. Rev. B 72 (2005) 205118.
[295] O.K. Andersen, Linear methods in band theory, Phys. Rev. B 12 (1975) 3060.
[296] H.L. Skriver, The LMTO Method, Springer Verlag, Berlin, 1984.
[297] N.V. Skorodumova, R. Ahuja, S.I. Simak, I.A. Abrikosov, B. Johansson, B.I. Lundqvist, Electronic, bonding, and optical properties of CeO_2 and Ce_2O_3 from first principles, Phys. Rev. B 64 (2001) 115108.
[298] Y.M. Chiang, E.B. Lavik, D.A. Blom, Defect thermodynamics and electrical properties of nanocrystalline oxides: Pure and doped CeO_2, Nanostruct. Mater. 9 (1997) 633.
[299] J.P. Perdew, M. Ernzerhof, in: J.F. Dobson, G. Vignale, M.P. Das (Eds.), Electronic Density Functional Theory: Recent Progress and New Directions, Plenum Press, New York, 1998.
[300] A. Filippetti, N.A. Spaldin, Self-interaction-corrected pseudopotential scheme for magnetic and strongly-correlated systems, Phys. Rev. B 67 (2003) 125109.
[301] K. Tsemekhman, E.J. Bylaska, E.C. Brown, H. Jónsson, On the orbital based estimate of the self-interaction correction to density functional theory: Less is better, unpublished.
[302] P.E. Blöchl, Projector augmented-wave method, Phys. Rev. B 50 (1994) 17953.
[303] G. Kresse, D. Joubert, From ultrasoft pseudopotentials to the projector augmented-wave method, Phys. Rev. B 59 (1999) 1758.